Die molekulare Kraftwaage

Dissertation an der Fakultät für Physik
der Ludwigs-Maximilians-Universität
München

vorgelegt von

Christian Albrecht

München, den 25. Januar 2007

1. Gutachter: Prof. Dr. Hermann E. Gaub

2. Gutachter: Prof. Dr. Joachim Rädler

Termin der mündlichen Prüfung: 21.03.2007

Zusammenfassung

Im Rahmen dieser Arbeit wurde eine neuartige Methode zur differenziellen Messung von intermolekularen Bindekräften entwickelt, die molekulare Kraftwaage. Dabei handelt es sich um einen molekularen Verbund aus zwei Rezeptor-Ligand-Komplexen, deren Bindekräfte direkt miteinander verglichen werden, wodurch selbst kleinste Unterschiede zwischen den Energielandschaften der beiden Bindungen nachgewiesen werden können.

Durch Experimente, bei denen Kraftwaagen aus kurzen DNA-Duplexen konstruiert wurden, konnte gezeigt werden, dass die differenzielle Kraftmessung auf verschiedene Stufen von Asymmetrien anspricht. So wurden Messungen durchgeführt, bei denen die Richtung, mit welcher der Duplex belastet wird, variiert wurde. Übereinstimmend mit kraftspektroskopischen Messungen wurde gefunden, dass ein sequenzielles Trennen, bei dem die Kraft parallel zur Ebene Basenpaaren angelegt wird (unzipping), unter weit geringeren Kräften vonstatten geht als ein Scheren der DNA, bei dem die Kraft senkrecht zur Ebene der Basenpaare angelegt wird.

Die außerordentlich hohe Sensitivität der differenziellen Messung konnte durch den Nachweis verschiedener Einzelbasenfehlpaarungen demonstriert werden. Dabei war es möglich, zwischen vergleichsweise stabilen Guanin-Guanin- und relativ instabilen Cytosin-Cytosin-Fehlpaarungen in einem 30-bp-Duplex zu unterscheiden.

Durch Messungen mit dem DNA-Interkalator Daunorubicin konnte die Interaktion eines Liganden mit der DNA mit sehr guter Sensitivität nachgewiesen werden, wobei gezeigt wurde, dass Daunorubicin nicht an linkshändige l-DNA bindet.

Eine in der Kraftspektroskopie bisher unbekannte mechanische Eigenschaft der DNA konnte bei geschwindigkeitsabhängigen Messungen nachgewiesen werden. Dabei handelt es sich um einen asymmetrischen Effekt, der auftritt, wenn Kraftwaagen, bei denen ein Duplex in 5'-5'- und der andere in 3'-3'-Richtung belastet wird, unter sehr hohen Kraftladungsraten getestet werden. Es konnte gezeigt werden, dass dieses Phänomen für 30 bp lange Duplexe bei einer kritischen Ladungsrate von etwa 10^5-10^6 pN/s auftritt und sehr wahrscheinlich dadurch zu erklären ist, dass die Trennung des Duplexes bei derart hohen Ladungsraten nicht mehr als eine Reaktion im Quasi-

Equilibrium angesehen werden kann, sondern im kinetischen Regime stattfindet. Dies konnte daraus geschlossen werden, dass die kritische Kraftladungsrate, bei welcher der asymmetrische Effekt beobachtet werden kann, sehr nahe an der Rate von Fluktuationen liegt, die in DNA-Duplexen nachgewiesen wurden und als „DNA-Atmung“ bezeichnet werden. Sobald die Kraft schneller angelegt wird, als Fluktuationen den Duplex öffnen können, wird die Doppelhelix offensichtlich in eine gestreckte Konformation überführt, wobei die verrichtete mechanische Arbeit als potenzielle Energie gespeichert wird, ehe es zur Trennung kommt.

Inhaltsverzeichnis

Zusammenfassung **3**

Inhaltsverzeichnis **5**

1. Einleitung **7**

2. Aufbau und Wechselwirkungen der DNA-Doppelhelix **11**

2.1 Die Struktur der Doppelhelix **11**

2.2 Wechselwirkungen in der Doppelhelix **13**

3. Thermodynamik und Kinetik **15**

4. Molekulare Wechselwirkungen unter Last **17**

5. Die Methode im Überblick **20**

6. Die Kraftwaage (Zusammenfassung der Publikationen) **22**

6.1 Der Einfluss der Bindungsgeometrie **22**

6.2 Einzelbasenfehlpaarungen **23**

6.3 Der kinetische Effekt **26**

7. „Schmelzkräfte“ (nicht publiziert) **33**

8. DNA-Interkalatoren (nicht publiziert) **35**

9. Ausblick **38**

10. Literatur **39**

11. Anhang (Publikationen) **43**

P1) **DNA: A programmable force sensor** **44**

P2) **Differential analysis of molecular rupture forces** **49**

P3) **Predicting the rupture probabilities of molecular bonds in series** **69**

P4) **Dynamic force spectroscopy with a molecular balance** **92**

P5) **dsDNA unbinds under force dependent pathways** **113**

12. Anhang (Material und Methoden) **132**

12.1 Die Herstellung des Stempels **132**

Der Stempelrohling 132

Die Beschichtung des Stempels 135

12.2 Die Herstellung des Objektträgers **137**

12.3 Das Kontaktgerät **139**

12.4 Die Fluoreszenzmessung **143**

12.5 Die Struktur der molekularen Kraftwaagen **143**

12.6 Verbrauchsmaterial **144**

12.7 Geräte **144**

12.8 Literatur (Material und Methoden) **145**

13. Anhang (Abkürzungen) **146**

1. Einleitung

Im Jahr 1827, als gerade die erste englische Dampfeisenbahnlinie ihren Betrieb aufgenommen hatte, machte der britische Botaniker Robert Brown mit seinem Mikroskop eine folgenschwere Entdeckung: Er beobachtete die wirre Bewegung kleinster Partikel in den mit Wasser gefüllten Vakuolen von Pollenkörnern[1]. Ein Ergebnis, das in einer soeben mobil gewordenen Gesellschaft vermutlich nur geringes Interesse hervorrief.

Erst achtzig Jahre später bewies Einstein, dass die Bewegung der Eisenbahn und der Brown'schen Partikel auf dieselbe Ursache zurückzuführen ist, nämlich auf thermische Energie. Im Gegensatz zur Maschine, bei der die kinetische Energie von sehr vielen Wasserteilchen zu einer gerichteten, makroskopischen Kraft umgewandelt wird, reichen laut Einstein einige wenige Kollisionen zwischen dem Partikel und Wassermolekülen aus, um die „Brown'sche Bewegung" hervorzurufen, was er aus der Relation der Partikelgröße zur thermischen Energie und der Viskosität des Wassers schließen konnte [3].

Begibt man sich von der Dampfeisenbahn über den Brown'schen Partikel in eine wiederum tausendmal kleinere Dimension, so befindet man sich auf der Größenskala biologischer Makromoleküle und somit in der Domäne der Biochemie, einer Disziplin, in der man Fluktuationen zunächst nur wenig Aufmerksamkeit schenkte. Im Gegenteil, die Vorstellung von biologischen Makromolekülen wurde vielmehr von den statischen Kristallstrukturen der Röntgenbeugungsanalyse geprägt, was sich etwa in dem Begriff „Schlüssel-Schloss-Prinzip" niedergeschlagen hat, der für die Beschreibung von Rezeptor-Ligand-Wechselwirkungen eingeführt wurde. Letztlich waren es die Einzelmolekülmethoden der Biophysik, denen es zukam, die große Bedeutung der Brown'schen Fluktuationen für biomolekulare Vorgänge experimentell nachzuweisen. Dies gelang zum Beispiel mithilfe von hochempfindlichen Fluoreszenzmikroskopen, mit denen man die thermisch verrauschten Trajektorien einzelner Moleküle direkt verfolgen konnte [4].

[1] Entgegen der weit verbreiteten Ansicht verfolgte Brown nicht die Bewegung ganzer Pollenkörner, welche zu groß sind, um durch thermische Fluktuationen bewegt zu werden, sondern kleine Partikel in Pollenkörnern [1], [2].

Eine besondere Stellung unter den Einzelmolekültechniken kam dabei den kraftspektroskopischen Methoden zu, da sie erstmals eine mechanische Charakterisierung von molekularen Systemen erlaubten. Dabei konnte festgestellt werden, dass der Arbeitszyklus von molekularen Motoren mit dem thermischen Rauschen der Umgebung synchronisiert ist. Auf diese Weise kann ein Transportprozess durch ungerichtete Fluktuationen vorangetrieben werden, wobei sich der Motor darauf beschränkt, die Rückreaktion unter Verbrauch von chemischer Energie zu unterbinden. Zwar kann auf diese Weise keine Wärme in Arbeit umgewandelt werden, wie es bei der Dampfmaschine der Fall ist, jedoch spart der molekulare Motor Energie, die er bei einem zu schnellen Takt durch Reibung mit der Umgebung verlieren würde [5], [6]. Ein weiterer Meilenstein der Kraftspektroskopie war der Nachweis einzelner Rezeptor-Ligand-Interaktionen. Da man die Kraft zur Trennung einer solchen Wechselwirkung maximal über eine Strecke von der Größe der Bindungstasche aufbringen muss, konnte man anhand der Einstein'schen Relation $k_BT \approx 4$ pN·nm abschätzen, dass Bindungen von einigen k_BT in Kräfte im Piconewtonbereich umgesetzt würden, was sich auch prompt experimentell bestätigen ließ [2]. Außerdem konnte man aus der Streuung der gemessenen Trennkräfte wiederum den stochastischen Charakter des thermisch aktivierten Trennprozesses ablesen [7].

Entsprechend der Vielfalt biologischer Interaktionen wurde eine Reihe verschiedener Verfahren zur Kraftmessung an einzelnen Molekülen entwickelt. Dabei erfolgt das Anlegen und Auslesen von Kräften entweder über die Verbiegung einer sehr kleinen Feder, die aus Halbleitermaterial (atomic force microscope), einer feinen Glasfaser (glass micro needle), aber auch aus einer biologischen Membran (biomolecular force probe) bestehen kann oder über mikroskopisch kleine Kugeln, die in einem Kraftfeld gefangen werden (optical tweezers, magnetic tweezers) [8], [9]. Insgesamt betrachtet haben diese kraftspektroskopischen Methoden eine enorme Kraft- und Ortsauflösung, jedoch auch Limitationen, deren Ursprung im Wesentlichen auf die Größenasymmetrie zwischen der Kraftsonde (Transducer) und der zu vermessenden Probe zurückzuführen ist. So weist etwa ein Partikel von zehn Mikrometern Durchmesser eine tausendmal größere Reibung auf als ein Protein von einem Nanometer Durchmesser und unterliegt deshalb etwa dreißigmal größeren Kraftfluktuationen, welche die Messung als Hintergrundrauschen beeinträchtigen [10]. Eine weitere Fehlerquelle beruht auf

[2] k_BT = Boltzmannkonstante · absolute Temperatur

hydrodynamischen Effekten, die besonders dann auftreten, wenn die Kraftsonde mit hoher Geschwindigkeit durch das auf der mikroskopischen Skala hochviskose Wasser gezogen wird. Ein Effekt, der bei einem symmetrischen Größenverhältnis von Kraftsonde und Probe gleich groß ausfallen würde und somit ohne störenden Einfluss wäre. Die Forderung nach größtmöglicher Messgenauigkeit ist demzufolge eine Forderung nach der größtmöglichen Symmetrie des Messaufbaus, was im radikalsten Sinn nur dann erfüllbar ist, wenn die Kraftsonde das genaue Spiegelbild der Probe darstellt. Ein Prinzip, das in der vorliegenden Arbeit in Form einer molekularen Kraftwaage verwirklicht wurde.

Bei einer molekularen Kraftwaage handelt es sich um ein differenzielles Messverfahren, bei dem die Trennkräfte von Rezeptor-Ligand-Komplexen direkt miteinander verglichen werden. Dies geschieht, indem an die Enden einer Kette aus zwei Komplexen eine Kraft angelegt wird, bis es zur Trennung einer der beiden Interaktionen kommt. Entsprechend dem Prinzip des schwächsten Glieds in einer Kette kann auf diese Weise eine Aussage über die relative Stabilität der beiden Rezeptor-Ligand-Komplexe getroffen werden. In Abb. 1 ist dies für eine Kraftwaage aus DNA-Duplexen dargestellt, die aus einem Referenz-Duplex (blau) und einem Proben-Duplex (rot) aufgebaut ist, welche zwischen zwei Oberflächen angebunden werden. Durch Trennen der Oberflächen, kommt es zum Aufbau einer Kraft in der Kraftwaage, bis einer der beiden Duplexe zerreißt. Je nachdem, welche der beiden Bindungen die stabilere ist, wird die Markierung (grün), die am mittleren Teil der Waage befestigt ist, nach der Trennung entweder auf der unteren oder oberen Oberfläche zu finden sein. Führt man einen solchen differenziellen Test mit einer perfekt symmetrischen Waage durch, so ist die relative Stabilität beider Duplexe gleich groß. Wird nun an einem der beiden Duplexe eine Veränderung eingeführt, so kann dessen Trennkraft dadurch stark verschoben werden, was sich aus einer anderen Verteilung der Markierung zwischen den Oberflächen ablesen lässt.

Das klassische Beispiel einer differenziellen Kraftmessung ist die Bestimmung eines Probengewichts mit einer Balkenwaage. Dabei wird das Ergebnis in Einheiten der Masse statt der Kraft angegeben, was insofern akzeptabel ist, da die Gewichtskraft der Probe im Wesentlichen von einem einzigen variablen Parameter, nämlich der Probenmasse abhängt.

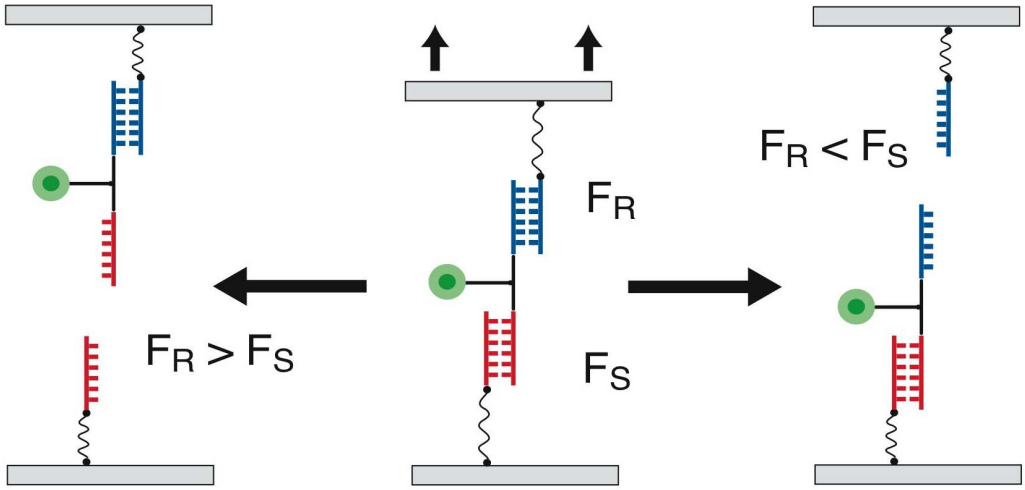

Abbildung 1: Das Prinzip der molekularen Kraftwaage. Durch Anlegen einer externen Kraft an zwei Oligonukleotidduplexe (rot, blau) kommt es zu einem Bindungsbruch. Nach dem Trennen befindet sich die Fluoreszenzmarkierung (grün) oben, wenn die Trennkraft des unteren Duplexes F_S kleiner ist als die des oberen Duplexes F_R. Für den Fall $F_S > F_R$ findet sich die Markierung auf der unteren Oberfläche.

Eine Balkenwaage ist deshalb resistent gegen Veränderungen der Beschleunigung und würde z. B. auch auf dem Mond funktionieren. Außerdem kann sie sehr einfach durch die Verwendung verschiedener geeichter Gewichte bedient werden, ohne dass man dabei im Allgemeinen Rücksicht auf die Zusammensetzung der Probe, ihre Konsistenz, Größe etc. nehmen müsste. Im Gegensatz dazu steht man bei der Kalibrierung einer molekularen Kraftwaage vor einer ungleich größeren Herausforderung, da es sich bei der Trennkraft im Gegensatz zur Gewichtskraft keineswegs um eine einparametrige Messgröße handelt, sondern vielmehr um eine komplexe Funktion, die auf einer Vielzahl von energetischen und mechanischen Probenvariablen beruht, welche zum Teil gegensätzlichen Einfluss auf die Nettokraft haben können.

Die vorliegende Arbeit befasst sich zum ersten Mal systematisch mit den Eigenschaften von molekularen Kraftwaagen am Beispiel von DNA-Oligonukleotid-Duplexen. Zu diesem Zweck wurde es angestrebt, eine Waage von möglichst perfekter Symmetrie zu konstruieren, mit deren Hilfe man die Auswirkung verschiedenster Modifikationen am Probenduplex auf die Trennkraft studieren kann. Untersucht wurden dabei die Auswirkungen struktureller und energetischer Asymmetrien bis hin zur Sondierung der Energielandschaft von DNA durch dynamische differenzielle Messungen.

2. Aufbau und Wechselwirkungen der DNA-Doppelhelix

2.1 Die Struktur der Doppelhelix

Die ungewöhnliche Eigenschaft der DNA, als Vorlage der eigenen Replikation zu dienen, basiert strukturell auf der Paarung von zwei Einzelsträngen, welche die gleiche Information, jedoch in komplementärer Schreibweise aufweisen. Aus der schieren Masse der Information, die auf diese Weise gespeichert wird, ergibt sich eine schnell ins Auge fallende Asymmetrie, nämlich das extreme Aspektverhältnis hinsichtlich Länge und Durchmesser, das in menschlichen Chromosomen bis zu $1:10^8$ betragen kann. Bei den in dieser Arbeit verwendeten kurzen Oligonukleotidduplexen beträgt das Aspektverhältnis zwar nur 1:5, was im Vergleich zu einem Chromosom wenig erscheint, aber mit wichtigen Konsequenzen für die kraftinduzierte Trennung der Doppelhelix verbunden ist.

Um nachvollziehen zu können, warum die beiden Einzelstränge der DNA nur in antiparalleler Paarung und fast ausschließlich als rechtsgängige Helizes vorliegen, ist es hilfreich, sich die genaue chemische Struktur der Desoxy-Ribose zu vergegenwärtigen, welche das verbindende Element zwischen dem Rückgrat und den funktionellen Gruppen der DNA darstellt. Dabei erkennt man leicht, dass die Einzelstränge eine Polarität aufweisen, die dadurch bedingt ist, dass sich zwischen dem C^3- und dem C^5-Atom des Zuckers keine Symmetrieachse konstruieren lässt, wodurch die Sauerstoffatome des Furanoseringes bei einer antiparallelen Paarung in entgegengesetzte Richtungen weisen (Abb. 2). Bei einer parallelen Paarung würden diese Sauerstoffatome in die gleiche Richtung zeigen, was aufgrund der damit verbundenen ungünstigen Bindungswinkel und der suboptimalen Ausrichtung von Basenstapelinteraktionen und Wasserstoffbrückenbindungen jedoch praktisch ausgeschlossen ist.

Helikale Strukturen von Biopolymeren sind grundsätzlich an chirale Bausteine gebunden, die alle in der gleichen chiralen Konfiguration (also entweder L oder D) vorliegen müssen. Im Fall der DNA handelt es sich um das asymmetrische C^4-Atom der Ribose, das bei natürlichen Nukleinsäuren stets in D-Konfiguration vorliegt und eine starke Bevorzugung der rechtshändigen Helix bedingt.

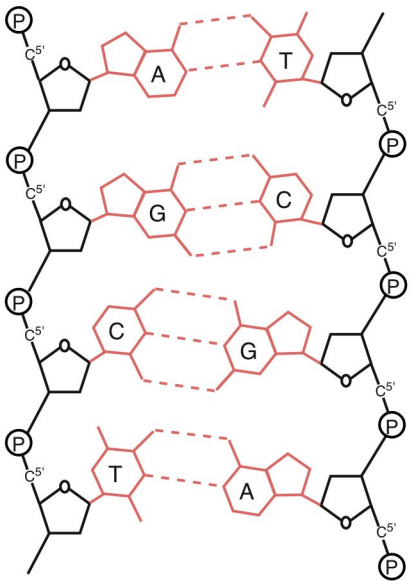

Abbildung 2: DNA in 2D-Projektion: Basen und Wasserstoffbrücken in rot. Bedingt durch die Asymmetrie der Ribose erfolgt die Paarung der DNA-Stränge stets antiparallel.

Bei der Herstellung künstlicher Oligonukleotide können allerdings ebenso L-Ribose-Bausteine verwendet werden, die zu linkshändigen Helizes führen. Der Durchmesser und die Steigung der Helix pro Basenpaar werden durch die Konformation der Ribose vorgegeben, die sowohl in einer $C^{2'}$-endo- oder $C^{3'}$-endo-Konformation vorliegen kann (Abb. 3).

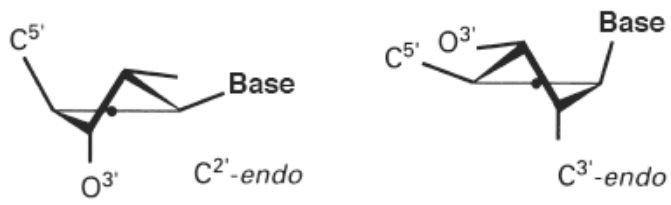

Abbildung 3: Die beiden Konformationen von D-Ribose in DNA

Liegen alle Furanoseringe in $C^{2'}$-endo-Konformation vor, so bildet sich eine B-Helix aus, bei einer $C^{3'}$-endo-Konformation dagegen eine A-Helix, die allerdings auf nicht-physiologische Bedingungen wie Wasserarmut beschränkt ist. Bei der vorliegenden Arbeit ist deshalb von B-DNA auszugehen. Die Eigenschaften von A-DNA und B-DNA sind in Tabelle 1 zusammengefasst.

	A-DNA	B-DNA
Basenpaare/Helixwindung	11	10
Winkel zwischen zwei Basen	32,7°	36°
Abstand der Basenpaare	2,9 Å	3,1 - 3,3 Å
Winkel zw. Helixachse u. Bp.	70°	90°
Konformation der Ribose	$C^{3'}$-endo	$C^{2'}$-endo

Tabelle 1: Strukturdaten von A-DNA und B-DNA nach [11].

2.2 Wechselwirkungen in der Doppelhelix

DNA besitzt die interessante Eigenschaft, durch Erhitzen und Abkühlen beliebig oft „geschmolzen“ und renaturiert werden zu können, ohne dass der genetische Code dabei Schaden nehmen würde. Ein Verhalten, aus dem man schließen kann, dass die Struktur der DNA auf zwei verschiedenen Arten von Wechselwirkungen beruht, die sich in ihrer thermischen Stabilität stark voneinander unterscheiden, nämlich auf kovalenten Bindungen und nicht-kovalenten Wechselwirkungen. Tatsächlich liegt die Stabilität einer einzelnen nicht-kovalenten Wechselwirkung sogar bedeutend unter der 100°C-Grenze, was in Abb. 4 veranschaulicht wird: Hierbei handelt es sich um die Gegenüberstellung der Bindungspotenziale einer kovalenten Bindung und einer Wasserstoffbrücke. Aus der Relation der Bindungsenergie zur thermischen Energie k_BT wird deutlich, dass einzelne Wasserstoffbrücken, im Gegensatz zu kovalenten Bindungen, bei Raumtemperatur sofort dissoziieren, was auch für die anderen nicht-kovalenten Wechselwirkungen gilt, die der Struktur der DNA zugrunde liegen.

Wie auch bei anderen Rezeptor-Ligand-Systemen findet man in der DNA-Doppelhelix eine fein ausbalancierte Nettowechselwirkung, die sich aus einer Vielzahl attraktiver und repulsiver Kräfte zusammensetzt. Hinsichtlich der attraktiven Kräfte sind zunächst die Basenstapelinteraktionen zu nennen, welche besonders starke π-π-van-der-Waals-Wechselwirkungen zwischen den planaren Ringsystemen benachbarter Basen eines Stranges ausbilden. Obwohl diese Interaktionen demnach gar keine direkte Verbindung zu dem anderen Strang herstellen, sind sie von erheblicher Bedeutung, da sie entgegen der Entropie die „Bindungstasche” der beiden Einzelstränge „in Ordnung“ halten.

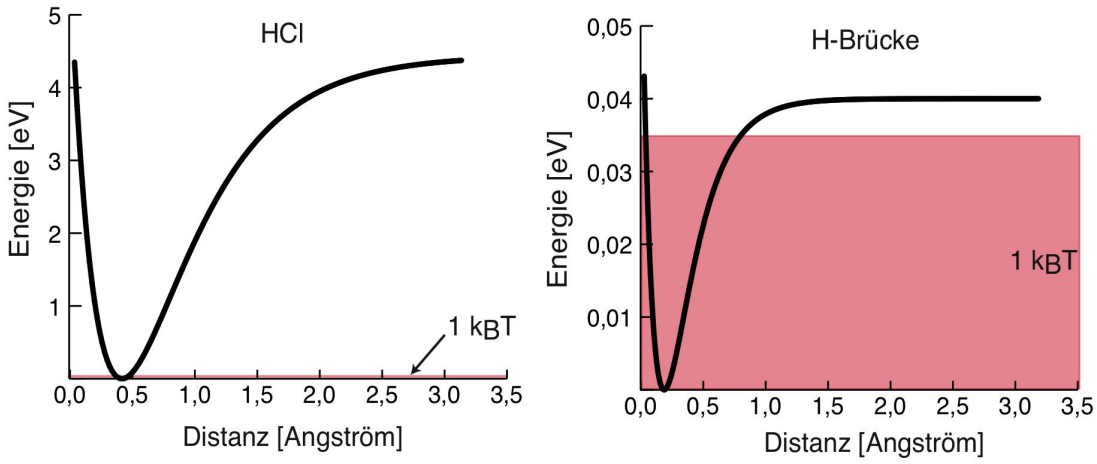

Abbildung 4: Morsepotenzial einer kovalenten und einer nicht-kovalenten Bindung. Das Potenzial der HCl-Bindung weist im Vergleich zur Wasserstoffbrücke eine etwa hundertmal höhere potenzielle Energie auf. Aus dem Verhältnis der Potenzialtiefen zur thermischen Energie k_BT resultiert die große Stabilität von kovalenten Bindungen und die Instabilität einzelner nicht-kovalenter Bindungen bei Raumtemperatur. Die Berechnung des HCl-Potenzials erfolgte nach [12], die des H-Brückenpotenzials nach [13].

Tatsächlich liegt auch einzelsträngige DNA bei Raumtemperatur überwiegend in helikaler Form vor [14]. Die eigentliche Interaktion zwischen den Strängen geht auf Wasserstoffbrücken zurück, von denen sich drei zwischen Guanin und Cytosin bzw. zwei zwischen Adenin und Thymin ausbilden (siehe Abb. 2). GC-Basenpaare bewirken deshalb eine höhere Stabilisierung der Doppelhelix als AT-Basenpaare. Als dritter stabilisierender Beitrag ist der hydrophobe Effekt zu nennen. Hierbei handelt es sich um H_2O-Moleküle, welche die hydrophoben Basen der dissoziierten Einzelstränge in einer entropisch ungünstigen Kristallstruktur umschließen und die freigesetzt werden, sobald die Stränge aneinander binden.

Bei den repulsiven Wechselwirkungen sind vor allem die stark negativ geladenen Phosphate des Rückgrats zu nennen, welche sich sowohl intra- als auch intermolekular abstoßen. Unter physiologischer NaCl-Konzentration von ~150 mM wird dieser repulsive Beitrag jedoch so stark abgeschirmt, dass keine repulsive Wechselwirkung zwischen den Strängen mehr auftritt. Der hauptsächliche repulsive Beitrag ist entropischer Natur und beruht auf der viel größeren Anzahl von Freiheitsgraden des ungebundenen Einzelstrangs [15], [16].

3. Thermodynamik und Kinetik

Ein einfacher thermodynamischer Ansatz zur Beschreibung von Rezeptor-Ligand-Interaktionen ist das Zwei-Zustands-Modell, das auf der Annahme beruht, dass die Bindungspartner *R* und *L* entweder als Komplex *RL* oder getrennt vorliegen, ohne dass dabei Zwischenzustände zu berücksichtigen sind.

. i $R + L \Leftrightarrow RL$

Im Potenzialmodel, wie es in Abb. 5 gezeigt wird, entsprechen die gebundenen Zustände einem Ort in einem Potenzialtopf, dessen Tiefe als Barriere ΔG_{off} bezeichnet wird, die sich aus der freien Gibbs'schen Energie der Bindung ΔG und der Aktivierungsbarriere der Assoziation ΔG_{on} zusammensetzt.

. ii $\Delta G = \Delta G_{off} - \Delta G_{on}$

In Abb. 5 ist der Komplex als Kugel dargestellt, die sich im Minimum des Potenzialtopfs befindet und aus dem er durch thermische Fluktuationen auf höhere Energieniveaus verlagert werden kann.

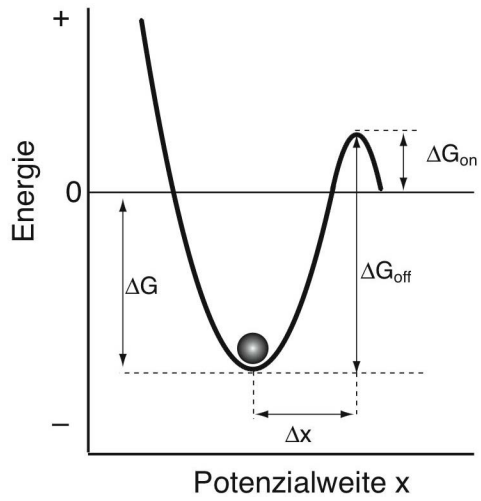

Abbildung 5: Das Bindungspotenzial einer Rezeptor-Ligand-Interaktion mit der Energiebarriere ΔG_{off}, die sich aus der freien Gibbs'schen Energie der Bindung ΔG und der Aktivierungsenergie ΔG_{on} zusammensetzt. Die Kugel symbolisiert den Komplex, der sich in dieser Darstellung im Minimum des Potenzials befindet. Bei thermischer Anregung wird der Komplex auf ein höheres Niveau verlagert.

Der Anteil gebundener Zustände im thermodynamischen Gleichgewicht skaliert exponentiell mit der freien Gibbs'schen Energie ΔG, woraus sich die Gleichgewichtskonstante der Dissoziation K_D ergibt

. iii $$K_D = \frac{[R]\cdot[L]}{[RL]} = e^{\frac{-\Delta G}{k_B T}},$$

wobei k_B die Boltzmannkonstante und T die absolute Temperatur bezeichnet. Die Frage, wie schnell sich das Gleichgewicht einstellt, hängt dabei zum einen von der Höhe der beiden Barrieren ΔG_{off} und ΔG_{on} und zum anderen davon ab, mit welcher Probierrate ν das System versucht, die Barrieren zu überwinden. Daraus ergeben sich die Raten der Assoziation k_{on} und der Dissoziation k_{off} als Funktionen der Probierfrequenzen ν_{on} und ν_{off}.

. iv $$k_{on} = \nu_{on} \cdot e^{\frac{-\Delta G_{on}}{k_B T}}$$

. v $$k_{off} = \nu_{off} \cdot e^{\frac{-\Delta G_{off}}{k_B T}}$$

Da man im Allgemeinen davon ausgeht, dass ν_{on} und ν_{off} für ein bestimmtes System identisch sind, kann man aus der Gleichgewichtskonstante und einer der beiden Raten die andere Rate berechnen.

.vi $$K_D = \frac{k_{off}}{k_{on}}$$

Im Fall von kurzen DNA-Duplexen ist es möglich, entsprechend Gleichung .vii die thermodynamischen Eigenschaften der Bindung, also die enthalpischen und entropischen Beiträge ΔH und ΔS in Abhängigkeit der Temperatur T, sowie die Schmelztemperatur T_m theoretisch vorherzusagen.

. vii $$\Delta G = \Delta H - \Delta S \cdot T = \Delta S(T_m - T)$$

Die besten Ergebnisse werden dabei mit dem „nearest neighbour"-Algorithmus erzielt, dessen Abweichung zu empirischen Ergebnissen mit ± 3 % angegeben wird [17], [18]. Die in dieser Arbeit verwendeten ΔG-Werte wurden mit dem Computerprogramm Hyther™ berechnet [19].

4. Molekulare Wechselwirkungen unter Last

Bei der kraftinduzierten Trennung eines Rezeptor-Ligand-Komplexes handelt es sich im Allgemeinen um einen Vorgang, bei dem die Bindungsenergie durch ein Zusammenspiel von mechanischer Arbeit und thermischen Fluktuationen überwunden wird, wobei sich jedoch kein Gleichgewicht einstellen kann, da die Reaktanten manipulativ voneinander getrennt werden und eine Rückreaktion somit ausgeschlossen wird. Der Haupteffekt der mechanischen Arbeit besteht darin, dass ein Teil der Barriere ΔG_{off} durch das Anlegen der Kraft überwunden wird, wodurch die Dissoziationsrate stark ansteigt. Die kraftabhängige Dissoziationsrate $\lambda(F)$ wird durch Gleichung .viii beschrieben, wobei ν_{off} für die Probierrate der Dissoziation steht.

. viii $$\lambda(F) = \nu_{off} \cdot e^{-\frac{\Delta G_{off} - F \cdot \Delta x}{k_B T}}$$

In Abb. 6 ist die Trennung eines Komplexes unter Last als Bindungspotenzial dargestellt, bei dem der Komplex (Kugel) durch thermische Anregung bereits auf ein höheres Energieniveau gehoben wurde und der restliche Teil durch mechanische Arbeit überwunden wird, indem eine Kraft F, die der Steigung des grauen Pfeils entspricht, über die Strecke Δx angelegt wird.

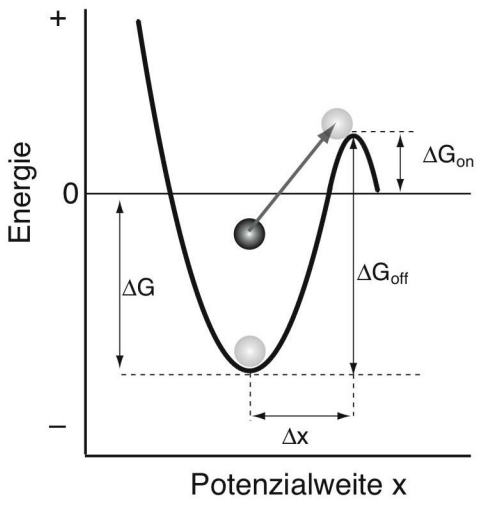

Abbildung 6: Beispiel für die Dissoziation eines Komplexes unter Krafteinwirkung. Bei dem dargestellten Fall wird ein Teil der Energiebarriere ΔG_{off} allein durch thermische Anregung überwunden, der restliche Teil durch mechanische Arbeit, wobei die Steigung des grauen Pfeils der angelegten Kraft F entspricht.

Der Zusammenhang zwischen der freien Gibbs'schen Energie der Dissoziation ΔG_{off} der wahrscheinlichsten Trennkraft F, in Abhängigkeit von der Bindungsweite Δx und

der Kraftladungsrate r, sowie der Dissoziationsrate bei Null-Kraft k_{off} wird durch das Bell-Evans-Modell [20], [21] beschrieben.

$$F = \frac{k_B T}{\Delta x} \cdot \ln \frac{r \cdot \Delta x}{k_B T \cdot k_{off}} \quad \textbf{. ix}$$

Durch Einsetzen von Gleichung .v in Gleichung .ix und Umformen erhält man den Zusammenhang zwischen der geleisteten mechanischen Arbeit und der Höhe der Energiebarriere ΔG_{off}

$$F \cdot \Delta x = \Delta G_{off} + \ln \frac{r \cdot \Delta x}{\nu_{off} \cdot k_B T}, \quad \textbf{.x}$$

wobei die Probierfrequenz ν_{off} nach der ursprünglichen Theorie von Bell mit 10^{13} /s angenommen wird, was der Oszillationsrate von Atomen in einem Festkörper entspricht [20]. Nach der Kramers-Theorie, welche die viskose Dämpfung in Flüssigkeit mit in Betracht zieht, wird ν_{off} mit maximal 10^{10} /s angegeben [22].

Gemäß Gleichung .ix besteht eine logarithmische Abhängigkeit zwischen der an einen Rezeptor-Ligand-Komplex angelegten Ladungsrate r und dessen wahrscheinlichster Trennkraft F, weshalb man davon ausgeht, dass es für ein bestimmtes System keine charakteristische Trennkraft gibt. Am ausführlichsten wurde die Kraft-Ladungsraten-Korrelation an kurzen DNA-Duplexen zwischen zehn und dreißig Basenpaaren untersucht [23]. Anhand dieser Messungen konnte eine Formel für die Bindungsweite Δx von Oligoduplexen in Abhängigkeit der Basenpaaranzahl n formuliert werden.

$$\Delta x = (7 \pm 3)\text{Å} + (0.7 \pm 0.3) n\text{Å} \quad \textbf{. xi}$$

Bei denselben Messungen stellte es sich auch heraus, dass bei hohen Ladungsraten und langen Duplexen ein Kraftlimit von 65 pN erreicht wird, ein Phänomen, das bereits vorher für polymere DNA von einigen Kilobasen Länge beschrieben wurde. Eine typische Kraftkurve von langer doppelsträngiger DNA beginnt mit einem Anstieg der Kraft bis auf 65 pN, bei der die Helix ihre B-DNA-Konformation behält. Daraufhin kommt es bei konstanter Kraft zur Ausdehnung der Probe um den Faktor 1,7 und zum Abschmelzen des freien Stranges (Abb. 7) [24], [25]. Das Kraftplateau bei 65 pN wurde mit dem Namen „B-S-Übergang" versehen, da man es als ein „Überstrecken" der Helix

interpretiert, bei der die B-Konformation in eine S-Konformation, d. h. in eine deformierte Helix mit intakten Basenpaaren überführt wird (Abb. 8) [24], [26].

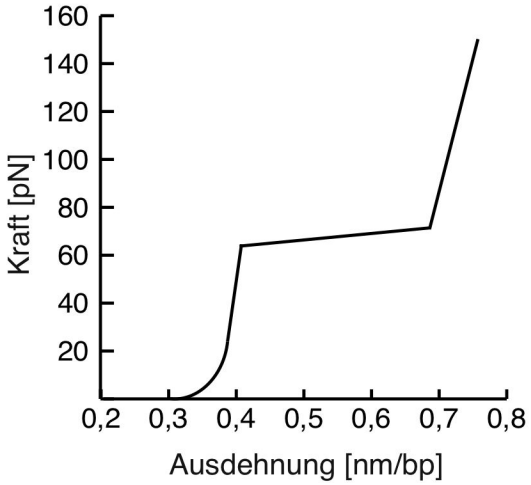

Abbildung 7: Überstrecken von polymerer DNA. Bei ~65 pN wird ein Kraftplateau erreicht, bei dem es zur 1,7-fachen Ausdehnung der DNA kommt (nach [27]).

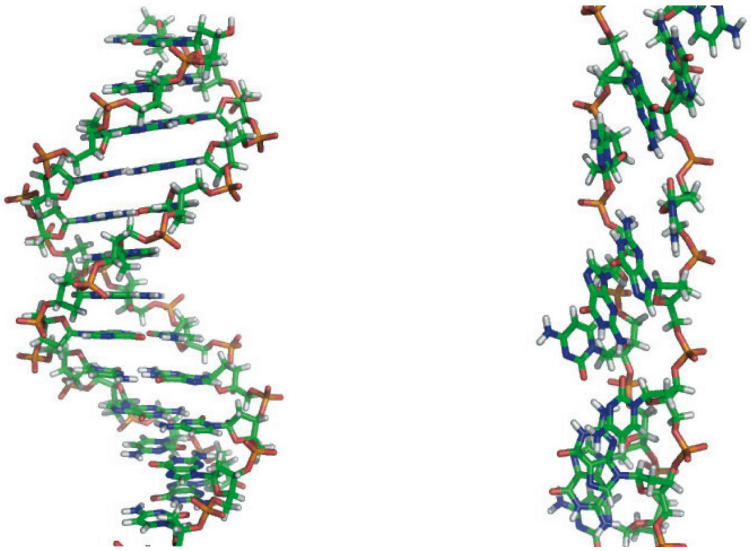

Abbildung 8: DNA in B-Konformation (links) und in 1,3-fach überstreckter S-Konformation (nach [26]).

Eine dieser Auffassung widersprechende Theorie interpretiert die Längenausdehnung bei konstanter Kraft dagegen als ein lokales Schmelzen, bei dem intakte Helixabschnitte und Blasen mit geöffneten Basenpaaren koexistieren, bis es unter dem Einfluss der mechanischen Arbeit zum Ausweiten der Blasen und schließlich zur Trennung der gesamten Doppelhelix kommt [28], [16], [27].

5. Die Methode im Überblick

In Abb. 9 ist der Ablauf eines Kraftwaagen-Experiments dargestellt. Dazu werden auf einem Objektträger bis zu sechzehn Messflecken mit verschiedenen Kraftwaagen angebunden. Daraufhin wird ein Silikonstempel, der sechzehn hervorstehende Noppen aufweist, die mit Streptavidin beschichtet sind, mit dem Objektträger in Kontakt gebracht. Dabei kommt die erhabene quadratische Mikrostruktur, die sich auf den Stirnflächen der Stempelnoppen befindet, in Kontakt mit den Kraftwaagen, deren Biotingruppen dabei an das Streptavidin des Stempels koppeln. Durch Anlegen einer Zugkraft an den Stempel kommt es zum Zerreißen der gekoppelten Kraftwaagen, weshalb nach dem Trennen auf dem Objektträger ein Abdruck der Stempelstruktur zu erkennen ist.

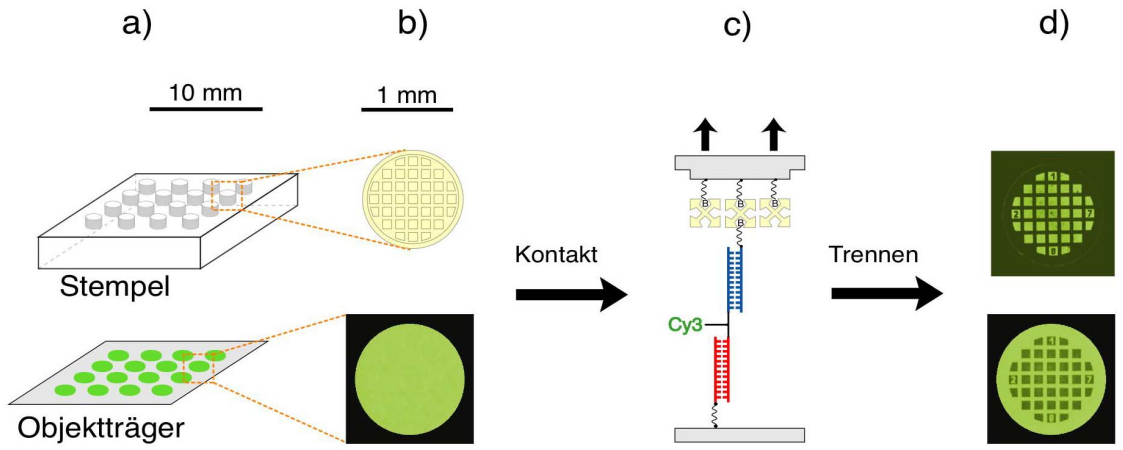

Abbildung 9: Ablauf eines Kraftwaagenexperiments: a) Schema des Objektträgers mit sechzehn Messflecken (grün) und des Stempels mit sechzehn Noppen, die mit Streptavidin beschichtet sind. b) Vergrößerte Aufsicht auf eine Noppe mit Streptavidinbeschichtung (gelb). Fluoreszenzbild eines Messflecks mit Kraftwaagen (grün). c) Schema einer Kraftwaage, die über Streptavidin (gelb) an den Stempel gekoppelt wurde. d) Fluoreszenzbilder einer Noppe und eines Messflecks nach der Trennung von Stempel und Objektträger. Von den quadratischen Kontaktflächen wurde ein Teil der Fluoreszenzmarkierung auf den Stempel übertragen.

Bei der Auswertung des Experiments wird das Fluoreszenzmuster der Messflecken analysiert, wie in Abb. 10 gezeigt, wobei das Ergebnis als Überlebenswahrscheinlichkeit des Probenkomplexes Φ_S angegeben wird. Φ_S berechnet sich aus dem Anteil der auf dem Objektträger verbliebenen Fluoreszenzmarkierungen normalisiert auf die Menge der Kraftwaagen, die getestet wurden. Dazu wird die auf den quadratischen Kontaktflächen verbliebene Fluoreszenzintensität $Cy3_{REM}$ ermittelt. Um das Ergebnis zu normalisieren, wird die Fluoreszenzintensität $Cy3_{START}$ ermittelt, also das Signal auf der

gitterförmigen Fläche, die nicht mit dem Stempel in Kontakt gekommen ist. Das Endergebnis, die Überlebenswahrscheinlichkeit des Proben-Duplex Φ_S, errechnet sich schließlich als $\Phi_S = Cy3_{REM} / Cy3_{START}$.

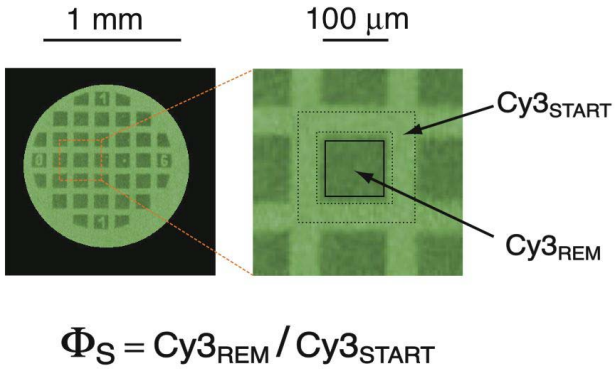

Abbildung 10: Die Auswertung eines Kraftwaagenexperiments: Fluoreszenzbild eines Messflecks nach der Trennung von dem Stempel (vgl. Abbildung 9d). Das Signal der verbliebenen Markierungen $Cy3_{REM}$ wird auf den quadratischen Kontaktflächen ermittelt. Das zur Normalisierung dienende Signal $Cy3_{START}$, das der Dichte der Kraftwaagen entspricht, wird auf der Gitterstruktur ermittelt. Durch Quotientenbildung erhält man das Endergebnis, die Überlebenswahrscheinlichkeit des Proben-Duplexes Φ_S.

Da man nicht davon ausgehen kann, dass 100 % aller Waagen an den Stempel binden, muss das Ergebnis außerdem hinsichtlich der Kopplungseffizienz korrigiert werden, wie in P2, P3 und P4 ausführlich beschrieben. Der detaillierte Ablauf eines Kraftwaagen-experiments wurde in Publikation P2 beschrieben. Die Erweiterung der Methode zu dynamischen Messungen ist in P4 beschrieben. Dabei ist zu beachten, dass die Terminologie zum Teil verändert wurde und die Kraftwaage im einen Fall als DRC (differential rupture complex), im anderen Fall als „force balance" bezeichnet wird. Für den Ausdruck der Überlebenswahrscheinlichkeit Φ_S wird in P2 noch der Begriff *RRP* (relative rupture probability) verwendet.

6. Die Kraftwaage (Zusammenfassung der Publikationen)

Um die Auswirkungen einer Modifikation an einem Komplex auf dessen Trennkraft studieren zu können, ist es notwendig, zuerst eine molekulare Kraftwaage von möglichst perfekter Symmetrie zu konstruieren. Dies lässt sich wiederum über die Analogie zur Balkenwaage verstehen, deren Messgenauigkeit unter anderem auch davon abhängt, ob sich der Balken im Leerzustand in einer horizontalen Position befindet. Eine perfekt symmetrische DNA-Kraftwaage scheint auf den ersten Blick einfach realisierbar zu sein, wenn man zwei Duplexe identischer Länge verwendet, die in der gleichen Geometrie an die Oberflächen gebunden werden. Dies ist in Abb. 11 an den Beispielen einer DNA-Waage mit doppeltem Scher-Modus (links) und einer anderen mit doppeltem Zipper-Modus (rechts) dargestellt.

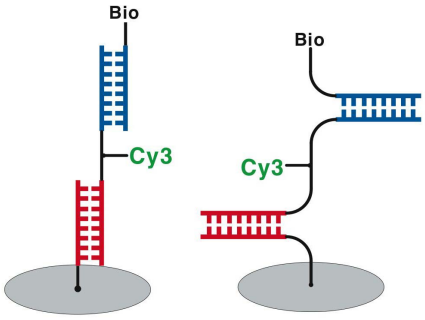

Abbildung 11: Kraftwaagen mit einheitlichen Bindungsgeometrien. Doppelter Scher-Modus (links) und doppelter Zipper-Modus (rechts).

6.1 Der Einfluss der Bindungsgeometrie

Der ausschlaggebende Einfluss der Bindungsgeometrie auf die Trennkraft von DNA konnte durch kraftspektroskopische Messungen nachgewiesen werden: Durch Anlegen einer Zugkraft an die 5'- und 3'-Termini eines Duplexendes wird die DNA parallel zur Ebene der Basenpaare belastet und es kommt zu einem sogenannten „Unzipping", bei dem die Wasserstoffbrücken sequenziell mit einer Kraft von 10-15 pN getrennt werden. Belastet man die Helix dagegen senkrecht zur Ebene der Wasserstoffbrücken, indem man die Kraft an die beiden 5'-Enden der gegenüberliegenden Duplexenden anlegt, so können die gemessenen Trennkräfte um ein Vielfaches höher ausfallen, was man darauf zurückführt, dass alle Wasserstoffbrücken gleichzeitig belastet, also „geschert" werden [29], [23], [30].

Auch bei den differenziellen Experimenten der vorliegenden Arbeit, die entsprechend dem Schema in Abb. 12 durchgeführt wurden, erwies sich der Schermodus bei gleicher Duplexlänge stets als um ein Vielfaches stabiler als der Zippermodus (P1 und P2).

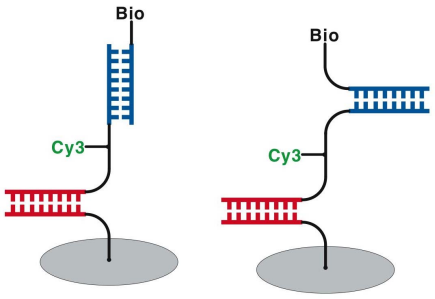

Abbildung 12: Kraftwaagen zum Vergleich von Zipper- und Schergeometrie.

6.2 Einzelbasenfehlpaarungen

Nachdem es bei dem vorigen Experiment gelungen war, zwei verschiedene Entbindungspfade energetisch equivalenter Bindungen zu unterscheiden, sollte nun die eingangs postulierte, besonders gute Kraftauflösung der differenziellen Methode erprobt werden. Dies sollte mit dem Nachweis von einzelnen fehlgepaarten Basen (Mismatches) in DNA-Duplexen erfolgen, welche mit kraftspektroskopischen Methoden nur schwer aufgelöst werden können, da der geringe Kraftunterschied weitgehend von thermisch bedingten Fluktuationen der Kraftsonde überlagert wird. Von besonderem Interesse sind Mismatches auch deshalb, da eine minimale strukturelle Änderung, eben der Austausch eines einzelnen Nukleotids, eine beträchtliche Verminderung der thermodynamischen Stabilität des DNA-Duplexes mit sich bringt, was man sich in der molekularen Diagnostik beim Nachweis von Einzelbasen-mutationen (single nucleotide polymorphisms) zunutze macht [31]. Die Detektion eines Mismatches, der in den Probenduplex eingefügt wurde, ist schematisch in Abb. 13 dargestellt.

Tatsächlich gelang es mit der differenziellen Methode nicht nur, Einzelbasenfehl-paarungen von vollständig gepaarten Duplexen (Perfect-Matches) zu diskriminieren, sondern auch verschiedene Mutationen voneinander zu unterscheiden, wie z. B. GG- und CC-Fehlpaarungen in 30-bp-Duplexen (P2, P3).

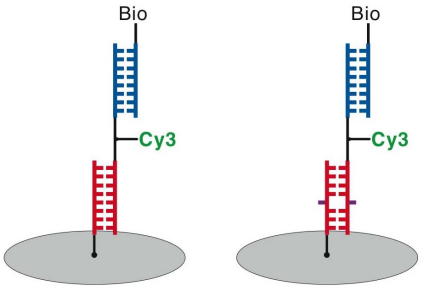

Abbildung 13: Kraftwaagen zum Nachweis von Einzelbasenfehlpaarungen: Die rechte Kraftwaage weist einen Mismatch im Probenduplex (rot) auf.

Für eine theoretische Beschreibung dieser Experimente geht man davon aus, dass die Überlebenswahrscheinlichkeit des Probenduplexes Φ_S dem Verhältnis der kraftabhängigen Dissoziationsraten des Proben-Duplexes und des Referenz-Duplexes entspricht: $\Phi_S = \lambda_R / \lambda_S$. Da bei einem Kraftwaagenexperiment an beiden Duplexen stets die gleiche Kraft anliegt, steht F in Gleichung .viii für die wahrscheinlichste Trennkraft des schwächeren der beiden Duplexe, die mit der wahrscheinlichsten Kraft, bei der die Kraftwaage getrennt wird, identisch sind.

Die Frage, wie stark λ dabei von der Bindungsweite Δx beeinflusst wird, hängt laut Gleichung .viii linear von der Größe der Trennkraft der Kraftwaage F ab, die wiederum eine logarithmische Funktion der Ladungsarte r ist (Gleichung .ix). Bei sehr kleinen Ladungsraten würde λ demnach nur noch sehr schwach mit Δx skalieren und Φ_S müsste nahe an dem Verhältnis der natürlichen Dissoziationsarten der beiden Duplexe $k_{off\,R} / k_{off\,S}$ liegen. Unter diesen Bedingungen wäre für das Beispiel der Diskriminierung eines CC-Mismatches (30 CC) von einem Perfect-Match (30 PM), wie es in P2 präsentiert wird, demnach eine extrem deutliche Diskriminierung $\Phi_S << 0{,}01$ zu erwarten, wie sich aus der folgenden Rechnung, bei der Φ_S mit dem Quotienten der natürlichen Dissoziationsraten gleichgesetzt wird, entnehmen lässt.

Eine Möglichkeit, die natürlichen Dissoziationsraten der beiden Duplexe zu errechnen, besteht darin, zuerst eine Annahme über die Assoziationsrate k_{on} treffen. Da k_{on} für 20 bp bei etwa $3 \cdot 10^4\ M^{-1}s^{-1}$ liegt [32], kann man für 30 bp ein k_{on} von mindestens $10^5\ M^{-1}s^{-1}$ erwarten. Der maximal mögliche Wert ist mit $10^6\ M^{-1}s^{-1}$ zu veranschlagen, da die Assoziationsreaktion durch die Diffusionskonstante limitiert ist [33]. Da es bei 20 bp außerdem kaum einen Unterschied zwischen den Assoziationsraten von Perfect-Matches und einzelnen Mismatches gibt, kann man im

Folgenden für 30 PM und 30 CC von $k_{on} = 10^6\ M^{-1}s^{-1}$ ausgehen. Die Dissoziationsraten lassen sich dann entsprechend Gleichung .iii und Gleichung .vi zu $k_{off}(30\ PM) = 2{,}86 \cdot 10^{-15}\ s^{-1}$ und $k_{off}(30\ CC) = 6{,}99 \cdot 10^{-12}\ s^{-1}$ berechnen. Die Überlebenswahrscheinlichkeit des Probenduplexes bei Ladungsraten gegen null wäre somit $k_{off}(30\ PM) / k_{off}(30\ CC) = 4 \cdot 10^{-4}$, also vier Größenordnungen geringer als der differenziell gemessene Unterschied zwischen $\Phi_S(30\ PM) = 0{,}4$ und $\Phi_S(30\ CC) \approx 0{,}2$). Die große Diskrepanz zwischen dem thermodynamisch zu Erwartenden und dem differenziell Gemessenen kann laut Gleichung .viii darauf zurückzuführen sein, dass der 30-CC-Proben-Duplex nicht nur über ein kleineres ΔG_{off} verfügt, sondern auch über eine kleinere Bindungsweite Δx als der Perfect-Match-Duplex, wodurch der große energetische Unterschied zwischen Perfect-Match und Mismatch bei hohen Ladungsraten zu einem großen Teil durch den geometrischen Unterschied in der Bindungsweite kompensiert wird (siehe Abb. 14).

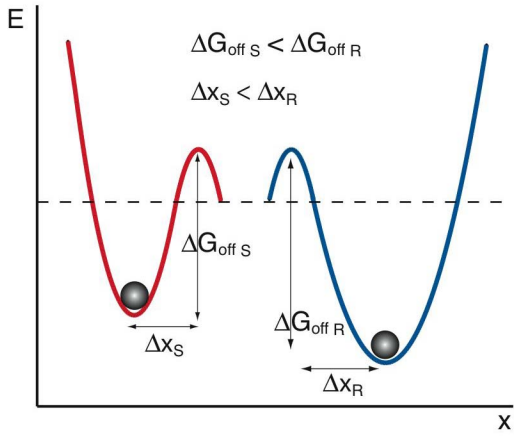

Abbildung 14: Proben-Duplex (rot) und mit kleinerem ΔG_{off} und Δx im Vergleich zum Referenzduplex (blau). Durch den kompensatorischen Effekt von ΔG_{off} und Δx kann die Trennkraft der beiden Duplexe trotz des großen Energieunterschieds sehr ähnlich ausfallen.

Eine Computersimulation, mit der man den Bindungsweitenunterschied zwischen den beiden Duplexen in Abhängigkeit von der Ladungsrate exakt berechnen kann, wurde von Gregor Neuert auf der Basis des Bell-Evans-Modells entwickelt (P3).

6.3 Der kinetische Effekt

Während die Messungen zur Zipper-Scher-Geometrie und zu den Einzelbasenfehlpaarungen durchaus den Vorhersagen entsprachen, kam es bei geschwindigkeitsabhängigen Messungen zu dem völlig unerwarteten Effekt, dass der Probenduplex oft eine viel höhere Stabilität aufwies als der Referenzkomplex. Da diese Asymmetrie ausschließlich zu beobachten war, wenn beide Duplexe im Schermodus belastet und mit Geschwindigkeiten > 5 µm/s gezogen wurden, war anzunehmen, dass die beiden Duplexe oberhalb einer kritischen Ladungsrate in verschiedenartige Entbindungspfade gezwungen werden. Die Ursache für dieses Verhalten konnte schließlich darauf zurückgeführt werden, dass bei allen bis dahin verwendeten Kraftwaagen eine Asymmetrie in der Zugrichtung vorliegt, da der Probenduplex (rot) stets in 3'-3'-Richtung, der Referenzkomplex (blau) jedoch in 5'-5'-Richtung belastet wurde. Bestätigt wurde dies durch Experimente mit gleichgerichteten Kraftwaagen, bei denen beide Duplexe in 5'-5'-Richtung belastet werden (Abb. 15) und bei denen der asymmetrische Effekt nicht auftritt (P5).

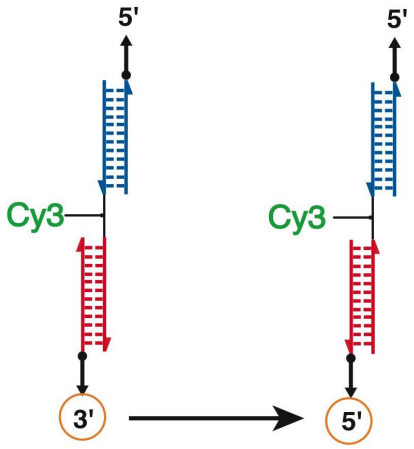

Abbildung 15: Gleichrichtung der Zugrichtung: Bei der linken Kraftwaage liegt eine Asymmetrie in der Zugrichtung vor, da der Referenzduplex (blau) in 5'-5'-Richtung und der Probenduplex (rot) in 3'-3'-Richtung belastet wird. Die rechte Kraftwaage wurde gleichgerichtet, indem die Zugrichtung des Probenduplex auf 5'-5 angeglichen wurde.

Um das Phänomen einer genaueren Analyse zu unterziehen, war es wünschenswert, die Ladungsrate zu ermitteln, bei der der asymmetrische Effekt zu beobachten ist. Im Allgemeinen ist dies bei einem Kraftwaagenversuch nicht möglich, da die Verteilung der Fluoreszenz zwischen den Oberflächen und die Trenngeschwindigkeit die einzigen direkt zugänglichen Parameter sind. Da es sich bei der verwendeten Kraftwaage jedoch um ein System handelt, das durch AFM-Messungen ausführlich charakterisiert wurde

[23], war es in diesem Fall möglich, die Ladungsrate zu errechnen. Dafür wurde zuerst die kritische Geschwindigkeit bestimmt, bei der der asymmetrische Effekt auftritt, indem der Separationsvorgang von Objektträger und Stempel mit der Methode der Reflektions-Interferenz-Kontrast-Mikroskopie (RICM) analysiert wurde. Anschließend wurde die kritische Geschwindigkeit mithilfe von Monte-Carlo-Simulationen in die wahrscheinlichste Ladungsrate (~$9 \cdot 10^5$ pN/s) und die wahrscheinlichste Trennkraft (~65 pN) umgerechnet (P4). Ein Hinweis darauf, dass 3'-3'- und 5'-5'-belastete Duplexe bei unterschiedlichen Kräften getrennt werden, wurde in [34] und [26] gefunden, wo die richtungsabhängige Deformation der Helix unter Kraft simuliert wurde. Wie in Abb. 17d dargestellt, kommt es für die beiden Richtungen zu charakteristisch unterschiedlichen Konformationen, die unterschiedliche Stabilität aufweisen können. Jedoch stellte sich daraufhin die Frage, warum dieser geometrische Unterschied in der differenziellen Messung erst ab ~$9 \cdot 10^5$ pN/s sichtbar wird und nicht schon bei niedrigeren Ladungsarten beobachtet werden kann.

Eine nahe liegende Antwort darauf war die Vermutung, dass es sich bei dem gemessenen asymmetrischen Effekt um den Übergang zu einem kinetischen Experiment handelt. Eine Annahme, die sich auf den Grundsatz stützen lässt, dass ein Kraftexperiment aus dem Quasi-Gleichgewicht-Zustand in das kinetische Regime wechselt, sobald dem System nicht genug Zeit bleibt, seinen Fluktuationsraum voll auszuschöpfen [35]. Es wurde gefolgert, dass es sich bei den Fluktuationen, die für den Trennungsvorgang der Doppelhelix relevant sein können, nur um die sogenannte „DNA-Atmung" handeln kann, also um die transiente Ausbildung von einzelsträngigen Abschnitten in einer sonst intakten Helix. Somit war es nahe liegend, einen Zusammenhang zwischen der zeitlichen Charakteristik dieser DNA-Fluktuationen und der am asymmetrischen Effekt gemessenen Ladungsrate herzustellen. Es zeigte sich, dass dies möglich ist, wenn man die Rate von „DNA-Blasen", die durch FRET-Messungen auf 10^4-10^5 /s bestimmt wurden [36], mit der Probierfrequenz ν_{off} in Gleichung .x gleichsetzt.

Hierbei handelt es sich um einen unkonventionellen Schritt, da die Probierfrequenz in der Regel nicht als freier Parameter angesehen wird. In der Theorie von Bell wird ν_{off} mit der Oszillationsfrequenz eines Atoms in einem Festkörper von 10^{13} /s gleichgesetzt [20]. In der Kramers-Theorie, bei der die viskose Dämpfung einbezogen wird, reduziert

sich ν_{off} auf 10^9-10^{10} /s [37]. Die Folge von derartig hohen Frequenzen ist, dass es praktisch unmöglich ist, die Kraft so schnell anzulegen, dass die gesamte Tiefe des Bindungspotenzials, also ΔG_{off} durch mechanische Arbeit überwunden werden kann, da dem Komplex immer noch genug Zeit bleibt, um einen Teil der Barriere durch Fluktuationen zu überwinden. Setzt man die Probierfrequenz dagegen mit den sehr viel langsameren thermischen „Oszillationen" von ~10^5 /s gleich, so erhält man eine auf Fluktuationen beruhende „thermische Leistung" $\nu_{off} \cdot k_B T$, die sehr nahe an dem Produkt aus Ladungsrate und Bindungsweite, also der mechanischen Leistung $r \cdot \Delta x$ liegt. Dies bedeutet, dass sich Gleichung .x für den Fall $\nu_{off} \cdot k_B T \approx r \cdot \Delta x$ zu $F \cdot \Delta x \approx \Delta G_{off}$ vereinfacht. Mit anderen Worten: Es gibt eine Ladungsrate, bei der die von außen geleistete mechanische Arbeit gerade so groß ist wie die vom Wärmebad geleistete Arbeit, d. h. $W_{mechan.} = W_{thermisch} = \Delta G_{off}$. Dabei muss allerdings angemerkt werden, dass das gesamte Potenzialmodell auf der Annahme beruht, dass Fluktuationen bei der Trennung des Komplexes beteiligt sind. Womit der Grenzfall $\nu_{off} \cdot k_B T = r \cdot \Delta x$, d. h. die Situation, bei der die gesamte Potenzialtiefe mechanisch überwunden wird, bereits nicht mehr durch das Potenzialmodell abgedeckt ist. In Abb. 16 ist der differenzielle Versuch in einem Doppelpotenzial dargestellt, bei dem das rote Potenzial dem Proben-Duplex und das blaue Potenzial dem Referenz-Duplex entspricht, wobei die Ladungsrate fast genau so schnell ist wie die Probierrate, wodurch nahezu die ganze Barriere durch mechanische Arbeit überwunden wird.

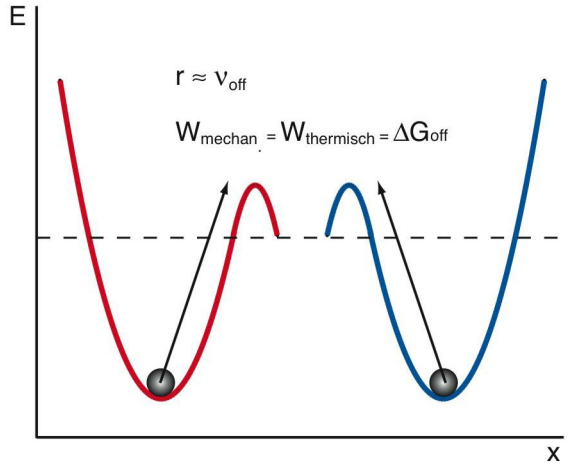

Abbildung 16: Trennung der Kraftwaage mit einer Ladungsrate *r*, die der Fluktuationsrate ν_{off} sehr nahekommt. Die Energiebarriere ΔG_{off} wird in diesem Fall fast ausschließlich durch mechanische Arbeit überwunden.

Folglich könnte es sich bei dem asymmetrischen Effekt tatsächlich um den Übergang zu einem kinetischen Experiment handeln. Bei Ladungsraten > ~$9 \cdot 10^5$ pN/s wird demnach

bereits mehr mechanische Arbeit beim Trennen des Doppelstrangs geleistet, als die Bindung an freier Gibbs'scher Energie aufweist, d. h. der Komplex ist eigentlich instabil, bleibt aber aus kinetischen Gründen noch für kurze Zeit intakt. Da die geleistete Arbeit jedoch nicht als Wärme an die Umgebung abgegeben werden kann, wird sie kinetisch gespeichert, indem die Helix deformiert wird, wie in Abb. 17d gezeigt. Entsprechend dieser Vorstellung kann man das kraftinduzierte Trennen von DNA in zwei Regime aufteilen: ein Quasi-Equilibriums-Regime moderater Ladungsraten, in dem kaum ein Unterschied in der Zugrichtung, d.h. 3'-3' oder 5'-5', festgestellt werden kann, und ein kinetisches Regime hoher Ladungsraten und hoher Kräfte, bei dem sich die geometrische Asymmetrie der DNA deutlich bemerkbar macht. Da unter diesen Bedingungen keine Zeit bleibt, die verrichtete Arbeit in Form von Wärme abzugeben, wird sie vorübergehend als potenzielle Energie, d. h. in Form einer deformierten Helix gespeichert, ehe es zum Zerreißen einer Bindung kommt. Da es sich bei der reißenden Bindung auch um den Biotin-Streptavidin-Komplex, mit dem die Waage an den Stempel gekoppelt wurde, handeln kann zeigt, dass sehr hohe Kräfte erreicht werden (P5). In diesem Licht ließe sich auch erklären, warum bei den ersten AFM-Experimenten an kurzen DNA-Duplexen extrem hohe Kräfte von mehreren hundert Piconewton gemessen wurden [38]. Tatsächlich hatte man damals keine Polymerspacer verwendet, wodurch wahrscheinlich sehr hohe Ladungsraten realisiert wurden und die DNA möglicherweise im kinetischen Regime getrennt wurde.

Das Potenzialmodel nach Bell und Evans ist demnach nur bis kurz vor Eintreten des kinetischen Effekts gültig, also in dem Bereich unterhalb der kritischen Ladungsrate, in welchem die Trennung des Duplexes auf einem Zusammenspiel von mechanischer Arbeit und „thermischer Arbeit", welche durch die DNA-Atmung geleistet wird, beruht. Demnach ist anzunehmen, dass im Bereich niedriger Ladungsraten das Öffnen von Basenpaaren von thermischen Fluktuationen angetrieben wird und dass die mechanische Arbeit nur dazu verwendet wird, die Rückreaktion, also das Schließen von Basenpaaren zu unterbinden. Dies ist in etwa mit dem Wirkungsprinzip der „Brown'schen molekularen Motoren" vergleichbar, bei dem die Vorwärtsreaktion ebenfalls durch geeignete Fluktuationen hervorgerufen wird und der Verbrauch von chemischer Energie dazu verwendet wird, um die Rückreaktion zu verhindern. Diese Anschauungsweise ist in Abb. 17 zusammengefasst: a) Bei Null-Kraft unterliegen die DNA-Duplexe Fluktuationen an ihren Enden, die sowohl zum Öffnen als auch zum

erneuten Schließen von randständigen Basenpaaren führen (gebogene Pfeile). b) Durch das Anlegen einer Kraft mit moderater Ladungsrate (< ~10^5 pN/s) wird das Schließen von bereits geöffneten Basenpaaren unterbunden (dünne vertikale Pfeile). Da auf diese Weise immer mehr Basenpaare durch Fluktuationen geöffnet werden, kommt es schließlich zur Trennung des gesamten Doppelstrangs. c) Beim Anlegen einer hohen Ladungsrate >> 10^5 pN/s wird mehr mechanische Arbeit geleistet als thermische und es kommt zum Einkoppeln der Kraft in die DNA, wodurch die Helizes deformiert werden. Dabei wird der Probenduplex (rot) aufgrund der 3'-3'-Belastung in eine andere Konformation gezwungen als der Referenz-Duplex (blau), der in 5'-5'-Richtung belastet wird. Die Folge ist, dass der 5'-5'-Duplexe bei einer niedrigeren Kraft zerreißt als der 3'-3'-Duplex.

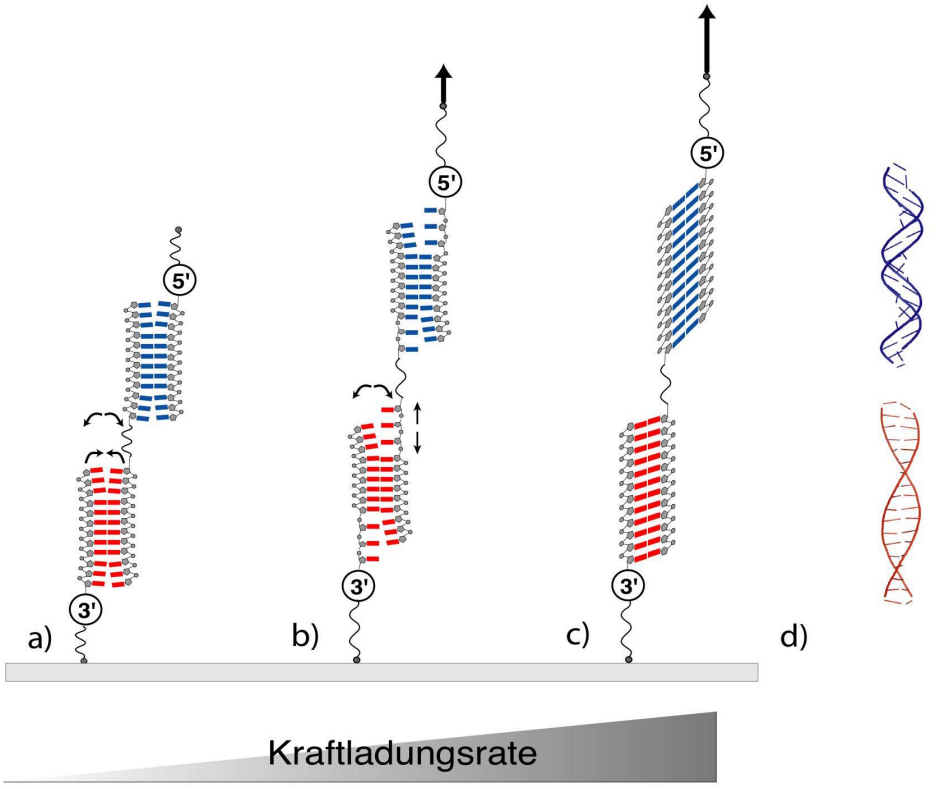

Abbildung 17: Verhalten einer Kraftwaage bei verschiedenen Ladungsraten: a) Bei Null-Kraft ist die Waage stabil, unterliegt jedoch einem beständigen Öffnen und Schließen an den Duplexenden (Pfeile). b) Bei moderaten Ladungsraten führt die angelegte Kraft dazu, dass die Rückreaktion (Schließen) unterbunden wird, wobei Fluktuationen zu einer Ausweitung des einzelsträngigen Bereichs führen. c) Bei sehr hohen Ladungsraten wird die Kraft schneller angelegt, als das Öffnen von Basenpaaren durch Fluktuationen möglich ist, deshalb kommt es zu einer gestreckten Konformation der Duplexe, die für die 3'-3'- und 5'-5'-Zugrichtung verschieden ausfallen und die unterschiedliche Trennkräfte bedingen. d) 1,3-fach gestreckte Konformationen von reinen GC-Duplexen, die den Konformationen in c) entsprechen könnten (nach [26]).

Bei den Studien, die zum Schmelzen von DNA unter Kraft veröffentlicht wurden, lassen sich zwei Hauptkategorien unterscheiden, nämlich eine, bei der kurze Duplexe

unter Kräften < 65 pN getrennt werden [23], und eine andere, bei der lange DNA unter einer konstanten Kraft von 65 pN auf etwa das 1,7-Fache ihrer Länge überstreckt wird, ehe es zur Dissoziation kommt [24], [25]. Ein wichtiger Unterschied zwischen diesen beiden Experimenten besteht außerdem darin, dass die Trennkraft eines Oligonukleotid-Duplexes mit dem Logarithmus der Ladungsrate ansteigt, das Überstrecken und Trennen der langen DNA jedoch aufgrund der konstanten Kraft von 65 pN bei Ladungsrate null vonstatten geht. Eine kontroverse Diskussion wird dabei über die Frage geführt, ob es sich bei der kraftinduzierten Trennung von DNA um einen Mechanismus handelt, bei dem es lokal zur Öffnung von Wasserstoffbrücken und zur Ausbildung von sich ausweitenden Blasen (bubbles) kommt ([28], [16], [27]) oder ob die B-Helix vielmehr kooperativ zu einer gestreckten „S-Leiter"-Konformation deformiert wird, ehe die Stränge dissoziieren [24], [26], wie in Abb. 8 dargestellt.

In der hier vorgelegten Arbeit wird dargelegt, dass beide Fälle auftreten können, je nachdem, ob das Experiment im Quasi-Equilibriums-Regime oder im kinetischen Regime durchgeführt wird. Die Frage nach dem Mechanismus entscheidet sich also daran, wie groß die mechanische Leistung ist, die dem System zugeführt wird. Der Übergang von Quasi-Gleichgewicht in den kinetischen Bereich wurde in der hier vorliegenden Arbeit durch eine Ladungsrate von $9 \cdot 10^5$ pN/s bei einer Bindungsweite von 2,8 nm gemessen, was einer Leistung von $6{,}1 \cdot 10^5$ $k_B T$/s entspricht.

Ein ähnlicher kinetischer Effekt wurde von Hauke Clausen-Schaumann für polymere DNA im Anschluss an das „B-S-Plateau" nachgewiesen [39], wenn eine Zuggeschwindigkeit von 150 nm/s überschritten wurde. Allerdings konnte bei diesen Experimenten keine Abhängigkeit der Trennkraft von der Zugrichtung festgestellt werden, möglicherweise weil die DNA nicht richtungsspezifisch angebunden wurde.

Nachdem gezeigt wurde, dass das Auftreten des kinetischen Effekts offensichtlich auf einer Korrelation von Probierfrequenz ν_{off} (=Fluktuationsrate) und Kraftladungsrate r beruht, soll versucht werden, das für die Kraftwaagenexperimente relevante ν_{off} genauer einzugrenzen. Tatsächlich kann man die in [36] angegebene Rate der DNA-Atmung von 10^4-10^5 /s (für 25 °C und 150 mM NaCl) nicht direkt auf die Experimente mit der Kraftwaage übertragen. Zwar werden in beiden Fällen mit 29 und 30 bp fast gleich lange DNA-Proben verwendet, jedoch handelt es sich dabei um Duplexe, die in der Mitte aus einem reinen AT-Abschnitt bestehen, an dem die Ausbildung interner DNA-

Blasen studiert werden kann. Die Kraftwaagen bestehen hingegen aus gemischten Sequenzen, bei denen blasenartige Fluktuationen nicht in der Mitte, sondern an den Enden der Duplexe zu erwarten sind. Dies hängt damit zusammen, dass die für eine interne DNA-Blase notwendige Nukleation, d. h. die Öffnung eines internen Basenpaares, eine relative hohe Energiebarriere überwinden muss. Da die Duplexenden hingegen einen beständigen Nukleationsdefekt aufweisen, kann man davon ausgehen, dass der Trennvorgang von außen nach innen erfolgt [40], [23], [36]. Da die mechanische Leistung $r \cdot \Delta x$ im Grenzfall gegen die thermische Leistung $\nu_{off} \cdot k_B T$ geht, entspricht ν_{off} entsprechend Gleichung .x $r \cdot \Delta x / k_B T = 5{,}4 \cdot 10^5$ /s, was bedeutet, dass an jedem Duplexende etwa jede Mikrosekunde eine Fluktuation von 1 k_BT erfolgt. Dieser Wert liegt einen Faktor zehn bis hundert niedriger als der in [36] für interne Blasen angegebene, was plausibel erscheint, wenn man berücksichtigt, dass randständige Blasen schon deshalb eine höhere Frequenz aufweisen müssen als interne, da ein stetiger Nukleationsdefekt vorliegt. Auf der anderen Seite liegt der Wert auch in realistischer Nähe zur Schließrate einer einzelnen Wasserstoffbrücke, die mit NMR auf 10^8 /s bestimmt wurde [36].

7. „Schmelzkräfte“ (nicht publiziert)

Ein verbreitetes Verfahren zur Charakterisierung von DNA-Duplexen ist die Bestimmung der Schmelztemperatur T_m. Dafür wird eine Lösung von komplementären DNA-Oligonukleotiden in eine Küvette gegeben und das Gleichgewicht zwischen doppelsträngiger und einzelsträngiger DNA anhand der Absorption der einzelsträngigen DNA bei 260 nm bestimmt. Durch Fahren einer langsamen Temperaturrampe kann somit die Schmelztemperatur bestimmt werden, d. h. die Temperatur, bei der sich das Gleichgewicht stark vom Doppelstrang zum Einzelstrang verschiebt. Vergleicht man dieses Verfahren mit einem Experiment, bei dem die Duplexe durch Anlegen einer Kraft getrennt werden, so stellt sich die Frage, warum es nicht ebenso möglich ist, eine typische „Schmelzkraft” zu messen, anhand derer man den Duplex mechanisch charakterisieren könnte[3]. Der grundlegende Unterschied zwischen beiden Experimenten liegt zunächst darin, dass beim mechanischen Trennen, im Gegensatz zum thermischen Schmelzen, keine Rückreaktion zugelassen wird. Da es sich bei der Dissoziation der DNA jedoch um einen von Fluktuationen getriebenen und somit statistischen Prozess handelt, kommt es in beiden Experimenten bereits zu einer Trennung von Duplexen, bevor ein charakteristischer Temperatur- oder Kraftwert erreicht wird. Im Fall der Schmelzkurve wirkt sich dies jedoch kaum auf die Messung aus, da gleichzeitig zur Dissoziation auch eine Reassoziation von Einzelsträngen stattfindet, weshalb das Maßsignal unterhalb des Schmelzpunktes nahezu konstant bleibt. Aus Gleichung .vii erkennt man, dass die Schmelztemperatur erreicht ist, sobald das Produkt der Entropie ΔS und der absoluten Temperatur T gerade so groß wird wie ΔH, womit ΔG gleich null wird.

Aus dem im vorigen Kapitel Gesagten kann geschlossen werden, dass eine charakteristische Schmelzkraft genau dann gemessen wird, wenn das System gerade in den kinetischen Bereich übergeht bzw. wenn die gesamte Potenzialtiefe ΔG_{off} durch mechanische Arbeit überwunden wird. Es konnte außerdem gezeigt werden, dass dieser Fall bei kurzen Duplexen dann eintritt, wenn die mechanische Leistung $P_{mechan.} = r \cdot \Delta x$

[3] An dieser Stelle muss angemerkt werden, dass es sich bei der Trennkraft um eine intensive Zustandsgröße eines einzelnen Moleküls handelt, bei der Temperatur aber um eine makroskopische, extensive Zustandsgröße, die nicht direkt miteinander verglichen werden können. Setzt man die Temperatur jedoch gedanklich mit einem “Anregungszustand” der DNA gleich, das heißt man geht bei hohen Temperaturen der Lösung von proportional energiereicheren Fluktuationen der Helix aus, so ist der Vergleich gestattet.

gerade so groß ist wie die thermische Leistung $P_{thermisch} = \nu_{off} \cdot k_B T$. Wenn man davon ausgeht, dass die Fluktuationsrate ν_{off}, die für den 30 bp-Duplex bestimmt wurde, auch für kürzere Duplexe gilt, so ist es möglich, eine Vorhersage zu treffen, bei welcher Ladungsrate und bei welcher Kraft (= Schmelzkraft) ein Oligonukleotidduplex in den kinetischen Bereich übergeht. Dies soll hier an einem Beispiel eines 16-bp-Duplex gezeigt werden, für den die Dissoziationsrate mit SPR bestimmt wurde [41].

Um die Schmelzkraft F_m zu berechnen, bestimmt man zuerst die Bindungsweite Δx für sechzehn Basenpaare zu $\Delta x = 1{,}82$ nm (Gleichung .xi). Durch Einsetzen der Bindungsweite, der Dissoziationsrate $k_{off} = 7{,}41 \cdot 10^{-4}$ /s und der mechanischen Leistung $r \cdot \Delta x = \nu_{off} \cdot k_B T = 6{,}1 \cdot 10^5$ k_BT/s = $2{,}5 \cdot 10^6$ pN·nm/s in Gleichung .ix errechnet sich F_m zu 47 pN bei einer Ladungsrate $r = P_{mechan.} / \Delta x = 1{,}4 \cdot 10^6$ pN/s. Eine Abschätzung, die bei einem Vergleich mit denen in [23] veröffentlichten Werten, die für 10-bp- und 20-bp-Duplexen im Bereich zwischen 40-50 pN liegen, als durchaus realistisch erscheint.

8. DNA-Interkalatoren (nicht publiziert)

Nachdem der Einfluss struktureller Modifikationen auf die Kraftwaage eingehend studiert wurde, war es interessant, auch die Auswirkung von DNA-Liganden auf die Kraftwaage zu untersuchen. Bei der am weitesten verbreiteten Klasse von DNA-bindenden Molekülen handelt es sich um Interkalatoren, die starke π-π-Wechselwirkungen mit DNA-Basen ausbilden und dadurch eine starke Stabilisierung der Doppelhelix bewirken [42].

Es stellte sich allerdings das Problem, einen Interkalator zu finden, der nur an einen der beiden Duplexe der Kraftwaage bindet und auf diese Weise die Symmetrie der Kraftwaage bricht. Zwar gibt es Interkalatoren, die eine gewisse Sequenzpräferenz aufweisen, jedoch waren diese für den angestrebten Zweck viel zu unspezifisch. Die Lösung für dieses Problem bestand darin, einen Interkalator zu verwenden, der spezifisch an die rechtsgewundene Form der Doppelhelix bindet. Diese Substanz, die unter dem Namen Daunorubicin oder Daunomycin in der Chemotherapie Verwendung findet, interagiert über einen Mechanismus, bei dem die planare Ringstruktur des Liganden zwischen benachbarte Basen der Doppelhelix interkaliert, wobei der chirale Zuckeraminrest (Daunosamin) in die kleine Furche der DNA greift (Abb. 18) [43].

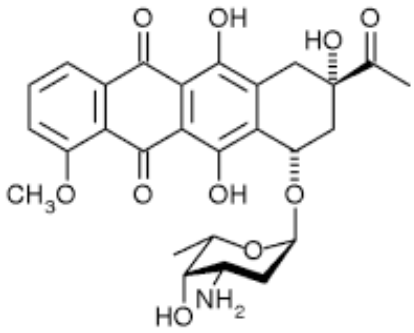

Abbildung 18: d-Enantiomer des Interkalators Daunorubicin. Die Präferenz für rechtsgängige DNA wird durch die Zuckeramingruppe vermittelt.

Da es bekannt ist, dass die d-Form von Daunorubicin mit einer 20-mal höheren Affinität an rechtshändige B-DNA bindet als an linkshändige Z-DNA [44], war es anzunehmen, dass das selbe Enantiomer auch eine stark verminderte Affinität für l-DNA (also künstliche DNA mit Nukleotiden aus l-Ribose) aufweisen sollte, was durch Schmelztemperaturmessungen bestätigt werden konnte (Daten nicht gezeigt). Deshalb wurde eine Kraftwaage mit einem Referenzduplex aus l-DNA und einem Proben-

Duplex aus d-DNA konstruiert. Hierbei handelt es sich wiederum um eine gleichgerichtete Kraftwaage (vgl. Abb. 15), bei der beide Duplexe in 5'-5'-Richtung belastet werden und bei der beide Duplexe auf der Probensequenz der Kraftwaage aus P4 und P5 beruhen.

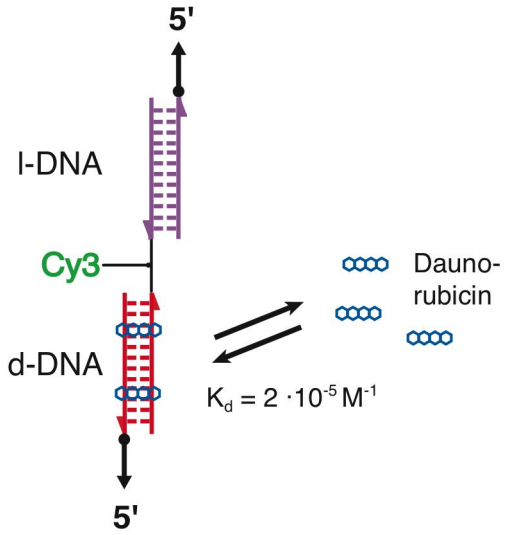

Abbildung 19: Kraftwaage mit Referenz-Duplex aus linksgängiger l-DNA (violett) und einem Proben-Duplex aus rechtshändiger d-DNA. Der Interkalator Daunorubicin bindet mit starker Präferenz an den rechtsgängigen Duplex.

In Abb. 20 sind Messungen zusammengefasst, bei denen die Kraftwaage in Abb. 19 mit verschiedenen Konzentrationen von Daunorubicin in 1 x SSC-Puffer inkubiert und mit 200 nm/s getrennt wurde. In dem Graphen wurde die Überlebenswahrscheinlichkeit des Proben-Duplexes Φ_S und die Kopplungseffizienz (vgl. P2) gegen Daunorubicin-Konzentration aufgetragen.

Offensichtlich führt die Interkalation von Daunorubicin in den Proben-Duplex aus d-DNA zu einer starken Stabilisierung des Duplexes, wie aus dem Anstieg der Überlebenswahrscheinlichkeit von Φ_S = 0,64 bei 0,1 nM auf Φ_S = 0,91 bei 500 nM Daunorubicin zu schließen ist. Ab 1000 nM ist festzustellen, dass sowohl Φ_S als auch die (scheinbare) Kopplungseffizienz abnehmen. Dies kann man wahrscheinlich darauf zurückführen, dass Daunorubicin bei höheren Konzentrationen auch an l-DNA bindet, wodurch es zu einer Stabilisierung beider Duplexe und folglich zur Trennung von Biotin-Oligonukleotiden und Streptavidin kommt, ähnlich wie in P5 für sehr hohe Ladungsraten beschrieben.

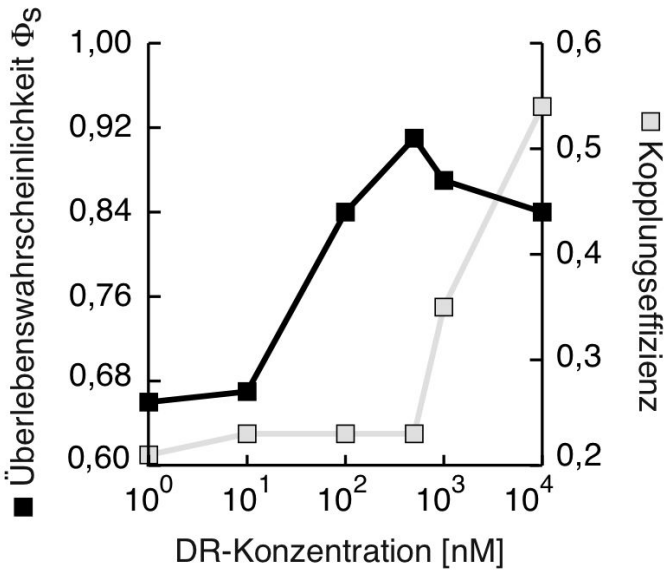

Abbildung 20: Überlebenswahrscheinlichkeit des d-DNA-Probenduplexes Φ_S und Kopplungseffizienz über die Konzentration von Daunorubicin geplottet.

Die besondere Bedeutung dieses Versuches beruht auf der Tatsache, dass DNA-Liganden als Medikamente insbesondere in der Krebstherapie Verwendung finden. Allerdings wird aufgrund der teilweise erheblichen Nebenwirkungen der unspezifischen Interkalatoren intensiv an Designersubstanzen gearbeitet, die in der kleinen Furche der DNA binden und möglichst für eine einzige Zielsequenz im menschlichen Genom spezifisch sein sollen [45]. Die Kraftwaage könnte sich hierbei als ein nützliches Hilfsmittel erweisen.

9. Ausblick

In der vorliegenden Arbeit wurden in grundlegender Weise die Möglichkeiten der differenziellen Messung von molekularen Bindekräften aufgezeigt. Dabei wurde mit den synthetischen DNA-Oligonukleotiden ein System gewählt, dessen großer Vorteil darin besteht, dass eine Vielzahl von Strukturen und chemischen Modifikationen einfach hergestellt werden kann. Durch eine präzise Kontrolle der Umgebungsparameter konnten an diesem Modellsystem sehr sensitive und reproduzierbare Messungen durchgeführt werden und selbst Details der DNA-Mechanik aufgelöst werden, die mit anderen Techniken bisher nicht zugänglich waren.

Die Verwendung von DNA in differenziellen Messungen kann auf dieser Basis in zwei wesentliche Richtungen weiterentwickelt werden. Zum einen ist es möglich, kurze DNA-Duplexe als Kraftsensoren zu verwenden, mit denen andersartige Rezeptor-Ligand-Interaktionen vermessen werden können, und zum anderen kann die Interaktion von freien Liganden mit der Doppelhelix studiert werden. Für eine Untersuchung von DNA-bindenden Proteinen steht man dabei allerdings vor der Aufgabe, längere Kraftwaagen, in etwa durch PCR, zu konstruieren.

Eine nahe liegende Anwendung ist es, auf der Basis der Interkalator-Versuche die Kraftwaage dazu zu verwenden, um die DNA-bindenden Liganden mit pharmazeutischem Potenzial zu untersuchen, eine Möglichkeit, die bei Forschern aus dem Bereich der Chemical Genomics bereits auf großes Interesse gestoßen ist und derzeit in einer Kooperation verfolgt wird.

10. Literatur

1. Brown, R., *A brief account of microscopical observations.* Philosophical Journal, 1828. **July-September 1828**: p. 358-371.

2. Ford, B., *Brownian movement in Clarkia pollen: A reprise of the first observations.* The Microscope, 1992. **40**(4): p. 235-241.

3. Einstein, A., *Über die von der molekulartheoretischen Theorie der Wärme geforderten Bewegung von in ruhenden Flüssigkeiten suspendierten Teilchen.* Annalen der Physik, 1905. **17**: p. 549-560.

4. Weiss, S., *Fluorescence spectroscopy of single biomolecules.* Science, 1999. **283**(5408): p. 1676-83.

5. Astumian, R.D., *Thermodynamics and Kinetics of a Brownian Motor.* Science, 1997. **276**(5314): p. 917-922.

6. Frey, E. and K. Kroy, *Brownian motion: a paradigm of soft matter and biological physics.* Annalen der Physik, 2004. **14**(1-3): p. 20-50.

7. Florin, E.L., V.T. Moy, and H.E. Gaub, *Adhesion forces between individual ligand-receptor pairs.* Science, 1994. **264**(5157): p. 415-7.

8. Leckband, D.I., J, *Intermolecular forces in biology.* Quarterly Reviews of Biophysics, 2001. **34**(2): p. 105-267.

9. Albrecht, C., H. Clausen-Schaumann, and H. Gaub, *Differential analysis of biomolecular rupture forces.* Journal of Physics: Condensed Matter, 2006. **18**: p. S581-S599.

10. Gittes, F. and C.F. Schmidt, *Thermal noise limitations on micromechanical experiments.* Eur Biophys J, 1998. **27**: p. 75-81.

11. Blackburn, G.M. and M.J. Gait, *Nucleic acids in chemistry and biology*. 2nd ed. ed. 1996, Oxford: Oxford University Press.

12. *http://www.chemgapedia.de/vsengine/printvlu/vsc/de/ch/15/thc/bindung/tc022_h2plus.vlu.html*.

13. Barbi, M., S. Cocco, and M. Peyrard, *Helicoidal model for DNA opening.* Physics Letter A, 1999. **253**: p. 358-369.

14. Sen, S. and L. Nilsson, *MD simulations of homomorphous PNA, DNA, and RNA single strands: characterization and comparison of conformations and dynamics.* J Am Chem Soc, 2001. **123**(30): p. 7414-22.

15. Vesnaver, G. and K.J. Breslauer, *The contribution of DNA single-stranded order to the thermodynamics of duplex formation.* Proc Natl Acad Sci U S A, 1991. **88**(9): p. 3569-73.

16. Rouzina, I. and V.A. Bloomfield, *Force-induced melting of the DNA double helix 1. Thermodynamic analysis.* Biophys J, 2001. **80**(2): p. 882-93.

17. Breslauer, K.J., et al., *Predicting DNA duplex stability from the base sequence.* Proc Natl Acad Sci U S A, 1986. **83**(11): p. 3746-50.

18. SantaLucia, J., Jr., *A unified view of polymer, dumbbell, and oligonucleotide DNA nearest-neighbor thermodynamics.* Proc Natl Acad Sci U S A, 1998. **95**(4): p. 1460.

19. *http://jsl1.chem.wayne.edu/Hyther/hythermenu.html*.

20. Bell, I.G., *Models for the Specific Adhesion of Cells to Cells.* Science, 1978. **200**(4342): p. 618-627.

21. Evans, E. and K. Ritchie, *Dynamic strength of molecular adhesion bonds.* Biophys J, 1997. **72**(4): p. 1541-55.

22. Kramers, H.A., *Brownian motion in a field of force and the diffusion model of chemical reactions.* Physica, 1940. **7**: p. 284-304.

23. Strunz, T., et al., *Dynamic force spectroscopy of single DNA molecules.* Proc Natl Acad Sci U S A, 1999. **96**(20): p. 11277-82.

24. Cluzel, P., et al., *DNA: an extensible molecule.* Science, 1996. **271**(5250): p. 792-4.

25. Smith, S.B., Y. Cui, and C. Bustamante, *Overstretching B-DNA: the elastic response of individual double-stranded and single-stranded DNA molecules.* Science, 1996. **271**(5250): p. 795-9.

26. Lebrun, A. and R. Lavery, *Modelling extreme stretching of DNA.* Nucleic Acids Res, 1996. **24**(12): p. 2260-7.

27. Harris, S.A., Z.A. Sands, and C.A. Laughton, *Molecular dynamics simulations of duplex stretching reveal the importance of entropy in determining the biomechanical properties of DNA.* Biophys J, 2005. **88**(3): p. 1684-91.

28. Marko, F.M. and E.D. Siggia, *Stretching DNA.* Macromolecules, 1995. **28**: p. 8759-8770.

29. Essevaz-Roulet, B., U. Bockelmann, and F. Heslot, *Mechanical separation of the complementary strands of DNA.* Proc Natl Acad Sci U S A, 1997. **94**(22): p. 11935-40.

30. Lang, M.J., et al., *Simultaneous, coincident optical trapping and single-molecule fluorescence.* Nat Methods, 2004. **1**(2): p. 133-9.

31. Sapolsky, R.J., et al., *High-throughput polymorphism screening and genotyping with high-density oligonucleotide arrays.* Genet Anal, 1999. **14**(5-6): p. 187-92.

32. Sauer, M., et al., *Interaction of chemically modified antisense oligonucleotides with sense DNA: a label-free interaction study with reflectometric interference spectroscopy.* Anal Chem, 1999. **71**(14): p. 2850-7.

33. Northrup, S.H. and H.P. Erickson, *Kinetics of protei-protein association explained by Brownian dynamics computer simulation.* Proc Natl Acad Sci U S A, 1992. **89**: p. 3338-3342.

34. Lavery, R. and A. Lebrun, *Modelling DNA stretching for physics and biology.* Genetica, 1999. **106**(1-2): p. 75-84.

35. Tinoco, I., Jr. and C. Bustamante, *The effect of force on thermodynamics and kinetics of single molecule reactions.* Biophys Chem, 2002. **101-102**: p. 513-33.

36. Altan-Bonnet, G., A. Libchaber, and O. Krichevsky, *Bubble dynamics in double-stranded DNA.* Phys Rev Lett, 2003. **90**(13): p. 138101.

37. Evans, E., *Probing the relation between force--lifetime--and chemistry in single molecular bonds.* Annu Rev Biophys Biomol Struct, 2001. **30**: p. 105-28.

38. Lee, G.U., L.A. Chrisey, and R.J. Colton, *Direct measurement of the interaction forces between complementary strands of DNA with atomic force microscopy.* Science, 1994. **266**: p. 771-774.

39. Clausen-Schaumann, H., et al., *Mechanical stability of single DNA molecules.* Biophys J, 2000. **78**(4): p. 1997-2007.

40. Pörschke, D. and M. Eigen, *Co-operative non-enzymic base recognition. 3. Kinetics of the helix-coil transition of the oligoribouridylic--oligoriboadenylic acid system and of oligoriboadenylic acid alone at acidic pH.* J Mol Biol, 1971. **62**(2): p. 361-81.

41. Yu, F., D. Yao, and W. Knoll, *Oligonucleotide hybridization studied by a surface plasmon diffraction sensor (SPDS).* Nucleic Acids Res, 2004. **32**(9): p. e75.

42. Krautbauer and H. Gaub, *Mechanical Fingerprints of DNA Drug complexes.* single molecules, 2002. **3**: p. 2-3.

43. Wang, A.H., et al., *Interactions between an anthracycline antibiotic and DNA: molecular structure of daunomycin complexed to*

d(CpGpTpApCpG) at 1.2-A resolution. Biochemistry, 1987. **26**(4): p. 1152-63.

44. Qu, X., et al., *Allosteric, chiral-selective drug binding to DNA.* Proc Natl Acad Sci U S A, 2000. **97**(22): p. 12032-7.

45. Dervan, P.B., *Design of sequence-specific DNA-binding molecules.* Science, 1986. **232**(4749): p. 464-71.

11. Anhang (Publikationen)

P1) DNA: A programmable force sensor

Christian Albrecht,Kerstin Blank, Mio Lalic-Mühlthaler, Siegfried Hirler, Thao Mai, Ilka Gilbert, Susanne Schiffmann, Tom Bayer, Hauke Clausen-Schaumann, Hermann E. Gaub

Science, 2003, 301, p. 367-370

P2) Differential analysis of molecular rupture forces

Christian Albrecht, Hauke Clausen-Schaumann, Hermann E. Gaub

Journal of Physics, Condensed Matter, 2006, 18, p. S581-S599

P3) Predicting the rupture probabilities of molecular bonds in series

Gregor Neuert, Christian H. Albrecht, Hermann E. Gaub

Biophysical Journal, 2007, **Accepted**

P4) Dynamic force spectroscopy with a molecular balance

Christian Albrecht, Gregor Neuert, Robert A. Lugmaier, Hermann E. Gaub

European Biophysics Journal, 2007, **Submitted**

P5) dsDNA unbinds under force dependent pathways

Christian Albrecht, Gregor Neuert, Robert A. Lugmaier, Hermann E. Gaub

Nucleic Acids Research, 2007, **Submitted**

P1) DNA: A programmable force sensor

Christian Albrecht,Kerstin Blank, Mio Lalic-Mühlthaler, Siegfried Hirler, Thao Mai, Ilka Gilbert, Susanne Schiffmann, Tom Bayer, Hauke Clausen-Schaumann, Hermann E. Gaub

Science, 2003, 301, p. 367-370

9. D. M. Wellik, P. J. Hawkes, M. R. Capecchi, *Genes Dev.* **16**, 1423 (2002).
10. G. M. Wahba, S. L. Hostikka, E. M. Carpenter, *Dev. Biol.* **231**, 87 (2001).
11. D. M. Wellik, M. R. Capecchi, data not shown.
12. S. L. Hostikka, M. R. Capecchi, *Mech. Dev.* **70**, 133 (1998).
13. Y. Herault, J. Beckers, M. Gerard, D. Duboule, *Dev. Biol.* **208**, 157 (1999).
14. P. Dolle, J. C. Izpisua-Belmonte, H. Falkenstein, A. Renucci, D. Duboule, *Nature* **342**, 767 (1989).
15. P. Dolle, J. C. Izpisua-Belmonte, J. M. Brown, C. Tickle, D. Duboule, *Genes Dev.* **5**, 1767 (1991).
16. B. Favier *et al.*, *Development* **122**, 449 (1996).
17. M. Suzuki, A. Kuroiwa, *Mech. Dev.* **118**, 241 (2002).
18. M. Hildebrand, *Analysis of Vertebrate Structure* (Wiley, New York, ed. 4, 1995).
19. E. B. Lewis, *Nature* **276**, 565 (1978).
20. M. J. Cohn, C. Tickle, *Nature* **399**, 474 (1999).
21. M. Kmita, B. Tarchini, D. Duboule, Y. Harault, *Development* **129**, 5521 (2002).
22. We are indebted to S. L. Hostikka for preparation of the *Hoxc10* and *Hoxc11* mutant mice, and we thank J. F. Fallon, S. Sakonju, and B. W. Bisgrove for discussions of these data before publication.

Supporting Online Material
www.sciencemag.org/cgi/content/full/301/5631/363/DC1
SOM Text
References

14 April 2003; accepted 9 June 2003

DNA: A Programmable Force Sensor

Christian Albrecht,[1] Kerstin Blank,[1] Mio Lalic-Mülthaler,[1] Siegfried Hirler,[1] Thao Mai,[1] Ilka Gilbert,[1] Susanne Schiffmann,[1] Tom Bayer,[1] Hauke Clausen-Schaumann,[1]* Hermann E. Gaub[2]

Direct quantification of biomolecular interaction by single-molecule force spectroscopy has evolved into a powerful tool for materials and life sciences. We introduce an approach in which the unbinding forces required to break intermolecular bonds are measured in a differential format by comparison with a known reference bond (here, a short DNA duplex). In addition to a marked increase in sensitivity and force resolution, which enabled us to resolve single–base pair mismatches, this concept allows for highly specific parallel assays. This option was exploited to overcome cross-reactions of antibodies in a protein biochip application.

Within the past decade, a variety of experimental tools based on applying and measuring piconewton forces between single molecules have been developed and have contributed to a better understanding of the mechanics of biomolecules and molecular bonds (*1–4*). Force measurements reveal detailed insights into binding-potential landscapes and into functional aspects of the molecules under investigation, and as a result, force has become a new structural and functional parameter in materials and life sciences. Receptor-ligand pairs (*5–8*), protein and nucleic acid structures (*9–15*), and even covalent bonds (*16*) have been investigated, and it has become evident that biomolecular processes are governed by piconewton forces. However, two major bottlenecks have hindered the widespread use of single-molecule mechanics: sizable instrumental effort and limited force resolution. To our knowledge, no single–base pair mismatch detection by single-molecule force measurements has been reported, despite numerous efforts. The best resolution to date has been 10 base pairs (bp), obtained by shearing and unzipping short oligomers by atomic force micoscopy (AFM) (*17*, *18*).

In conventional single-molecule force spectroscopy, inter- or intramolecular forces are exerted and measured with microscopic force sensors like AFM cantilevers or beads in optical or magnetic traps (*19*, *20*). With state-of-the-art instrumentation, the force resolution is limited only by thermal fluctuations that are detected by the force sensor. Arguments based on the fluctuation-dissipation theorem predict that a reduction of the sensor size should improve the signal-to-noise ratio (*21*). This has been verified in experimental studies using a new generation of small AFM cantilevers (*22*). The logical extrapolation is to replace the cantilever by a single elastic molecule. To increase the precision of the assay even further, we chose a differential measurement format, where rupture forces of two molecular complexes are directly compared with each other. This differential format offers several advantages. Because of the high symmetry of the assay, most external disturbances cancel out (*23*). In addition, for most applications, a precise measure of the difference is more valuable than two absolute values with their respective error bars, such as the ranking of binders or a single–base pair mismatch detection in a DNA sequence.

In our setup (Fig. 1), the cantilever spring was replaced by a polymeric anchor and a known molecular bond (reference bond) carrying a fluorescence label. The molecular bond under investigation was directly compared to this reference bond, which served as a molecular force standard. During separation of the two surfaces, the polymeric anchor was stretched, and the force acting along the molecular chain consisting of the sample and labeled reference complex built up gradually, until the weaker of the two bonds ruptured. The difference in the stability of the two bonds breaks the symmetry in this experiment. As a result, there is a higher probability that the fluorescence label will end up on the side of the stronger bond rather than on the side of the weaker bond. This process can be seen as a 1-bit analog-to-digital conversion broadened by thermal fluctuations (*24*). Many single-molecule force measurements can be performed simultaneously, using two congruent chip surfaces and different spots containing the molecules of interest. Counting the labels on each side, for instance, by single-molecule optics, provides a quantitative measure for the differences between the distributions of the bond rupture probabilities of the two molecular complexes. It is equivalent to measuring the fluorescence intensities, which are proportional to the densities of the fluorescence labels (*25*). Although a large number of molecules are probed simultaneously, the actual force measurement is still performed at the single-molecule level, because each sample bond is probed individually by a single reference bond.

Figure 1B illustrates the setup schematically. The rupture forces of two DNA strands with different hybridization lengths (a 20-bp duplex and a 25-bp duplex) are directly compared. Both oligonucleotides are bridged with a conjugated 65-base oligonucleotide, carrying a terminal Cy5 fluorescent label. The resulting 20-bp duplex is coupled to an activated glass surface, and the 25-bp duplex to a soft polydimethylsiloxane (PDMS) stamp (*26–28*), both by means of polyethylene glycol (PEG) spacers. Figure 1C shows fluorescence images of the glass surface containing the capture oligonucleotide and the labeled sample oligonucleotide before the two surfaces were brought into contact and separated again, and both glass (bottom) and PDMS (top) after the separation of the two surfaces. Because the PDMS stamp has a grid pattern of trenches to ease the water flux at the surface during separation, the transferred labels form a checkerboard pattern on the PDMS. No transfer occurred in the trenches, so that here the initial label density was maintained on the glass surface, whereas in the contact areas (squares), labels were transferred from the glass to the PDMS side.

[1]Nanotype GmbH, Lochhamer Schlag 12, 82166 Gräfelfing, Germany. [2]Lehrstuhl für Angewandte Physik and Center for Nano-Science, Amalienstrasse 54, 80799 München, Germany.

*To whom correspondence should be addressed. E-mail: hauke.clausen-schaumann@nanotype.de

A direct quantification of the fluorescent label density is limited by the different optical and chemical properties of the two surfaces—glass chip and PDMS stamp—which influence the quantum yield and the excitation efficiency of the label. In addition, the coupling efficiencies to the two chip surfaces may differ. However, the symmetry of the experiment can be restored by placing the two molecules of interest on the same side of the assay and measuring both against a common reference on the other side (*29*). This is the format chosen for the following experiments, where single–base pair mismatches and different binding modes of DNA were investigated. A quantitative analysis of the experiment that is shown in Fig. 1 is provided in fig. S1.

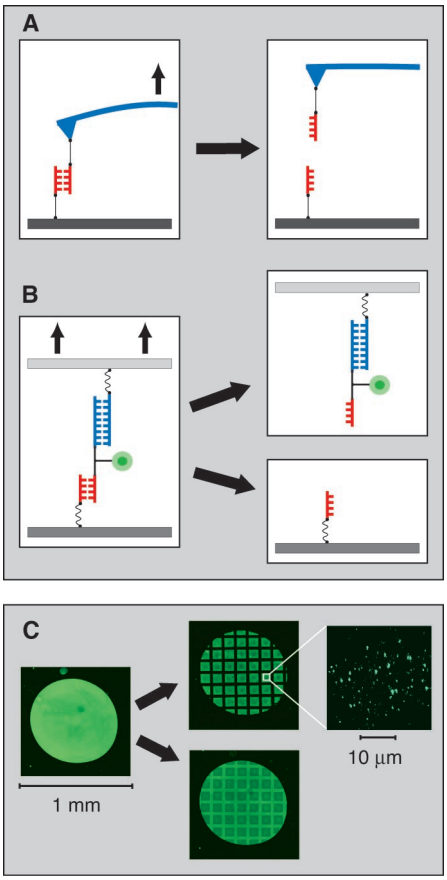

Fig. 1. (**A**) Conventional, AFM-based single-molecule force spectroscopy, in which the rupture force required to break a molecular bond, such as a DNA duplex (red), is measured with a cantilever spring (blue). (**B**) The differential force test, in which the rupture force of a sample bond (red) is measured by comparing it with a known reference bond (blue), which serves as a molecular force standard. Upon loading the chain of polymer spacers, sample bond, and reference bond, the weaker bond has a higher probability of rupturing than the stronger one. Consequently, most of the probed fluorescence labels (green) end up with the stronger bond after separating the two surfaces. (**C**) (left) Cy5 fluorescence image of a spot containing the molecular chains of polymer spacers, sample, and reference duplexes before connecting the biotinylated reference duplexes to the second chip surface. (middle) Cy5 fluorescence image of both chip surfaces—microstructured PDMS (top) and glass (bottom)—after separating them again. (right) PDMS surface at single-molecule resolution after separating the two surfaces. The image was obtained by TIRF.

To investigate the force resolution of the differential force test, we measured the reduction of the unbinding forces caused by a single–base pair mismatch in a 20-bp DNA duplex. Figure 2A illustrates the experimental setup and shows the superposition of the histograms of fluorescence intensities, obtained on the PDMS surface, after separating the two chips. The main peaks of the two histograms are clearly separated and are to a good approximation of Gaussian shape, indicating a homogeneous surface coverage with statistical distribution of the bond-rupture process. The spike (to the left) stems from the trenches of the grid and reflects the fluorescence background. The mean fluorescence intensities were determined by fitting Gaussian distributions to the histogram peaks. The ratio of these intensities, which directly represents the ratio of the bond-rupture probabilities of mismatch to perfect match was found to be 1.7. Because the half width of the two peaks is less than one-third of the difference of the peak values, a quantitative single-nucleotide polymorphism assay with high precision is possible. The experiment was conducted in a buffer solution containing 150 mM NaCl at room temperature. Under these conditions, thermal off-rates are extremely low (*30*), and discrimination between mismatch and perfect match sequences is difficult to obtain in conventional equilibrium binding assays (*31*, *32*). This high thermal stability ensures that in the force-based assay, the data are not obscured by spontaneous strand-separation events or differences in hybridization efficiencies (*33*).

On conventional DNA chips, single–base pair mismatches are detected by identifying differences in the thermal off-rate or the equilibrium constant. In both cases, stringent conditions are established by reducing the salt concentration (or alternatively increasing temperature) such that the DNA duplexes to be analyzed either dissociate at different time scales or bind with distinguishable binding ratios (*34*). Because both ionic strength and temperature are global parameters, a delicate compromise of these parameters has to be chosen to establish satisfactory ambient conditions for all the different spots on the chip. These global boundary conditions impose severe limitations on the sequences that can be tested in parallel on the same chip and require large numbers of additional control spots (*35*, *36*). In contrast, in the differential force for-

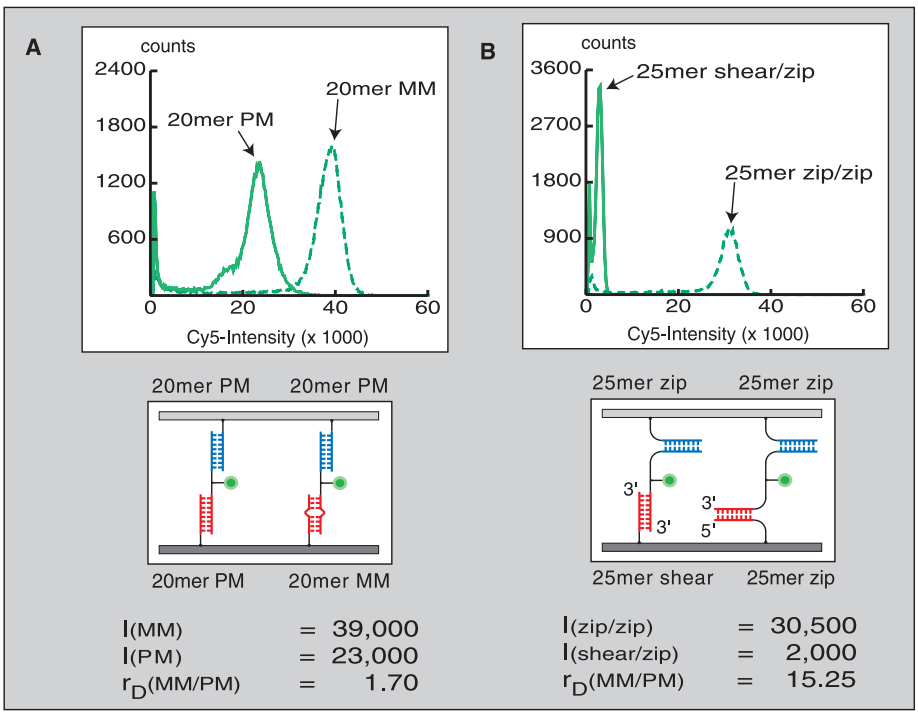

Fig. 2. (**A**) Histograms of a perfectly matching (PM) 20-bp DNA duplex (left) as compared with a 20-bp duplex that has a single–base pair mismatch (MM). Both duplexes were probed with a 20-bp reference complex that is reverse to the perfectly matching 20-bp duplex. Both sample duplexes are identical, except for a single base mutation (G → C) that was introduced at position 13 of the capture oligonucleotide. (**B**) Histograms of identical 25-bp DNA duplexes in both shear (left) and unzip geometry (right), both of which have been probed with an identical 25-bp duplex in unzip geometry. I, mean fluorescence intensity; r_D, discrimination ratio.

mat, the stringency imposed by the reference complex is a local boundary condition. Both the sequence and the length of the reference complex on the stamp may be chosen for every sample spot on the chip accordingly, allowing optimum force resolution and background discrimination for every spot. Thermodynamic stringency is global, whereas mechanical stringency is local. The combination of maximum resolution and local stringency is desirable for the precise quantification of interactions.

Figure 2B highlights an additional and unique feature of force-based assays: the discrimination among energetically and kinetically equivalent interactions. Both hybrids, the one in shear geometry and the one in unzip geometry, have identical sequences and, therefore, have the same binding energy, as well as the same thermal on-rates and off-rates. However, upon forced dissociation, the complex in unzip geometry has a probability of rupturing that is more than 15 times as high as that of the complex in shear geometry, as can be derived from the peak positions of the histograms in Fig. 2B. This pronounced difference is consistent with earlier measurements (*13*, *17*, *37*, *38*) in which unzipping forces of 14 pN and values that were more than three times as high for the shear geometry were measured under comparable conditions (*39*).

The discrimination between different binding modes, as illustrated above, and the concept of mechanical stringency offer striking advantages when applied to the field of protein arrays. In this field, it is crucial to discriminate between specific and nonspecific interactions, and it is difficult to define a common set of stringent ambient conditions for many different proteins (*40*, *41*). Proteins typically interact with each other specifically over well-defined binding sites, whereas nonspecific interactions with other proteins and with surfaces occur over larger surface areas (*42*). As shown in Fig. 2B, discrimination between these two binding modes can then be reliably achieved using a low-force but high-affinity force sensor, such as a DNA duplex in unzip conformation. Figure 3 shows that the threshold force defined by such a DNA duplex in unzipping geometry is well suited to discriminate between specific and nonspecific binding for a variety of antibody-antigen interactions. At the same time, the affinity is high enough to provide a stable anchor. The antibodies can be safely "delivered" to their respective antigens. In addition, if needed, other threshold forces can easily be programmed into the DNA reference complex by changing the base composition or the binding geometry.

The advantages of the force-based delivery of antibodies become more apparent when applied to capture arrays based on a sandwich format. In conventional sandwich arrays, each detection antibody can interact with all spots of the array. Therefore, each analyte molecule that is bound to the array can be decorated by detection antibodies, even the ones that are bound nonspecifically or because of cross-reactive capture antibodies (*43*). Consequently, the nonspecific background and the number of false-positives grow geometrically with the number of spots on the chip, which severely limits the multiplexing capabilities of protein capture arrays (*44*). The differential force assay allows for the local application of specific detection antibodies, and the second chip surface therefore provides for a second dimension of specific encoding (*45*). Figure 4 shows an example of a cross-reactive capture antibody that is specific for both human and murine interleukin-5 (IL-5). In a conventional protein array, discrimination between human and murine antigens is not possible (Fig. 4A) with this capture antibody, and the assay generates false-positive results (*46*). In our assay, the second chip surface (top surface) allows the definition of two specific spots for the two different antigens, even if the same cross-reactive capture antibody is used in both spots of the capture surface (bottom). Specific detection and reliable discrimination of both antigens are now possible in a single step. This illustrates the potential of our assay to overcome a major bottleneck in the field of protein biochips, namely, the lack of specificity caused by nonspecific interactions and cross-reactions (*47*, *48*).

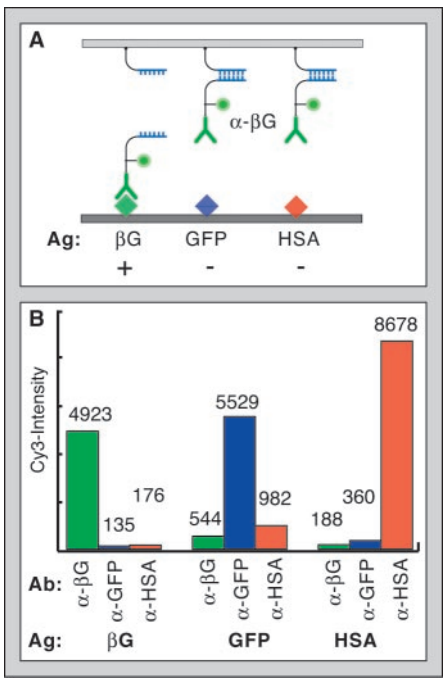

Fig. 3. Discrimination between specific and nonspecific antibody-antigen interactions with a DNA force sensor. (**A**) Three spots with different proteins [β-galactosidase (βG), green fluorescent protein (GFP), and human serum albumin (HSA)] on the bottom surface were probed with antibodies to β-galactosidase, which were connected to the top surface by way of DNA force sensors in unzipping conformation. Upon separation of the two surfaces, only β-galactosidase, which was probed with its specific antibody, was decorated with the fluorescently labeled antibody. (**B**) Fluorescence intensities (arbitrary units) on three different antigens (on the bottom surface) after each antigen was probed with three different antibodies, which were connected to the top surface by way of DNA zippers. Ab, antibody; Ag, antigen.

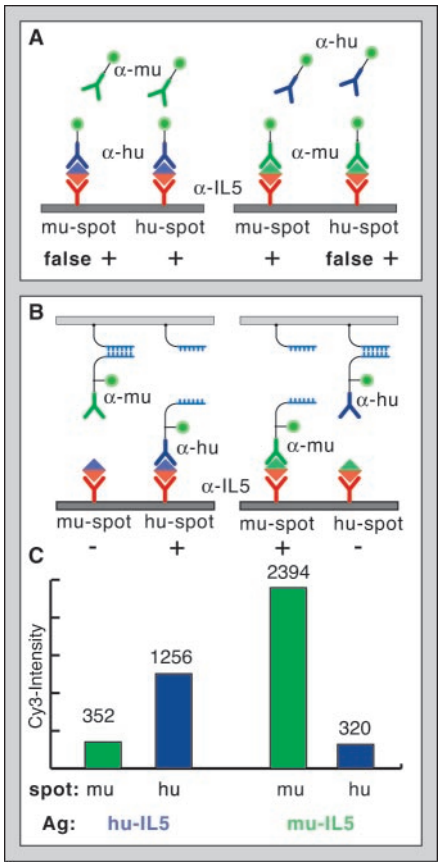

Fig. 4. Antibodies to IL-5, which bind both murine IL-5 and human IL-5, were used as capture antibodies in a sandwich immunoassay. The detection antibodies are specific for either murine IL-5 or human IL-5. (**A**) If both detection antibodies are applied simultaneously in buffer solution, as in a conventional protein array, the discrimination between murine (mu) and human (hu) antigens is not possible, because of the cross-reactivity of the capture antibody. (**B**) If the detection antibodies are coupled to the top surface by way of DNA force sensors, they can be applied locally. The second chip surface provides a second dimension for specific encoding, making it possible to define a murine and a human spot on the array and to discriminate between the two antigens. (**C**) Fluorescence intensities on the murine spots (green) and the human spots (blue) after incubation of human (left) and murine (right) antigen. Ag, antigen.

References and Notes

1. C. Bustamante, J. C. Macosko, G. J. Wuite, *Nature Rev. Mol. Cell Biol.* **1**, 130 (2000).
2. H. Clausen-Schaumann, M. Seitz, R. Krautbauer, H. E. Gaub, *Curr. Opin. Chem. Biol.* **4**, 524 (2000).

3. R. Merkel, *Phys. Rep.* **346**, 343 (2001).
4. R. Lavery, A. Lebrun, J.-F. Allemand, D. Bensimon, V. Croquette, *J. Phys. Cond. Matter* **14**, R383 (2002).
5. V. T. Moy, E.-L. Florin, H. E. Gaub, *Science* **266**, 257 (1994).
6. E.-L. Florin, V. T. Moy, H. E. Gaub, *Science* **264**, 415 (1994).
7. R. Merkel, P. Nassoy, A. Leung, K. Ritchie, E. Evans, *Nature* **397**, 50 (1999).
8. F. Schwesinger *et al.*, *Proc. Natl. Acad. Sci. U.S.A.* **97**, 9972 (2000).
9. S. B. Smith, Y. Cui, C. Bustamante, *Science* **271**, 795 (1996).
10. M. S. Kellermayer, S. B. Smith, H. L. Granzier, C. Bustamante, *Science* **276**, 1112 (1997).
11. M. Rief, M. Gautel, F. Oesterhelt, J. M. Fernandez, H. E. Gaub, *Science* **276**, 1109 (1997).
12. A. F. Oberhauser, P. E. Marszalek, H. P. Erickson, J. M. Fernandez, *Nature* **393**, 181 (1998).
13. M. Rief, H. Clausen-Schaumann, H. E. Gaub, *Nature Struct. Biol.* **6**, 346 (1999).
14. F. Oesterhelt *et al.*, *Science* **288**, 143 (2000).
15. T. Hugel *et al.*, *Science* **296**, 1103 (2002).
16. M. Grandbois, M. Beyer, M. Rief, H. Clausen-Schaumann, H. E. Gaub, *Science* **283**, 1727 (1999).
17. T. Strunz, K. Oroszlan, R. Schafer, H. J. Guntherodt, *Proc. Natl. Acad. Sci. U.S.A.* **96**, 11277 (1999).
18. R. Krautbauer, M. Rief, H. E. Gaub, *Nano Lett.* **3**, 493 (2003).
19. A. Janshoff, M. Neitzert, Y. Oberdorfer, H. Fuchs, *Angew. Chem. Int. Ed.* **39**, 3212 (2000).
20. A. D. Mehta, M. Rief, J. A. Spudich, D. A. Smith, R. M. Simmons, *Science* **283**, 1689 (1999).
21. F. Gittes, C. F. Schmidt, *Eur. Biophys. J.* **27**, 75 (1998).
22. M. B. Viani *et al.*, *J. Appl. Phys.* **86**, 2258 (1999).
23. In conventional force spectroscopy, molecular forces are measured as displacements against spring constants or trap slopes. Because the nature of intra- and intermolecular forces is fundamentally different from metal or silicon springs (or from optical or magnetic traps), all kinds of fluctuations or drifts, such as temperature and pH, will alter the measured signal. In the differential molecular format, each cancels out the effects of the other.
24. As long as the sample and reference complexes are similar, for example, consisting of two antibodies or two DNA oligomers (as in our case), the potential-energy landscape of the two complexes will be comparable. This means that the difference of the unbinding forces is approximately independent of the rate at which the force was built up. Consequently, this assay format is insensitive to variations of the spacer length or to separation velocity. Also, the force threshold of the common reference has to lie either within the force window defined by the molecular bonds under investigation, or close to one of these forces. The force distributions are broadened by thermal fluctuations on the order of k_BT/l , where k_B is Boltzmann's constant, T is temperature, and l is the characteristic width of the binding potential. Consequently, the window of possible reference forces is broadened by approximately the same amount (*49*, *50*).
25. This is true as long as the lateral density is kept below the fluorescence resonance energy transfer limit.
26. A. Kumar, N. L. Abbott, E. Kim, H. A. Biebuyck, G. M. Whitesides, *Acc. Chem. Res.* **28**, 219 (1995).
27. Y. Xia, G. M. Whitesides, *Annu. Rev. Mater. Sci.* **28**, 153 (1998).
28. A. Bernard, B. Michel, E. Delamarche, *Anal. Chem.* **73**, 8 (2001).
29. Different optical and chemical properties, as well as differences in coupling efficiencies to the two surfaces, are compensated in this way.
30. D. Pörschke, M. Eigen, *J. Mol. Biol.* **62**, 361 (1971).
31. C. Schildkraut, S. Lifson, *Biopolymers* **3**, 195 (1965).
32. P. Nollau, C. Wagener, *J. Int. Fed. Clin. Chem.* **9**, 162 (1997).
33. The discrimination between mismatch and perfect match could clearly be improved by decreasing the salt concentration or increasing the temperature and making use of both spontaneous and force-induced strand separation. However, in this study, we focused on forced unbinding events.
34. M. Chee *et al.*, *Science* **274**, 610 (1996).
35. R. J. Lipshutz, S. P. Fodor, T. R. Gingeras, D. J. Lockhart, *Nature Genet.* **21**, 20 (1999).
36. F. Naef, D. A. Lim, N. Patil, M. Magnasco, *Phys. Rev. E.* **65**, 040902 (2002).
37. U. Bockelmann, B. Essevaz-Roulet, F. Heslot, *Phys. Rev. Lett.* **79**, 4489 (1997).
38. B. Essevaz-Roulet, U. Bockelmann, F. Heslot, *Proc. Natl. Acad. Sci. U.S.A.* **94**, 11935 (1997).
39. The difference in the bond-rupture probabilities of the two chosen unbinding geometries is much larger than the difference in unbinding forces. Our assay measures the ratio of unbinding probabilities directly. Therefore, differences down to the order of the thermal force scale k_BT/l can be resolved.
40. R. P. Ekins, *J. Pharm. Biomed. Anal.* **7**, 155 (1989).
41. R. P. Ekins, F. Chu, *Trends Biotechnol.* **12**, 89 (1994).
42. P. Mitchell, *Nature Biotechnol.* **20**, 225 (2002).
43. L. G. Mendoza *et al.*, *Biotechniques* **27**, 778 (1999).
44. A. Abbott, *Nature* **415**, 112 (2002).
45. H. Petach, L. Glod, *Curr. Opin. Biotechnol.* **13**, 309 (2002).
46. C. Abrecht *et al.*, data not shown.
47. G. MacBeath, *Nature Genet.* **32** (suppl. 2), 526 (2002).
48. P. Cutler, *Proteomics* **3**, 3 (2003).
49. E. Evans, K. Ritchie, *Biophys. J.* **72**, 1541 (1997).
50. P. Hänggi, P. Talkner, M. Borkovec, *Rev. Mod. Phys.* **62**, 251 (1990).
51. We thank M. Rief for kindly providing the total internal reflection flourescence (TIRF) data showing single-molecule fluorescence, M. Benoit for technical support, F. Oesterhelt, C. Duschl, and D. Mendik for helpful discussions. Supported by the Nanobiotechnology and Proteomics program of the Bundesministerium für Bildung and Forschung (grants 13N8141 and O312821A) and the Bayerische Forschungsstiftung.

Supporting Online Material
www.sciencemag.org/cgi/content/full/301/5631/367/DC1
Materials and Methods
Fig. S1

19 March 2003; accepted 13 June 2003

Allosteric Activators of Glucokinase: Potential Role in Diabetes Therapy

Joseph Grimsby,[1] Ramakanth Sarabu,[1] Wendy L. Corbett,[1] Nancy-Ellen Haynes,[1] Fred T. Bizzarro,[1] John W. Coffey,[1] Kevin R. Guertin,[1] Darryl W. Hilliard,[1]* Robert F. Kester,[1] Paige E. Mahaney,[1]† Linda Marcus,[1] Lida Qi,[1] Cheryl L. Spence,[1] John Tengi,[1] Mark A. Magnuson,[2] Chang An Chu,[1] Mark T. Dvorozniak,[1] Franz M. Matschinsky,[3] Joseph F. Grippo[1]‡

Glucokinase (GK) plays a key role in whole-body glucose homeostasis by catalyzing the phosphorylation of glucose in cells that express this enzyme, such as pancreatic β cells and hepatocytes. We describe a class of antidiabetic agents that act as nonessential, mixed-type GK activators (GKAs) that increase the glucose affinity and maximum velocity (V_{max}) of GK. GKAs augment both hepatic glucose metabolism and glucose-induced insulin secretion from isolated rodent pancreatic islets, consistent with the expression and function of GK in both cell types. In several rodent models of type 2 diabetes mellitus, GKAs lowered blood glucose levels, improved the results of glucose tolerance tests, and increased hepatic glucose uptake. These findings may lead to the development of new drug therapies for diabetes.

Glucose homeostasis is lost in type 2 diabetes because of combined defects in both insulin secretion and insulin action (*1, 2*). The characterization of patients with abnormal glycemic control due to either gain- or loss-of-function mutations in GK has provided new insights into the pathogenesis of type 2 diabetes. Loss-of-function mutations in the gene encoding GK have been linked to maturity-onset diabetes of the young type 2 (MODY2), an autosomal dominant form of diabetes mellitus characterized by early onset and mild chronic fasting hyperglycemia (*3, 4*). MODY2 patients display impaired glucose responsiveness of β cells, decreased net accumulation of glycogen, and increased hepatic glucose production after meals (*5, 6*). The GK mutations found in MODY2 patients result in decreased activity of this enzyme as a result of reduction in its V_{max} and/or reduced affinity toward its substrates, glucose and adenosine triphosphate (ATP) (*7–11*). In contrast, gain-of-function GK mutations, which increase the catalytic activity of GK, cause persistent hyperinsulinemic hypoglycemia of infancy as a result of lowering the threshold

[1]Department of Metabolic Diseases, Hoffmann-La Roche Inc., Nutley, NJ 07110, USA. [2]Department of Molecular Physiology and Biophysics, Vanderbilt University, Nashville, TN 37232, USA. [3]Department of Biochemistry and Diabetes Center, University of Pennsylvania School of Medicine, Philadelphia, PA 19104, USA.

*Present address: Lilly Research Laboratories, Lilly Corporate Center, Indianapolis, IN 46285, USA.
†Present address: Chemical Sciences, Wyeth Research, 500 Arcola Road, Collegeville, PA 19426, USA.
‡To whom correspondence should be addressed. E-mail: joseph.grippo@roche.com

P2) Differential analysis of molecular rupture forces

Christian Albrecht, Hauke Clausen-Schaumann, Hermann E. Gaub

Journal of Physics, Condensed Matter, 2006, 18, p. S581-S599

INSTITUTE OF PHYSICS PUBLISHING JOURNAL OF PHYSICS: CONDENSED MATTER

J. Phys.: Condens. Matter **18** (2006) S581–S599 doi:10.1088/0953-8984/18/18/S06

Differential analysis of biomolecular rupture forces

Christian H Albrecht[1], **Hauke Clausen-Schaumann**[2] **and Hermann E Gaub**[1,3]

[1] Chair of Applied Physics, LMU-München, Amalienstrasse 54, D-80799 Munich, Germany
[2] Munich University for Applied Sciences, Lothstrasse 34, D-80335 Munich, Germany

E-mail: gaub@physik.uni-muenchen.de

Received 20 September 2005
Published 19 April 2006
Online at stacks.iop.org/JPhysCM/18/S581

Abstract

After a brief overview over the development of single molecule force spectroscopy and the basic concepts of bond dissociation under external force, we discuss the recently developed differential force assay, where a molecular bond serves as a microscopic force sensor. We introduce the basic concept of this novel biomolecular assay, discuss its requirements, capabilities and limitations, and present the latest advances in the design of the assay itself, as well as its appropriate hardware. The necessary data analysis procedures are introduced, and recent results showing the discrimination of single CC and GG mismatches within a 30 base pair DNA duplex are presented.

1. Introduction

The mechanical properties of biomolecules are closely related to their molecular structure and they are key parameters in understanding their biological function [1]. Consequently, techniques which allow the precise application and measurement of piconewton forces have provided new insights into the mechanisms governing biological phenomena at the molecular level. Today, in addition to material science, physical and physical chemistry aspects, research areas in force spectroscopy cover a broad range of biologically relevant topics, like molecular motors, protein folding, nucleic acid base pairing, or enzyme–substrate and receptor–ligand binding [2–5]. Moreover, especially intermolecular forces, like the ones involved in receptor–ligand binding and nucleic acid base pairing, also play a key role in a number of technological applications: from the detection of pathogens to the quantification of messenger RNA and proteins, the vast majority of assays in biomedical diagnostics rely on receptor–ligand binding or nucleic acid base pairing, with DNA and protein biochips being only two prominent examples. Furthermore, a large number of drugs and toxins interfere with protein–substrate binding or nucleic acid base pairing in one way or another.

[3] Author to whom any correspondence should be addressed.

0953-8984/06/180581+19$30.00

Unlike the more traditional methods of studying receptor–ligand binding and nucleic acid base pairing, such as micro-calorimetry, UV-absorption spectroscopy, or mass and refractive index sensitive techniques, like the quartz crystal microbalance or surface plasmon resonance spectroscopy, the dissociation of the molecular bonds by mechanical force allows not only for the quantification of binding enthalpies and reaction rate constants, but it can also provide detailed insights into binding potential landscapes and into the binding mechanisms.

1.1. Tools for measuring intermolecular forces

With the introduction of the surface force apparatus (SFA) by Tabor and Israelachvili, more than 30 years ago, the precise quantification of intermolecular and surface forces became possible for the first time [6]. In the SFA, two crossed cylindrical mica sheets are brought into close proximity with each other. The distance between the two sheets is determined by reflection interference contrast microscopy (RICM) and controlled by lever arms, while the force acting between the two sheets is measured with a mechanical spring. If the mica sheets are brought into contact, the contact area is usually of the order of several square microns, and the contact is established from the centre of the contact area towards the rim [7].

Electrostatic double layer forces, hydration and van der Waals forces, steric repulsion, friction and the forces governing molecular recognition have been studied with the surface force apparatus [8–10]. However, in the SFA, the contact area is still large, compared to molecular dimensions, and thus the intermolecular forces of many molecules act in concert. Because force is a directional parameter and binding forces in biological and chemical bonds depend on the direction of the applied force, as well as the distance along the reaction coordinate, it is not sufficient to just divide the measured force by the number of bonds probed. Therefore, in order to assess binding forces and binding potential landscapes of such bonds, a large number of molecules must be synchronized in time and space, and the number of bonds rupturing simultaneously must be precisely known. Although, with the SFA, this may in principle be accomplished, an alternative approach has been developed over the past 15 years: in single molecule force spectroscopy, one individual molecule is probed at a time and a synchronization of molecules is no longer necessary. This simplifies the experimental protocol considerably, and it makes the interpretation of the data straightforward, as incomplete synchronization and variable numbers of rupturing bonds cannot obscure the results. The most prominent techniques in single molecule force spectroscopy include optical and magnetic tweezers, glass micro-needles, the bio-membrane force probe (BFP), and most dominantly the atomic force microscopy (AFM)-based methods [7, 2]. In a typical experiment, a single molecule or molecular complex is anchored between a microscopic force sensor and an actuator which can be positioned with ångström precision. As the actuator is shortened, strain is built up within the molecule or between the partners of the molecular complex and the force sensor is displaced, by a small amount. Usually, for small displacements, the sensor displacement is proportional to the exerted force and can be detected for example by optical methods. In the case of the AFM, for example, the molecular complex is attached at one side to the substrate surface and at the other side to the sharp tip at the end of the cantilever spring. As the substrate or the cantilever is displaced by the piezo actuators, strain is built up, and the cantilever is deflected. The deflection of the cantilever is then detected via an optical lever and a position sensitive photodiode (cf also figure 1) [11].

1.2. The bond-rupture processes—thermally activated bond rupture versus quasi-static dissociation

In general, two different situations have to be considered, when molecular bonds, such as receptor–ligand bonds or nucleic acid base pairs, are ruptured apart by an external force. In

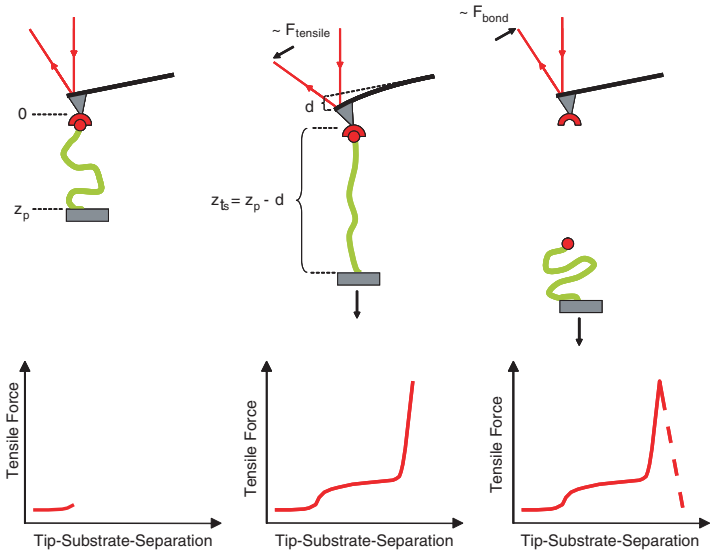

Figure 1. *AFM*. Schematic set-up of an AFM-based force spectroscopy experiment (top) and of the corresponding force trace (bottom) of a single-molecular bond attached to a polymer tether (a). Stretching of the polymer tether reveals details of the polymer elasticity: a tensile force F_{tensile} is exerted via the polymer and molecular bond to the AFM cantilever. The cantilever is displaced by a distance d, which is proportional to the exerted force, and the displacement is detected with an optical lever (b). When the tensile strength of the bond is exceeded, the molecular bond ruptures and the cantilever snaps back to its equilibrium position. The relaxation of the cantilever is proportional to the bond-rupture force F_{bond} (c). Reprinted with permission from [11]. Copyright, 2005, American Chemical Society, Washington, DC.

most cases, the binding partners are quickly separated from each other upon rupturing of the bond, so that the on-reaction is no longer possible. In this case, the on-rate is practically slowed down to zero. The bond rupture is irreversible and the whole rupture process occurs far from thermodynamic equilibrium. At the same time, the off-rate increases with increasing force, because the force effectively lowers the height of the energy barrier which must be overcome for spontaneous bond dissociation. According to a simple linear model proposed by Zhurkov and Bell [12, 13], and then elaborated by Evans *et al* [14–16], the energy barrier ΔG^* in the Arrhenius-rate function of the off-reaction is reduced by $f x_\beta$, where f is the applied force and x_β denotes the separation of the potential minimum and the dissociation barrier. The force dependent off-rate $k_{\text{off}}(f)$ then becomes

$$k_{\text{off}}(f) = \nu \exp\left(-\frac{\Delta G^* - f x_\beta}{k_B T}\right), \tag{1}$$

where ν is the force independent frequency factor, which depends on the curvature of the binding potential at its minimum, $\Delta G^* - f x_\beta$ is the effective height of the dissociation energy barrier under force, k_B is the Boltzmann constant, and T the temperature. Because $1/\nu$ is usually much smaller than the typical timescale of a force experiment, the dissociation barrier is probed many times during the experiment. Consequently, the bond dissociation under force is a thermally activated process and the observed rupture force depends on the timescale of the experiment. Fast loading of the bond will lead to a higher bond rupture force than slow loading, because shorter bond lifetimes require higher forces, as can be seen from equation (1). Using $k_{\text{off}}(f)$ from equation (1), bond rupture probability distributions and unbinding forces can be

derived in a straightforward manner [14, 16]. For a constant force loading rate $\mathrm{d}f/\mathrm{d}t$ the most probable bond rupture force f^*—i.e. the maximum of the rupture probability distribution—depends logarithmically on the force loading rate, as long as the binding potential has a single dissociation barrier. In a semilogarithmic representation of bond rupture force versus the logarithm of the force loading rate, the width of the potential, as given by x_b, can be derived from the slope of the graph, and its intersect with the $\ln(\mathrm{d}f/\mathrm{d}t)$ axis gives the off-rate at zero force. For multi-barrier potentials, the semilogarithmic representation of f^* and $\mathrm{d}f/\mathrm{d}t$ exhibits several distinct regions with different slopes, each representing the distance to the next internal separation barrier [17].

On the other hand, if a large number of consecutive bonds has to rupture in series, before the binding partners are effectively separated, both off-reaction and on-reaction can occur during the time course of the experiment. As long as the reaction rates are fast, compared to the experimental timescale, the rupture process is a fully reversible equilibrium process. In such a case the observed rupture force does not depend on the timescale of the experiment and therefore is independent of the force loading rate. A prominent example is the unzipping of long DNA duplexes which are attached to soft springs. Here on-rates and off-rates are of the order of several kilo-base-pairs per second, which is fast compared to a typical force experiment [18–22].

1.3. New tools for measuring intermolecular forces—small force sensors and symmetric designs

Today, with state of the art instrumentation, within a given bandwidth, the force resolution, i.e. the smallest detectable force f_min, is limited only by Brownian motion of the force sensor, which, according to the fluctuation-dissipation theorem, depends on temperature and on the viscous damping of the sensor:

$$f_\mathrm{min} = \sqrt{4k_\mathrm{B}TRB}, \tag{2}$$

where k_B is the Boltzmann constant, T is the temperature, R is the coefficient of viscous damping and B is the bandwidth [23, 24]. Smaller sensors experience less viscous damping, and within the desired bandwidth, the smallest detectable force f_min is therefore a function of temperature and of the size of the sensor. In recent years, several attempts have been made to reduce the size of the cantilever spring in AFM-based set-ups. Viani *et al* have demonstrated that the thermal noise of an AFM cantilever can be reduced by a factor of five, if the size of the cantilever is reduced by one order of magnitude [24]. However, as the size of the cantilever is reduced, it is crucial that the lever maintains a spring constant of the order of a few millinewtons per metre ($\mathrm{mN\ m^{-1}}$), because otherwise detector and other instrumental noise sources may start to play a role and the assumption that the force resolution is only limited by Brownian motion of the cantilever no longer holds true. As further miniaturization of AFM cantilevers remains technologically challenging, alternative routes have to be explored, to further improve the force resolution. With bead-based techniques, like optical and magnetic tweezers, the miniaturization of the sensors, i.e. the trapped beads, seems somewhat simpler; however, here miniaturization goes at the expense of the accessible force range, as with small beads only small forces may be exerted, while receptor–ligand bond rupture forces can be of the order of a few hundred piconewtons (pN).

A conceptually different and very simple approach to reduce the size of the force sensor to a few nanometres is the use of a single molecular bond as a force standard, to which the sample bond is directly compared. In this case, the sample bond must be linked to the force standard, also referred to as the reference bond, and the external force must be applied to the sample

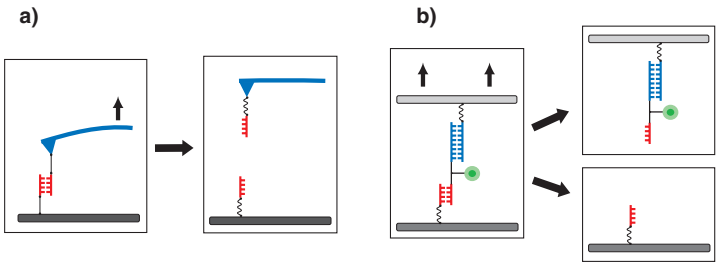

Figure 2. *AFM and DFA*. Comparison of rupture force measurements by atomic force microscopy (a) and differential force assay (b). Upon separation of the two surfaces the polymeric anchors are stretched and the force acting along the molecular complex is slowly built up. The weaker of the two molecular bonds will rupture first and as a result the label will end up on either side.

and the reference bond in series. One experimental realization of such a set-up is depicted in figure 2. Figure 2(a) shows a typical AFM set-up, where a DNA duplex is attached to an AFM tip and the substrate surface. Here the tensile force which is needed to rupture the DNA duplex is detected via the AFM cantilever spring. Figure 2(b) shows a set-up where a molecular complex consisting of a sample bond (red) and a reference DNA duplex (blue) is connected to two adjacent surfaces via polymeric anchors. As the two surfaces are separated, the force acting on the bonds in series gradually builds up until eventually the weaker bond fails. A fluorescent label, which is positioned between the two possible rupture sites, is used to identify which one of the two molecular bonds actually has ruptured. This approach has been introduced in a recent paper by Albrecht *et al* [25], where single base mutations in DNA have been detected based on bond rupture forces. A similar set-up, where the external force is applied and also monitored through an optical trap and again fluorescence is used to determine which bond ruptures, has recently been described by Lang *et al* [26].

In addition to reducing the size of the sensor, the scheme described here also increases the symmetry in single molecule force experiments. In conventional set-ups, intermolecular forces are determined via the deformation or deflection of micrometre sized springs, while here, intermolecular forces are directly compared to each other in a differential measurement format. This is analogous to weighing macroscopic objects with either scales or mechanical springs, where it is immediately evident that even with a crude scale balance small weight differences can be accurately detected, because the same physical parameters are directly compared, whereas, when a spring is used, a much more sophisticated device is required. In fact, it is a fundamental principle that small differences or small changes in a physical parameter can be most accurately determined if the difference is directly measured.

Furthermore, as has been discussed above, the forced separation of molecular bonds is a thermally activated, statistical process. Therefore a large number of rupture experiments must be carried out for each type of molecular bond. With a set-up like the one depicted in figure 2(b), it is possible to probe many molecules at the same time, because large numbers of molecules can be easily assembled between the two surfaces and probed simultaneously. Here it is important to note that the intermolecular forces are still characterized on the single molecule level, as each sample bond is individually probed by its own reference bond. Neither the macroscopic forces acting between the two surfaces nor their separation need to be determined, and the synchronization and quantification of molecules can therefore be avoided. Finally, this set-up is also capable of multiplexing, as it is compatible with chip-based assay formats, as are widely used in bio-analytics and biomedical diagnostics [27–29]. For this purpose different molecular complexes may be assembled in different spots on the substrate surface and then be connected

to the second (top) surface. Instead of measuring equilibrium binding constants, as is done with conventional biochips, the mechanical strength of the molecular bonds that have formed on the chip can be measured. This has several potential advantages over conventional chip-based assays. Assay times can be reduced, because thermodynamic equilibrium is not required, and low off-rates and rebinding do not require time-consuming washing steps. By selecting appropriate reference molecules, stringent assay conditions can be achieved locally for all spots on a chip, even if the different analyte molecules have different binding constants. And finally, in multiplexed sandwich immuno-assays, the specificity of the assay can be drastically increased, because two chip surfaces, rather than one, can be used for antigen specific encoding, as has been shown by Blank *et al* [30].

Here we give an overview over the present state of the development of the differential force assay, its capabilities and limitations. We describe recent advances, which include a motor and piezo controlled contact device, combined with a reflection interference contrast microscope for accurate distance and velocity control, an improved design of the micro-structured surfaces and surface chemistry, and we compare the assay and assay results to data obtained by other methods well as to theoretical modelling.

2. Methods

2.1. A detailed description of the differential force assay

Let us now take a more detailed look at the differential force assay and its requirements, capabilities and limitations. For convenience the differential force assay will be abbreviated as DFA in the following parts of this paper. For the complex containing the sample and reference bonds, as well as the fluorescence label, the term differential rupture complex or DRC will be used. Similar to the field of biochip technologies, the disposables of the DFA consist of chip surfaces containing immobilized biomolecules, and a fluorescence scanner serves as the readout instrument. However, in addition to more conventional biochip formats, a device for contacting and pulling apart the two chip surfaces is required. Like other chip formats, the DFA allows for the parallel measurement of multiple samples at once. In its present state 16 sample spots are deposited on an area of 1 cm $\times$ 1 cm, in a 4 $\times$ 4 array. Nevertheless, further parallelization through miniaturization is possible with more sophisticated micro-spotting devices.

A typical DFA experiment is depicted in figure 3. The assembly of the DRC starts with the covalent immobilization of the amino-modified DNA-oligomer (oligo) onto the bottom surface (the glass slide). The fluorescently labelled oligo is then hybridized to the amino-modified oligo. In the next step a biotin-labelled oligo is hybridized to the fluorescently labelled oligo, thereby completing the *DRC*. This initial situation is depicted in figure 3 on the left-hand side. Now, the upper chip surface (the silicone stamp), which is coated with a streptavidin layer is lowered, until the biotin-labelled oligo can bind to the streptavidin by molecular recognition and form a high affinity bond (middle). As the silicone stamp is withdrawn again from the glass slide, a loading force gradually builds up within the DRCs, until one of the two DNA duplexes within each DRC ruptures (right-hand side). As a result, the fluorescence label within each DRC ends up alongside the intact bond. The fluorescence intensities on both the silicone stamp and the glass slide are then determined using a fluorescence scanner. Note that during the chip separation, each DRC is loaded and probed individually so that the overall force acting between the chip surfaces does not affect the outcome of the assay.

This differential force measurement is a unique feature of the DFA, which also shares a number of features with other methods like AFM, SFA, as well as micro-contact printing (μCP), as will be pointed out in the following sections.

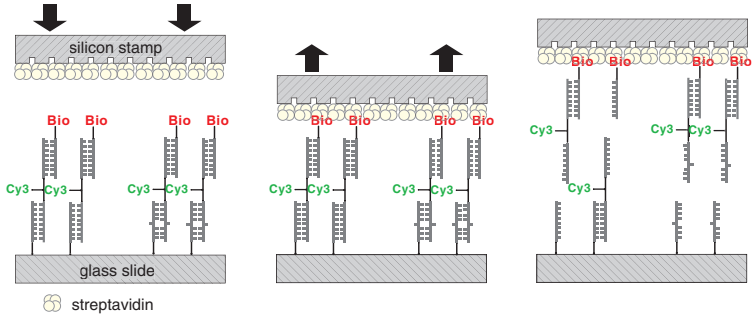

Figure 3. *DFA process*. Schematic diagrams of the differential force assay with oligo nucleotides. Two spots each containing two identical molecular rupture complexes (DRC) are to be compared. The DRCs on the left spot are symmetrical. The lower and the upper duplex are equal in length. The DRCs on the right spot have a lower duplex, which contains a single base pair mismatch. Left: the stamp is approaching the slide. Middle: the stamp is in contact with the slide. The DRCs are coupled to the streptavidin layer of the stamp via their biotinylated oligos. As the stamp is retracted, force builds up in the DRCs. Right: the stamp is removed from the slide. All DRCs are broken due to the force they have experienced. Because of the symmetrical structure of the DRCs on the left spot there is a 50–50 distribution of the Cy3-label between stamp and slide. On the right spot both DRCs are ruptured at the lower duplex, which is weaker than the upper duplex. Both Cy3-labels end up on the stamp side.

(a)

```
5' Bio-ttttttttttCTGCAGGAATTCGATATCAA   ←  biotin oligo
                 ||||||||||||||||||||
3'     Cy3-ttttt GACGTCCTTAAGCTATAGTT tttttttttttttttttt TTGATATCGAATTCCTGCAG  ←  cy3 oligo
                                                         ||||||||||||||||||||
5'                                  amino oligo  →  AACTATAGCTTAAGGACGTCttttttttttt-NH2
```

(b)

```
5'                CTGCAGGAATTCGATATCAAttttttttttt-Bio  ←  biotin oligo
                  ||||||||||||||||||||
3'     Cy3-ttttt GACGTCCTTAAGCTATAGTT tttttttttttttttttt TTGATATCGAATTCCTGCAG  ←  cy3 oligo
                                                         ||||||||||||||||||||
5'                       amino oligo  → NH2-ttttttttttt AACTATAGCTTAAGGACGTC
```

Figure 4. (a) *DRC sh-sh*. Differential rupture complex in two-fold shear geometry. Double-stranded DNA, the amino group (NH_2) for immobilization on the slide, the Cy3-fluorophore (Cy3) and the biotin residue (Bio) for the connection to the stamp are shown in bold letters. The polyT spacers are shown in regular letters. (b) *DRC zp-zp*. Differential rupture complex in two-fold zipper geometry (see (a) for details).

2.1.1. Molecules. As described above, the DRC consists of a serial assembly of three DNA oligonucleotides. A typical example is depicted in figure 4(a).

For better readability, here the DRC is drawn in horizontal orientation. Double-stranded DNA is represented by capital letters, single-stranded spacers in small letters. (The spacer sequences do not contribute to the actual base pairing. They have been introduced to separate the base pairing regions of the oligos from the slide and the stamp surface, and to allow better overall flexibility of the DRCs.) With respect to utmost symmetry, both double strands are equal in length and base composition (G–C and A–T content) and are even reverse to each other in terms of sequence. The upper oligo (to the left) is labelled with the biotin anchor, the middle oligo with the Cy3-fluorophore and the bottom oligo (right) with an amino linker for covalent immobilization. Notice that both double strands are probed in a shearing geometry, where the force builds up parallel to the double helix. A zipper geometry, where the force builds up perpendicular to the double helix, and the individual base pairs are separated in a sequential fashion, is depicted in figure 4(b).

The DRCs used in the shear–shear experiments described below, contain 30 base pair (bp) duplexes in shear mode and 60–62 nucleotides long single-stranded spacers. In completely elongated conformation, all single and double strands add up to about 60 nm in length. As estimated from a dilution series, about 10 fmol DRCs are immobilized per 1 mm^2 of the slide. This equals 10 DRCs on 100 nm $\times$ 100 nm.

It is evident that the coverage of the slide with DRCs is rather dispersed. However, a higher immobilization density of oligos might result in molecular crowding when the biotin-labelled oligos are connected to the stamp, which might interfere with the single molecule character of the experiment.

A general limitation of the differential force assay is that it has to compete with the natural (zero force) off-rate of the nucleic acid duplexes in the DRC. In case of very short DNA duplexes, low ionic strength buffers or high temperature, this natural off-rate may result in dissociation of the duplexes before the DRCs can be probed with the stamp. However, for double strands between 20 and 30 bp in 150 mM NaCl at room temperature, the spontaneous off-rates are of the order of hours to days, so these parameters are not critical.

2.1.2. Surface chemistry. A specific oriented attachment of the molecules is crucial for the outcome of the DFA, as illustrated by the shear-zip experiment described below. The altered binding geometry (5′ instead of 3′ terminus) from shear to zipper mode shifts the bond rupture force of the duplex tremendously.

For immobilization of DNA oligos on glass slides a wide variety of commercial solutions have been developed. However, the widespread ionic adsorption of the negatively charged DNA backbone to positively charged amino-functionalized surfaces cannot be used for the DFA, because this results in a rather ill-defined binding geometry of the DNA. Easily available epoxysilane slides also have limitations, because epoxy groups react with a broad range of nucleophilic residues, including intrinsic amino moieties within the nucleotides A, C and G. In our hands amino-labelled oligos attached to aldehyde slides work very well. This chemistry is reported to yield highly specific binding to the terminal amino linker. Furthermore all single-stranded spacer nucleotides are amino-free thymidines and hence do not bind to the aldehyde slide. A typical array of 16 spots on 1 cm^2 before contact with the stamp is shown in figure 6 left bottom[4].

In contrast to the commercially available slides, the surface chemistry on the silicone stamp is home-made. The silicone elastomer is activated in HCl. In experiment 2 the stamp is coated with aminosilane and grafted with reactive biotin-polyethyleneglycol (PEG) before streptavidin is bound to the surface (cf supporting online material of reference [25] for details). Alternatively, epoxysilane can be used in combination with amino-PEG-biotin. In the latter case the PEG (Rapp Polymere, Goettingen; 3000 Da) is melted at 80 °C and incubated on the stamp for 12 h, before it is washed with boiling water thoroughly (experiment 1).

2.1.3. Contact. At present, the contact area of the DFA is in the range of 1 mm^2 per spot. This could be reduced to a few μm^2 per spot, by further miniaturization. Still, the relatively large contact area is a common feature that the DFA shares with SFA. Considering the high sophistication required to bring two atomically smooth mica cylinders into contact in the SFA, it is evident that for the DFA, with multiple sample spots on each chip, a different strategy has

[4] A simple method for spotting such arrays accurately has been established just by using the same stamps as described below as a printing tool. Each pad of the stamp is loaded with a drop of the amino-modified oligo solution in upside-down orientation. Then the stamp is turned around and the pads are brought into close proximity to the slide until the drops come into contact with the surface. Due to wetting forces and gravity about 3/4 of the drop is transferred to the slide in a contact-free manner.

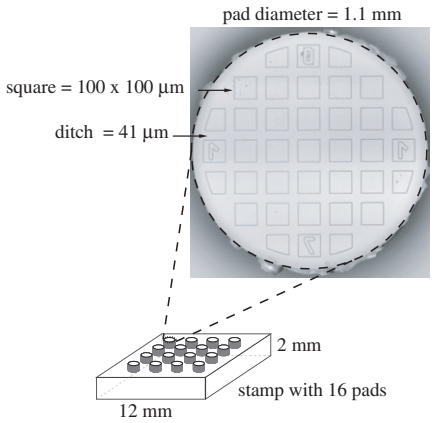

Figure 5. *Stamp structure*. A sketch of the silicone elastomer stamp is shown. The blown-up image shows the substructure of a single pad of 1.1 mm in diameter.

to be pursued to establish contact between the two surfaces. Rather than trying to perfectly level and align the two surfaces, we used one soft surface, which can conform to the other rigid surface. As soft surface, we have chosen a micro-structured silicone stamp such as is widely and successfully used for micro-contact printing, which was introduced by Whitesides [31] and co-workers. Such silicone elastomers can compensate for surface corrugations even on relatively rough surfaces, like standard microscope slides. Furthermore, they can be produced easily, by casting silicone in micro-structured moulds.

Because the stamp has to comply with the functions of uniform, conformal contact and fast drainage of buffer over an area of 1 cm^2, the geometry of the stamp is crucial for the whole experiment. The minimum requirement is a microstructure of elevated zones which come into contact with the slide, and are separated by a grid of some μm deepness. Suitable aspect ratios in terms of mechanical stability have been investigated by Delamarche *et al* for μCP [32]. The microstructures on our stamp are 100 μm $\times$ 100 μm squares with an elevation of 5 μm. The grid between the squares is about 41 μm wide, which results in a ratio of elevated to recessed surface area of approximately 1:1.[5]

As depicted in figure 5 (photograph), the microstructure is located on pads of 1.1 mm diameter and 1 mm height, which are connected to a 2 mm thick base of silicone. The 16 elevated pads shown in figure 6 (top left) are opposite to the 16 sample spots on the slide.

The pad columns increase the overall aspect ratio of the stamp and thereby improve its elastic properties. The continuous 1 mm thick stamp which was used previously in comparison has had a 8.6 times higher spring constant. The reduced contact surface, which is now restricted just to the area of the pads, and the softening in the z-direction enhance the levelling of the stamp considerably. Figure 6 (top) shows all 16 pads in contact with the slide. The image was recorded using reflection interference contrast microscopy.

[5] The moulds for the stamps are manufactured using an SOI wafer with a 5 μm thick silicon layer on top of an oxide layer. The microstructure is etched into the wafer by standard procedures. On top of the SOI wafer a Pyrex glass wafer is fixed by anodic bonding. The Pyrex wafer was structured with holes of the pad diameter, by means of ultrasonic drilling, before bonding it to the SIO wafer. Finally, the bonded SOI-Pyrex-wafer was coated with fluorosilane, in order to prevent the silicone from sticking to the mould. The bonded moulds were purchased from HSG Imit, Villingen-Schwenningen, Germany.

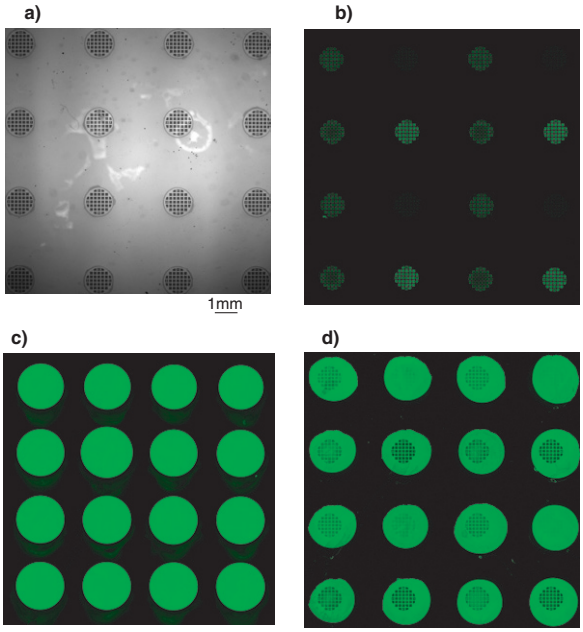

Figure 6. *Elastomer stamp and DNA-array on slide*. Reflection interference contrast micrograph of the stamp (a). Fluorescence micrographs of the stamp after contact (b), of a 16 spot DNA array on 1 cm^2 before contact (c) and of another array after contact (d).

2.1.4. Contact device. The contact device is similar to a micro-contact printing tool for soft lithography developed by the Physical Chemistry group, at the NMI Reutlingen [33]. The stamp and slide are brought into contact by means of a piezo stage (figure 7). The contact process is monitored from the bottom by reflection interference contrast microscopy (RICM). Once the gap between the silicone and the glass is of the order of the wavelength of the incident light, interference patterns are observed, until contact results in total extinction.

Figure 6 (top left) shows an RICM image of the entire stamp in contact with glass in air. In liquid, the contrast is reduced significantly, because the difference in refractive index between the stamp and the surrounding media drops from $\Delta n_{\mathrm{PDMS-air}} = 0.45$ in air to $\Delta n_{\mathrm{PDMS-water}} = 0.11$ in water. To get an overview over the whole stamp, we have used the relatively low magnification of a 1.25× objective in combination with a 16-bit CCD camera (Zeiss Axiocam). The low contrast, which is hardly resolved by eye, was enhanced by the Axiocam image processing software, using the white reference function. Adhesion of the PDMS is employed to mount the stamp onto its support.

Then stamp and slide were levelled using a tilt stage guided by the RICM image. It takes about 10 μm in z-direction from the first contact at one pad of the stamp to full contact of all pads. The corresponding contact pressure can be estimated from the Young's modulus of Sylgard184 [34] to be 17 mN mm^{-2}. If one considers that the quaternary structure of proteins remains intact up to pressures of 1 kbar, we can assume that streptavidin remains intact since we are approximately four orders of magnitude lower in pressure.

2.1.5. Coupling. As depicted in figure 3, the DRC is built up by hybridization on the slide and is subsequently connected to the streptavidin-coated stamp by means of the biotin label. The efficiency of bond formation is between 50% and 90%. Apart from several other parameters,

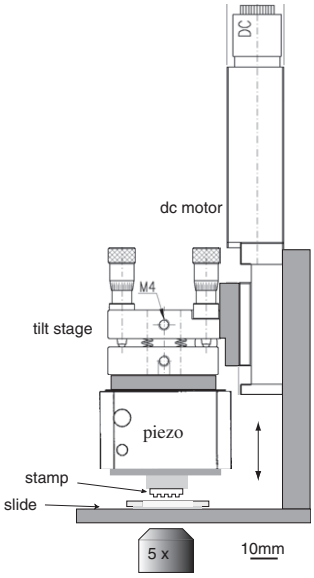

Figure 7. *Contact device*. The slide with the DNA array is located between the contact table and a trough which contains buffer solution. The stamp is mounted upside down on a glass support by adhesion. The stamp can be moved in the z-direction by the piezo stage, as well as the dc motor. Adjustment in terms of planarity between stamp and slide are accomplished by the tilt stage.

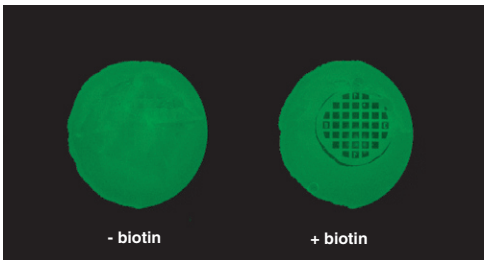

Figure 8. *Specific coupling*. Specificity of the coupling step: fluorescence micrographs of two spots on the slide after contact and removal of the stamp. The oligos on the left spot carry no biotin. The right spot is biotinylated. No Cy3–oligo was removed from the left spot, which demonstrates that the removal of Cy3–oligo from the right spot is due to specific interaction between biotin and streptavidin.

like biotin and streptavidin density and spacer length, variations in contact pressure in particular account for the broad distribution of coupling efficiencies. A sufficiently uniform contact pressure over all 16 pads hence is essential for reproducible experiments.

Once formed, the biotin–streptavidin bond is practically irreversible due to its very low off-rate. In order to demonstrate the specificity of this coupling step, the following control experiment was carried out. In figure 8 the DRC was *not* labelled with biotin on the left spot, while the right spot contained a biotinylated DRC. Consequently, on the left spot no DNA was removed from the glass slide, while on the right spot fluorescently labelled DNA was removed from the contact areas (dark squares). This demonstrates that the transfer of oligos to the stamp surface is indeed highly specific.

The coupling efficiency can be determined by labelling the free biotin residues, which have been left on the glass slide, after separation of the two surfaces, with a soluble streptavidin,

carrying a second fluorescent label. To avoid crosstalk between the two fluorescent labels, their emission and absorption spectra should be well separated. In our case we used Cy3 as a reporter within the DRC and AlexaFluor-647 as a label for the free streptavidin. Labelling with streptavidin-AF647 is done after the first scan in the Cy3-channel. Scans in the Cy3-channel are displayed in green, and scans in the AF647-channel in red (see figures 9 and 10).

2.1.6. Surface forces. Just like in AFM-based force spectroscopy, nonspecific surface interactions have to be avoided in the differential force assay. Therefore, like in AFM-based force spectroscopy, spacer molecules, here in the form of additional single strands on both ends of the DRC, are used to move the DNA duplexes away from the surfaces and separate the two surfaces from each other. Furthermore, in the set-up discussed here, attractive electrostatic forces can be neglected, because the slide, which contains carboxyl groups, and the streptavidin layer are both negatively charged at the working pH of 7.2 [7]. Also, at a NaCl concentration of 150 mM, electrostatic interactions between the surfaces are effectively screened, as the Debye length is only 0.78 nm [9] under these conditions.

However, van der Waals forces, which are not much affected by ionic strength and pH, may still contribute to the adsorption–desorption behaviour of the stamp and slide. Nevertheless, unlike in AFM and SFA experiments, in the DFA nonspecific surface to surface interactions do not interfere with the rupture forces of the individual DRCs, because the forces acting between the two chip surfaces are not measured or quantified in the experiment. Only the forces acting on the DRCs contribute to the observed results, and because the DRCs contain the sensor that actually measures the force—i.e. the reference bond in the DRC—nonspecific surface to surface forces can be ignored with this set-up.

2.1.7. Separation of stamp and slide. The pulling velocity is another important parameter for the DFA. The piezo set-up in figure 7 allows for separation velocities between nm s^{-1} and mm s^{-1}. Pulling velocities with the AFM usually do not exceed 10 μm s^{-1}, as at higher velocities deflection of the cantilever caused by hydrodynamic forces increasingly interferes with the measurement. Although hydrodynamic forces should disturb the molecular force sensors used in the DFA much less than the microscopic sensors, which are employed by other techniques, such as AFM, fluid shear stress may lead to a loss of oligonucleotides, when the silicone stamp is disrupted from the slide very rapidly. We have therefore used low pulling velocities (5 nm s^{-1} to about 1 μm s^{-1}) with the DFA so far.

As described in the introduction, the rupture force of a molecular complex with a single dissociation barrier depends logarithmically on the force loading rate. Because the slope of the f^* versus $\ln(\mathrm{d}f/\mathrm{d}t)$ curve is inversely proportional to the bond width x_b, i.e. the distance between the potential minimum and the dissociation barrier, this effect has to be considered in particular for cases where the two bonds, which are compared, have different bond widths, as is the case for DNA in shear and in zipping geometries. If the bond widths are comparable, like in the case of two 30 bp duplexes in shear geometry one containing a single mismatch and one perfect match, both bonds will be affected by the force loading rate in almost the same way. However, since the force loading rate depends not only on the pulling velocity, but also on the elasticity of the sample molecules and their molecular spacers, as well as the surface elasticity, the actual force loading rate at the DRC cannot be determined directly in our present set-up. Nevertheless, as the elasticity of the system remains constant for a certain kind of experiment, the loading rate can be assumed to be constant, as long as the pulling velocity is kept constant. The influence of the loading rate on the relative rupture probability will be discussed in more detail below.

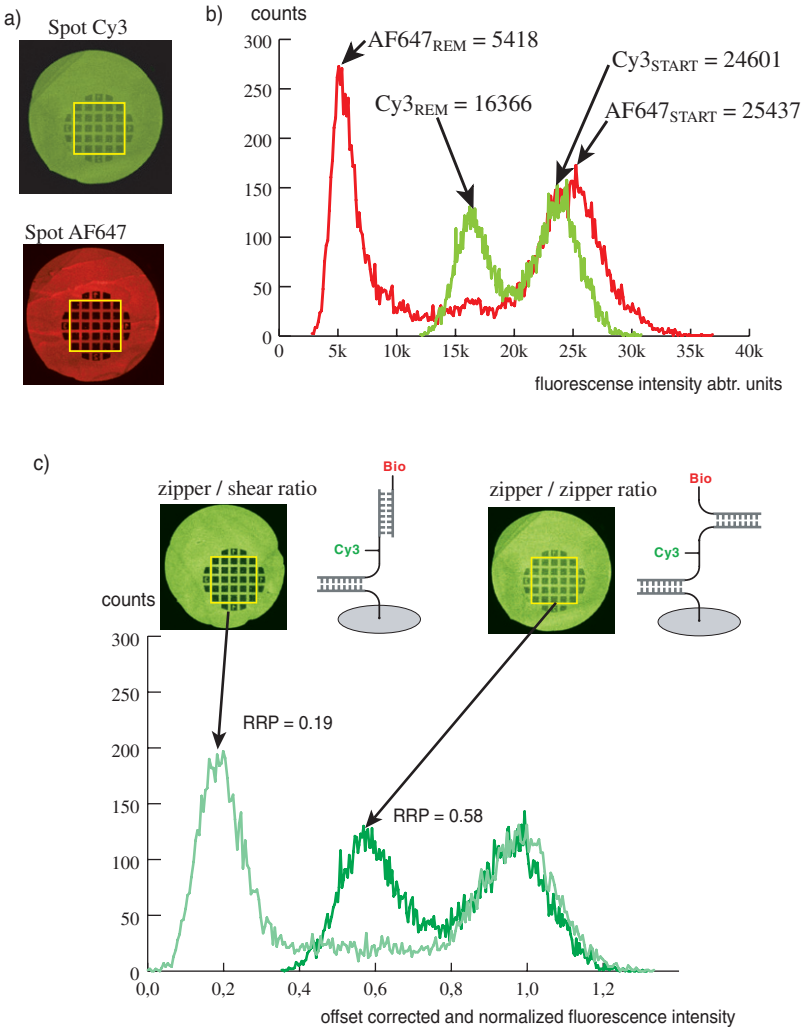

Figure 9. An experiment is presented, in which on one spot a 30 bp duplex in shear geometry is compared to a 30 bp duplex in zipper geometry and on another spot a 30 bp duplex in zipper geometry is compared to a 30 bp zipper geometry. (a) Two micrographs of the zipper/zipper spot after separation of stamp and slide are shown. The upper micrograph shows the Cy3 fluorescence intensity and the lower one the AF647 fluorescence intensity, after streptavidin labelled to AF647 was bound to the free biotins (the molecular scheme is shown in (c) on the right). (b) The histogram shows two fluorescence intensity curves corresponding to the area inside the yellow regions of interest in the spots in (a). On both curves arrows indicate the START-value for Cy3 and AF647 which corresponds to the grid in (a). The REM-values for Cy3 and AF647, corresponding to the dark squares in (a) are indicated as well. (c) The molecular structure of the shear/zipper and the zipper/zipper spots are shown schematically. The micrographs show Cy3 intensities, corrected for the offset due to molecules which did not couple, and normalized with respect to the offset corrected $Cy3_{START}$-values. The histogram again displays the regions of interest of both spots. In each curve arrows indicate the vertex of the first peak. This value corresponds to the relative rupture probability (RRP) of the lower DNA duplex. The pulling velocity of the base of the stamp was 660 nm s^{-1}.

2.1.8. Read-out. Fluorescence intensities were determined with a Tecan LS laser scanner at a spatial resolution of 6 μm. Thanks to its autofocus system, this scanner is well suited even

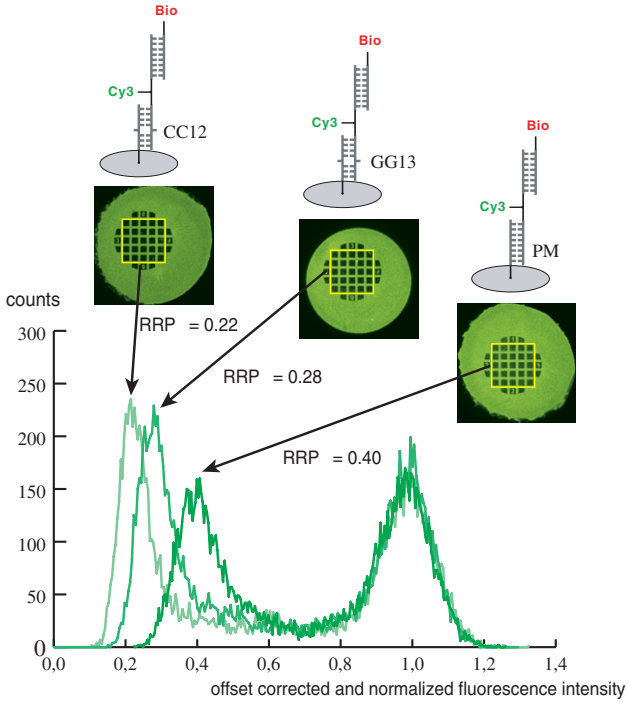

Figure 10. The molecular structures of an experiment are shown, in which the upper duplex is a 30 bp duplex in shear geometry in all three spots. The lower duplex is a 30 bp shear geometry containing a CC mismatch at position 12 on the left spot, a GG mismatch on position 13 on the middle spot and a perfect match on the right spot. The micrographs show Cy3 fluorescence intensities, corrected for the offset of non-coupled molecules and normalized to offset corrected $Cy3_{START}$-values. The histogram displays the region of interest of the three spots. In each curve arrows indicate the vertex of the first peak. This value corresponds to the relative rupture probability (RRP) of the lower DNA duplex. The pulling velocity of the base of the stamp was 5 nm s^{-1}.

for the measurement of complex surfaces, like our micro-structured silicone stamps. Cy3 was scanned at 532 nm and AF647 at 633 nm excitation wavelength.

3. Experimental results and discussion

A good example to illustrate the difference between force measurements and the measurements of reaction rate constants is depicted in figure 9. Here, two 30 bp DNA duplexes with identical sequences are compared to each other (cf figure 9(c) for a schematic drawing of the experimental set-up). In one case (left) the force is applied parallel to the helix axis, in shearing geometry; in the other case (right), the force is applied perpendicular to the helix axis, and the two strands of the double helix are separated like a zipper. In the experiment depicted in figure 9, for both geometries, the force is applied via a 30 bp DNA duplex in zipper geometry, which is attached to the slide (bottom surface) and which again contains the same base composition.

Figure 9(a) shows two fluorescence micrographs of the slide, of a typical spot where the DRCs (cf section 2.1) consist of two 30 bp DNA zippers (zip/zip). The green image (top) shows the Cy3 fluorescence intensity, after the two chip surfaces have been separated. The dark squares correspond to areas where the streptavidin-functionalized PDMS stamp has made

contact with the slide and where some of the Cy3-labelled oligos have been transferred to the stamp after the two surfaces have been separated. The fluorescence intensity of the dark squares ($Cy3_{REM}$) therefore represents DRCs, where the duplex at the bottom has remained intact after separation of the two chip surfaces. The grid pattern between the squares, on the other hand, corresponds to the micro-channels on the stamp surface. Here, as well as in the surrounding region, the stamp has not made contact with the slide, and consequently no Cy3-labelled oligos have been transferred to the stamp during the experiment. Consequently, the fluorescence intensity of the grid pattern reflects the initial DRC concentration on the slide. A histogram of fluorescence intensities (green trace in figure 9(b)) clearly shows the two corresponding peaks at fluorescence intensities of 16.4k and 24.6k.

The normalized $Cy3_{REM}$ value, i.e. the ratio of $Cy3_{REM}$ and $Cy3_{START}$, which in this case is 0.67, should therefore correlate to the relative bond rupture probability of the DNA duplex at the top of the DRC, i.e. the probability that the duplex at the top ruptures before the bottom one does. However, as already pointed out in section 2.1.5, not all of the biotin-labelled DRCs actually couple to the streptavidin-coated stamp and experience an external force, when the slide and stamp are separated. To quantify the fraction of molecules which did not couple to the stamp during the experiment, we incubated the slide with AlexaFluor-647 (AF647)-labelled streptavidin, after the slide and stamp had been separated. The red image of figure 9(a) (bottom) shows the corresponding AF647 fluorescence intensity. The remaining AF647 fluorescence intensity in the dark squares should be proportional to the number of DRCs which have not coupled to the functionalized stamp during the experiment, while the AF647 intensity on the grid should be proportional to the total number of biotin-labelled DRCs on the slide. Again, the two corresponding peaks can be clearly identified in the fluorescence intensity histogram (red trace in figure 9(c)). The ratio of AF647 intensities on squares and grid—in this case 0.21—should be equal to the fraction of DRCs which did not couple to stamp. We can use this result to correct our data and exclude those DRCs which did not couple properly to the stamp. If, for example, 21% of the DRCs did not couple to the stamp and thus did not take part in the force experiment, we simply have to subtract 21% of the $Cy3_{START}$ value from the $Cy3_{START}$ value, as well as from the $Cy3_{REM}$ value, in order count only the DRCs which actually were subjected to the external force. This subtraction is equivalent to a simple offset correction for the Cy3 fluorescence intensities. With this offset correction, the relative rupture probability (RRP) of the upper bond becomes:

$$\mathrm{RRP} = \frac{\mathrm{Cy3_{REM}} - \left(\mathrm{Cy3_{START}}\frac{\mathrm{AF647_{REM}}}{\mathrm{AF647_{START}}}\right)}{\mathrm{Cy3_{START}} - \left(\mathrm{Cy3_{START}}\frac{\mathrm{AF647_{REM}}}{\mathrm{AF647_{START}}}\right)}. \tag{3}$$

Figure 9(c) shows typical Cy3 fluorescence images both of the zip/shear and zip/zip spot, where the offset correction and the normalization—i.e. division by the offset corrected Cy3 start value—has been made directly within the image. As a consequence, in the corresponding histogram of offset corrected and normalized fluorescence intensities, the marked peak positions (left and middle), directly yield the RRP values for the two binding geometries. For the zip/shear and the zip/zip systems, the RRP values are 0.19 and 0.58 respectively.

The value of 0.58 is rather close to 50% which might be expected for a symmetrical DRC, like the one used here. However, the value of 0.19 for the shear/zip is far from 50%, although the base pairing free enthalpies, as well as the reaction rate constants of the two geometries used in this DRC, are expected to be identical. Nevertheless, when an external force is applied, the shear geometry opens more or less instantaneously, when the bond rupture force is exceeded, while in the zipper geometry the individual bases open in a consecutive manner. This corresponds to two entirely different reaction pathways in the binding potential landscape: to break a 30 bp duplex in shear geometry, a displacement of only 2 nm is required [35],

Table 1. Mean values and standard deviations of relative rupture probabilities (RRP) of a 30 bp duplex with perfectly matching sequences (GC), a GG single-base mismatch at position 13 (GG13) and a single-base mismatch at position twelve (CC12).

Duplex	RRP	σ
GC	0.41	0.013
GG13	0.28	0.004
CC12	0.21	0.014

while more than 20 nm are necessary to completely separate the two strands in the zipper geometry. According to literature values, the corresponding bond rupture forces should be around 45 and 14 pN, for shear and zipper geometry respectively [35, 19, 21, 18, 20], which is in good agreement with the low RRP of the zip/shear DRC. Nevertheless, it should be noted that, because of the statistical nature of the bond rupture process, the bond that ruptures within a DRC is not necessarily always the weaker bond in the complex. There is always a certain chance that the stronger bond, i.e. the one with the higher bond rupture force f^*, ruptures before the weaker one does, since the rupture probability distributions always have a certain overlap, where the weak bond may still be intact and the strong one may already rupture. The overlap of the two rupture probability distributions depends on the width of the distributions and on their separation, i.e. the difference $\Delta f^* = f^*_{\text{sample}} - f^*_{\text{reference}}$. Although, for a DNA zipper, the bond rupture probability distribution is rather narrow [19], the shear geometry exhibits a much broader distribution, with nonzero rupture probabilities, even at very small forces [35].

A good example of the high force resolution which can be achieved if two molecular bonds are directly compared to each other is shown in figure 10. Here, a perfectly matching 30 bp DNA duplex is compared to a 30 bp duplex with a single GG mismatch at position 13 (cf section 2.1.1 for details) and to a 30 bp duplex with a CC mismatch at position 12. Except for the indicated mismatches, all DNA duplexes again contain the same base composition. Figure 10 shows Cy3 fluorescence micrographs of typical spots for of the three DRCs, as well as the corresponding fluorescence intensity histograms. In the fluorescence images as well as in the histogram, all fluorescence intensities have been corrected for offset, and normalized with respect to the (offset-corrected) Cy3 start value, as described above for the zip/shear and zip/zip experiments. The dark green trace corresponds to the perfect match (PM), the middle one corresponds to the GG mismatch (GG13), and the light green one corresponds to the CC mismatch (CC12). The three peaks on the left-hand side of the histogram again directly reflect the RRP values of the three DRCs. The results of nine different spots (three for each DRC) are summarized in table 1. For the perfect match (GC) the mean RRP value is 0.41 ± 0.013, for the GG mismatch, it is 0.28 ± 0.004, and for the CC mismatch it is 0.21 ± 0.014. As expected, the DRC with perfect match has the highest RRP value, because the perfectly matching duplex at the bottom of the DRC is stronger than the mismatch containing duplexes of the other two DRCs, and perfect match and single nucleotide mismatch can be clearly distinguished. The value of 0.41 for the perfect match is again close to the expected 50% for a symmetric DRC.

The fact that the GG mismatch has a slightly higher RRP value than the CC mismatch is in agreement with the fact that a GG mismatch reduces the base pairing free enthalpy of DNA less than a CC mismatch, which has been attributed to the fact that although Watson–Crick base pairing is impaired for both types of mismatches, in the GG mismatch alternative hydrogen bond structures can be formed [36].

If we compare these results to AFM-based data, as indicated above, for the shear versus zip experiment, the clear discrimination of the two geometries is in good agreement with rather large Δf^* of approximately 30 pN (depending on the force loading rate), and the

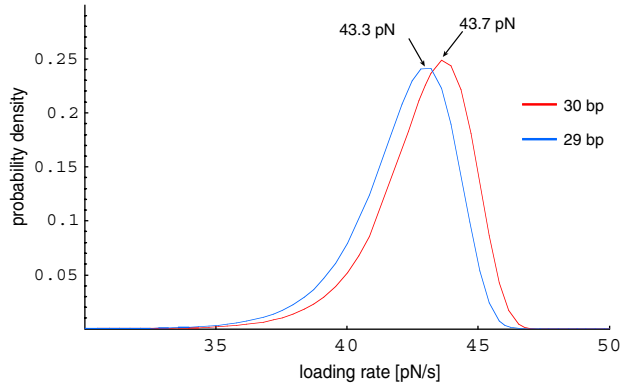

Figure 11. *Probability density functions.* Extrapolated bond rupture density probability functions for a 29 bp and a 30 bp duplex are shown. The extrapolations are based on experimental data for 10, 20, and 30 bp DNA duplexes, and on an extrapolation formula given in [35]. The blue line corresponds to the sample duplex of 29 bp, the red line to the reference complex of 30 bp. The most probable rupture forces are indicated by arrows. The force loading rate is 10^1pN s^{-1}.

narrow bond rupture probability distribution, especially of the DNA zipper. In the case of the single nucleotide mismatches, there are no direct AFM data available, because in this case the value of Δf^* is rather small and therefore extremely difficult to resolve with state of the art instrumentation. Nevertheless, one can use the interpolation formulae for $k_{\rm off}$ and for $x_{\rm b}$ given by Strunz *et al* [35], who determined the bond rupture forces of 10, 20, and 30 bp DNA duplexes by AFM, to derive bond rupture probability distributions for 29 bp and for 30 bp DNA duplexes at various force loading rates [14, 16], and use the Δf^* value as a first approximation. Figure 11 shows the calculated bond rupture probability distributions for a 29 bp and a 30 bp DNA duplex at force loading rates of 10 pN s^{-1}. This corresponds to separation velocities like those used in our experiments. The maximum (f^*) of the 29 bp distribution is at 43.3 pN, and the maximum of the 30 bp distribution is at 43.7 pN, resulting in a force difference Δf^* of only 0.4 pN. It should be pointed out, however, that this is the expected force difference if a single base is deleted at the end of one of the duplexes. In the case of a mismatch within the duplex, the nearest neighbour interactions—namely stacking interactions—with two neighbouring bases are affected, while at the end of the duplex only one nearest neighbour is actually affected. Therefore, in the case of single-base mismatch within the duplex, the expected force difference should be slightly larger than 0.4 pN. The expected force difference between a 28 bp and a 30 bp DNA duplex at 10 pN s^{-1}, which may serve an upper estimate, is 1.4 pN.

Based on our present knowledge about DNA base pairing forces, it is extremely difficult to estimate the expected force difference between a CC and a GG mismatch within a 30 bp DNA duplex. Nevertheless, our results clearly indicate that the differential force test can resolve force differences on the order of 1 pN or smaller. Yet, because a theoretical model, which would permit us to calculate the relative rupture probabilities of two bond in series, like in our DRCs, from the bond rupture probability distributions the individual bonds is still lacking, a direct comparison between AFM and DFA results is still difficult. Furthermore, in our present DFA set-up, only the separation velocity of the two surfaces can be controlled, and the force loading rate, which affects the rupture probabilities, has to be estimated from the velocity and from the elastic parameters of the stamp material. Nevertheless, although a shift in the force loading rates shifts the individual rupture probability distributions considerably, as long as the two bonds are similar, e.g. in the case of two different DNA duplexes which are both in shear

geometry, the distributions are both shifted in the same direction. Therefore, in such a case, the effect of force loading rate variations on the outcome of the experiment should be rather small.

4. Conclusion: technological applications and outlook

In this paper we have reviewed the fundamental concept, and the basic requirements, capabilities and limitations, as well as the latest technical advances, of the recently introduced differential force assay. We have discussed the conceptual difference between the measurement of rupture forces and of reaction rate constants. We have demonstrated that the differential force assay, which constitutes a completely new approach to compare intermolecular forces, has an unprecedented accuracy, as it can accurately discriminate between closely related DNA oligonucleotides, and resolve differences in bond rupture force of around 1 pN.

Although the results compare quite well with results obtained by more traditional methods, e.g. AFM-based force spectroscopy, a theoretical model for the forced dissociation of a construct containing two bonds in series, like in the DRCs, is still lacking. A suitable model would allow for direct comparison of fluorescence intensities on our chip surfaces, and bond rupture probability distributions determined from the fracture of single molecular bonds, or predict the relative rupture probabilities (RRPs) of the DRCs from single bond rupture probabilities.

As mentioned in section 1.3, a conceptually similar approach to the one discussed here has recently been described by Lang *et al* [26]. Here the external force is applied and monitored via a micro-bead in an optical trap. Their results comparing rupture forces of DNA in shear and zipper geometry agree quite well our data. The fact that the force which is applied to the DRC can be directly monitored and quantified with the optical trap is an evident advantage of the set-up used by Lang *et al*. With this set-up, it is not only possible to discriminate between different bond rupture forces, but the bond rupture force of the weaker bond, as well as the force loading rate, can be accurately determined. On the other hand, our approach uses a standard biochip format. This opens the door for technological applications of the DFA, which go far beyond comparing bond rupture forces of biomolecular bonds. The compatibility with standard biochip formats [25, 37, 38] allows for the use of the DFA for highly parallel diagnostic applications in a simple and straightforward manner. Because the DFA compares bond rupture forces, rather than equilibrium binding constants, like conventional biochips, it has the potential to overcome some of the shortcomings and limitation conventional DNA and protein biochip formats. Because in the DFA the two chip surfaces are separated on a millisecond to second timescale (the whole process takes a few seconds), slow thermal dissociation does not slow down the assay. Consequently, time-consuming washing steps, like overnight stringency washing, can be avoided. This is extremely valuable, especially for the analysis and detection of high-affinity binders, which play an increasingly important role in drug development and diagnostics, and which may have thermal off-rates of the order of days. In particular, when it comes to comparing large libraries of high-affinity binders and selecting the desired molecules—something which is traditionally done with surface plasmon spectroscopy—the DFA may speed up the selection process significantly. Furthermore, by choosing appropriate force references for each spot on a chip, it should in principle be possible to achieve stringent binding conditions for analyte molecules with different binding constants. And it has already been shown that the specificity and also the sensitivity, both extremely critical assay parameters of multiplexed sandwich immuno-assays (i.e. protein biochips), can be drastically improved [30].

Acknowledgments

The authors would like to acknowledge Gregor Neuert for providing the probability density simulations, E Sackmann for helpful discussions, and D Braun, M Stelzle and Philip Severin for support regarding the design of the contact device and the silicon moulds. This work was supported by the Deutsche Forschungsgemeinschaft (DFG).

References

[1] Bensimon D 1996 *Structure* **4** 885
[2] Merkel R 2001 *Phys. Rep.-Rev. Section of Phys. Lett.* **346** 344
[3] Janshoff A, Neitzert M, Oberdorfer Y and Fuchs H 2000 *Angew. Chem.-Int. Edn* **39** 3213
[4] Rief M and Grubmuller H 2002 *Chem. Phys. Chem.* **3** 255
[5] Clausen-Schaumann H, Seitz M, Krautbauer R and Gaub H E 2000 *Curr. Opin. Chem. Biol.* **4** 524
[6] Israelachvili J N and Tabor D 1972 *Proc. R. Soc.* A **331** 19
[7] Leckband D 2000 *Annu. Rev. Biophys. Biomol. Struct.* **29** 1
[8] Israelachvili J and Wennerstrom H 1996 *Nature* **379** 219
[9] Israelachvili J N 1992 *Intermolecular and Surface Forces* (San Diego, CA: Academic)
[10] Urbakh M, Klafter J, Gourdon D and Israelachvili J 2004 *Nature* **430** 525
[11] Beyer M K and Clausen-Schaumann H 2005 *Chem. Rev.* **105** 2921
[12] Zhurkov S N 1965 *Int. J. Fract. Mech.* **1** 311
[13] Bell G I 1978 *Science* **200** 618
[14] Evans E and Ritchie K 1997 *Biophys. J.* **72** 1541
[15] Evans E and Ritchie K 1999 *Biophys. J.* **76** 2439
[16] Evans E 2001 *Annu. Rev. Biophys. Biomol. Struct.* **30** 105
[17] Merkel R, Nassoy P, Leung A, Ritchie K and Evans E 1999 *Nature* **397** 50
[18] Essevaz-Roulet B, Bockelmann U and Heslot F 1997 *Proc. Natl Acad. Sci. USA* **94** 11935
[19] Bockelmann U, Essevaz-Roulet B and Heslot F 1997 *Phys. Rev. Lett.* **79** 4489
[20] Rief M, Clausen-Schaumann H and Gaub H E 1999 *Nat. Struct. Biol.* **6** 346
[21] Bockelmann U 2004 *Curr. Opin. Struct. Biol.* **14** 368
[22] Clausen-Schaumann H, Rief M, Tolksdorf C and Gaub H E 2000 *Biophys. J.* **78** 1997
[23] Gittes F and Schmidt C F 1998 *Eur. Biophys. J. Biophys. Lett.* **27** 75
[24] Viani M B, Schaffer T E, Chand A, Rief M, Gaub H E and Hansma P K 1999 *J. Appl. Phys.* **86** 2258
[25] Albrecht C, Blank K, Lalic-Multhaler M, Hirler S, Mai T, Gilbert I, Schiffmann S, Bayer T, Clausen-Schaumann H and Gaub H E 2003 *Science* **301** 367
[26] Lang M J, Fordyce P M, Engh A M, Neuman K C and Block S M 2004 *Nat. Methods* **1** 133
[27] Ekins R P and Chu F 1994 *Trends Biotechnol.* **12** 89
[28] Lipschutz R J, Fodor S P A, Gingeras T R and Lockhart D J 1999 *Nat. Genet.* **21** 20
[29] Mitchell P 2002 *Nat. Biotechnol.* **20** 225
[30] Blank K, Lankenau A, Mai T, Schiffmann S, Gilbert I, Hirler S, Albrecht C, Benoit M, Gaub H E and Clausen-Schaumann H 2004 *Anal. Bioanal. Chem.* **379** 974
[31] Xia Y and Whitesides G M 1998 *Annu. Rev. Mater. Sci.* **28** 153
[32] Delamarche M and Biebuyck H 1997 *Adv. Mater.* **9** 741
[33] http://www.nmi.de/englisch/showprj.php3?id=65&bereich=3&typ=2
[34] Engel J C J M, Bullen D and Liu C 2004 mass.micro.uiuc.edu/publications/papers/133.pdf
[35] Strunz T, Oroszlan K, Schafer R and Guntherodt H J 1999 *Proc. Natl Acad. Sci. USA* **96** 11277
[36] Hyther 2006 http://ozone2.chem.wayne.edu/Hyther/hythermenu.html
[37] Blank K, Mai T, Gilbert I, Schiffmann S, Rankl J, Zivin R, Tackney C, Nicolaus T, Spinnler K, Oesterhelt F, Benoit M, Clausen-Schaumann H and Gaub H E 2003 *Proc. Natl Acad. Sci. USA* **100** 11356
[38] Gilbert L, Schiffmann S, Rubenwolf S, Jensen K, Mail T, Albrecht C, Lankenau A, Beste G, Blank K, Gaub H E and Clausen-Schaumann H 2004 *Proteomics* **4** 1417

P3) Predicting the rupture probabilities of molecular bonds in series

Gregor Neuert, Christian H. Albrecht, Hermann E. Gaub

Biophysical Journal, 2007, **Accepted**

PREDICTING THE RUPTURE PROBABILITIES OF MOLECULAR BONDS IN SERIES

Gregor Neuert*#, Christian H. Albrecht* and Hermann E. Gaub*

*Ludwig-Maximilians-University Munich, chair for applied physics & Center for Nano Science, Amalienstrasse 54, 80799 Munich, Germany
#Massachusetts Institute of Technology, Department of Physics, 77 Massachusetts Ave., Cambridge, MA, 02139, USA

ABSTRACT

An assembly of two receptor ligand bonds in series will typically break at the weaker complex upon application of an external force. The rupture site depends highly on the binding potentials of both bonds and on the loading rate of the applied force. A model is presented that allows simulations of force induced rupture of bonds in series at a given force and loading rate based on the natural dissociation rates $k_{R0,S0}$ and the potential width $\Delta x_{R,S}$ of the reference and sample bonds. The model is especially useful for the analysis of differential force assay experiments. This is illustrated by experiments on molecular force balances consisting of two 30 bp oligonucleotide duplexes where $k_{R0,S0}$ and $\Delta x_{R,S}$ have been determined for different single nucleotide mismatches. Furthermore, prediction of the rupture site of two bonds in series is demonstrated for DNA duplexes in combination with streptavidin / biotin and anti-digoxigenin / digoxigenin respectively.

INTRODUCTION

Being a pivotal parameter in classical physics for centuries, force was not accessible on a molecular level in the biological sciences for a long time. Just recently single molecule experiments by means of force probe instruments like atomic force microscope (AFM) (1-5), optical trap (6,7), magnetic tweezers (8,9) and biomolecular force probe (BFP) (10,11) made it possible to investigate the mechanical properties of biological macromolecules (12,13). Receptor ligand bonds, which are commonly characterized by affinity measurements, have also been subject to single molecule force measurements. While affinities solely reflect the binding energy corresponding to the depth of the binding potential and therefore to the natural dissociation rate k_0, force measurements furthermore reveal an additional parameter, which is dependent on the unbinding pathway, the potential width Δx (14-16).

In order to derive Δx a variety of force transducers like cantilevers (16-18), optical tweezers (19,20) and even biological membranes (11,15) have been employed to record force extension curves of receptor ligand bonds . Recently a fundamentally different approach to probe molecular forces has been introduced by our group (Fig. 1) (21-25). Here the microscopic force transducer is substituted by a single molecular bond which is linked to the sample bond in series, thereby forming a “molecular force balance”. Upon application of a force at the ends of the balance, both bonds are probed simultaneously until the weaker one fails (21,22).

For highly symmetric combinations of sample (S) and reference (R) bonds, excellent sensitivity in terms of force differences is achieved, as demonstrated by detection of single nucleotide mismatches in DNA duplexes (21,22). However due to the lack of a theoretical description only ratios of discrimination have been assessed instead of quantitative differences in the natural dissociation rate of the reference k_{R0} and the sample k_{S0} bond as well as the potential width Δx_R and Δx_S.

Here we present a new theoretical approach for the analysis of force induced unbinding of two bonds in series. By means of a reference bond where the binding potential is well characterized (known k_{R0} and Δx_R), we are able to calculate the dissociation rate k_{S0} and potential width Δx_S for an arbitrary sample bond based on the well established Bell-Evans model for a given force and loading rate (14,26-28).

We apply this new analysis to experiments where small mutations have been introduced into a 30 bp oligonucleotide duplex. The results are compared to previous measurements on DNA oligonucleotides (17) and single chain antibodies performed by other groups (18). In general we corroborate the finding of those earlier studies, namely that differences in k_{R0} of a receptor ligand bond are closely coupled to the potential width Δx_R (17,18).

Moreover the theoretical model allows for predictions on alternative unbinding of any biological system where two bonds are probed in series. The model is particularly useful for simulations of force experiments (AFM, BFP, magnetic- and optical tweezers) where the sample is immobilized by affinity tags (7,20,29-34). Our approach allows one to predict whether a certain immobilization tag will survive the forces applied during the experiment or not.

MATERIALS AND METHODS

THE PRINCIPLE OF THE MOLECULAR FORCE BALANCE

The technology of the molecular force balance has been described elsewhere in detail (22). Briefly, amino labeled oligonucleotides are immobilized on an activated slide at their 3'-termini. Cy3 labeled oligonucleotides are now hybridized to the receptors, thereby forming a sample duplex. Subsequently biotin labeled oligonucleotides are hybridized to the sample thereby forming a reference duplex. This results in a molecular balance as it is depicted in Fig. 1. A stamp covered with streptavidin having an elevated microstructure is pressed onto the slide at this time. When the elevated area of the stamp makes contact with the slide, the biotinylated oligonucleotides will bind to the streptavidin. Following the formation of biotin-streptavidin bond the stamp is pulled away from the slide. The applied force will gradually increase until the reference duplex or the sample duplex ruptures, depending on which one is the weaker link. The Cy3-label of the middle oligonucleotide will therefore end up on the stamp when the sample duplex fails or on the slide when the reference duplex fails. Reading out the slide using a fluorescent scanner determines how much of the Cy3-oligonucleotide remained on the slide ($Cy3_{REM}$) in relation to the starting intensity $Cy3_{START}$. Thus the normalized $Cy3_{REM}$ intensity reflects the survival probability of the sample duplex Φ_S when probed against a certain reference duplex Φ_R. In principle Φ_S could also be deduced from the distribution of the Cy3-label between the stamp and the slide as described in (22), however it is easier and more accurate to accomplish

the read out just from the information on the slide. Therefore in the following the stamp images are not used for the analysis.
The structure of the molecular balances is shown in Table 1.

SURFACES AND INSTRUMENTATION

The silicone stamp had 16 protruding contact areas which themselves were micro structured by 100 x 100 µm squares elevated by 5 µm. It was functionalized by treatment with epoxy-silane, subsequently coated with bifunctional amino- biotin- PEG and finally covered with streptavidin. The amino-oligonucleotides were labeled at the 3'-termini and attached to aldehyde-functionalized glass slides. Following the hybridization of the other two oligonucleotides, stamp and slide were brought in contact by a piezoelectric element. The piezo allowed for precisely defined pulling velocities during surface separation (see (22) for details).

ANALYSIS OF FLUORESCENCE IMAGES

The image analysis procedure is shown in Fig. 2. The light gray DNA spot (Fig. 2 A) on a slide is depicted, where the fluorescence intensity of the Cy3-labeled oligo was measured. The area of contact between slide and stamp is equivalent to the darker squares, where the balances were probed and Cy3-labeled oligonucleotides were removed from the slide. The intensity of the darker squares corresponds to the remaining signal $Cy3_{REM}$. The light grid area is equivalent to the start intensity $Cy3_{START}$ where no contact was established between stamp and slide. The solid light grey line in Fig. 2 A indicates a region of interest (ROI-1) corresponding to the $Cy3_{REM}$ signal. Another two dashed black lines are enclosing the area of ROI-2 which corresponding to $Cy3_{START}$. The fluorescence intensity of the dark grey spot in Fig. 2 B represents biotin residues that have not coupled to the stamp and which have been labeled by soluble AlexaFluor647-streptavidin after the Cy3-scan was performed. Accordingly the AlexaFluor647 intensity of the dark squares reflects the coupling efficiency as discussed in (22). Here (ROI-3) and (ROI-4) are enclosing the remaining biotin density $AF647_{REM}$ and the starting biotin density $AF647_{START}$. For each of the 25 contact areas the mean intensities $Cy3_{REM}$, $Cy3_{START}$, $AF647_{REM}$ and $AF647_{START}$ have been determined. The degree of coupling was obtained by $AF647_{REM}$ / $AF647_{START}$. In order to correct the Cy3-signal for the coupling efficiency an offset of Cy3 was calculated from

$$Cy3_{offset} = Cy3_{REM} \cdot \frac{AF647_{REM}}{AF647_{START}} . \quad (1)$$

Finally the survival probability of the sample duplex Φ_S was calculated from $Cy3_{REM}$ corrected for the coupling efficiency and normalized to $Cy3_{START}$ according to Eq. 2:

$$\Phi_{S1-25} = \frac{Cy3_{REM} - Cy3_{offset}}{Cy3_{START} - Cy3_{offset}} \quad (2)$$

Since not all of the contact areas showed a high homogeneity in terms of intensity and a good coupling efficiency, those Φ_{S1-25} were selected which resulted in the minimal standard deviation (SD) for all of the measurement spots. This was the case for the following criteria: Coupling efficiency > 85%; $SD(Cy3_{START}) < 14\%$; $SD(Cy3_{REM}) < 12\%$; $SD(AF647_{START}) < 15\%$ and $SD(AF647_{REM}) < 49\%$. According to those criteria the SD for every kind of measurement spot (30PM, 30CC, 30GG and 29CC) was < 5% as indicated in Table 2.

CALCULATION OF DISSOCIATION RATES $K_{R0,S0}$ AND THE GIBB'S FREE ENERGY DIFFERENCES $\Delta G_{R,S}$

The Gibb's free energy difference $\Delta G_{R,S}$ for the DNA perfect match and mismatch duplexes was calculated by the computer program Hyther™ (35), which is based on the nearest neighbor algorithm refined for mismatches by SantaLucia (36,37), for 150mM Na+, 25°C and 100nM of each oligonucleotide. The dissociation rate $k_{R0,S0}$ of the duplexes were then calculated from the equilibrium constant of dissociation

$$K_D = \frac{k_{R0,S0}}{k_{on}} = e^{\frac{\Delta G_{R,S}}{k_B T}} \quad (3)$$

and with $k_{on} = 10^6\ M^{-1}\ s^{-1}$ based on the assumption that k_{on} is diffusion limited and identical for all DNA duplexes (38).

DETERMINATION OF LOADING RATE AND RUPTURE FORCE

The loading rate r and the corresponding rupture force f of the balance were estimated from the applied velocity v = 5 nm / s, the polymer spacer length L_0 = 30 nm, dissociation rate $k_{R0} = 2.81 \cdot 10^{-14}\ s^{-1}$ and potential width Δx_R = 2.8 nm of the reference duplex according the model from (28).

SIMULATIONS

Each survival probability for the reference Φ_R and the sample duplex Φ_S was simulated by increasing the force f and keeping the loading rate $r_{0,1,2,3,4}$ fixed at the same time. Simulations and data fits were performed with Mathematica™ and IGOR™.

RESULTS

THEORETICAL MODEL

Despite the fact that a differential force assay is carried out on a large ensemble of molecular balances at the same time, each of the balances is probed individually without cooperative effects from neighboring molecules. Therefore a single molecule approach is adequate for the theoretical description of the assay.

According to the experiments presented later, where the molecular balance comprises a constant reference duplex and a variable sample duplex, the goal of the simulation is to derive the survival probability Φ_S of the sample from the potential width Δx_S and the dissociation rate k_{S0} in a combination with a certain reference bond with Δx_R and k_{R0}.

In order to calculate Φ_S, the molecular force balance is modeled based on reaction rates as shown in Fig. 1 where Φ_R and Φ_S indicate survival probabilities for the reference and sample duplex respectively. According to Fig. 1, the time dependent rupture probabilities can be expressed as a system of coupled ordinary differential equations, depending only on the dissociation rates k_R and k_S:

$$\frac{d\varphi_B(t)}{dt} = \left(-k_R - k_S\right) \cdot \varphi_B(t) \quad (4\ A)$$

$$\frac{d\varphi_R(t)}{dt} = k_R \cdot \varphi_B(t) \quad (4\ B)$$

(4 C) $$\frac{d\varphi_S(t)}{dt} = k_S \cdot \varphi_B(t)$$

In order to solve Eqs. 4 A-C the probabilities of φ_B (t = 0) = 1, φ_R(t = 0) = 0 and φ_S (t = 0) = 0 are used as boundary conditions at t = 0 s when the bonds are just about to rupture. The association reaction is neglected based on the assumption that forced unbinding happens much faster than the association reaction. In contrast to the force balance experiment where intact bonds are detected by means of the fluorophor, the solution of the differential equations equals probabilities (φ_R(t)) and (φ_S(t)) which correspond to ruptured bonds. Therefore the survival probabilities Φ_R(t) and Φ_S(t) of the intact bonds are calculated from

(5 A) $$\Phi_R(t) = 1 - \varphi_R(t)$$

(5 B) $$\Phi_S(t) = 1 - \varphi_S(t)$$

and plotted as a function of time in Fig. 3A. Please note that all probability diagrams represent experiments on very large ensembles (n ~ 10^9) of molecular balances and not single molecule data.

In order to convert k_R and k_S into force dependent rates, the Bell-Evans model for force induced unbinding was applied to obtain

(6 A) $$k_R(f) = k_{R0}(f = 0) \cdot e^{f \cdot \Delta x_R / k_B T}$$

(6 B) $$k_S(f) = k_{S0}(f = 0) \cdot e^{f \cdot \Delta x_S / k_B T}$$

where $\Delta x_{R,S}$ is the distance between the bound and the transition state in a triangular binding potential and f is the external applied force. The constants k_{R0} and k_{S0} correspond to the natural dissociation rates in equilibrium, which were calculated from the free energy equilibrium constants K_D as discussed above. The applied force tilts the binding potential and thus lowers the transition state energy by $f \cdot \Delta x_{R,S}$, causing the reference and sample bond to dissociate faster. The rate constants in Eq. 1 are therefore substituted by the force dependent rates k_R=k_R(f) and k_S=k_S(f). An example for survival probability functions Φ_R(t, f) and Φ_S(t, f) for different external applied forces was plotted in Fig. 3 A over the logarithm of time. The time scale was normalized with respect to the time of dissociation of the reference bond at zero force $t_{R0} = k_{R0}^{-1}$. Since the experimentally accessible variables are the separation velocity v and force f, the loading rate r and the time were substituted by r = df/dt as shown in Fig. 3 B. With this substitution the final form of the differential equations is given in Eqs. 7 A-C and the solutions are plotted in Fig. 3 B.

(7 A) $$\frac{d\varphi_B(f,r)}{df} = \left(\frac{-k_{R0} \cdot e^{f \cdot \Delta x_R / k_B T} - k_{S0} \cdot e^{f \cdot \Delta x_S / k_B T}}{r} \right) \cdot \varphi_B(f,r)$$

(7 B) $$\frac{d\varphi_R(f,r)}{df} = \frac{k_{R0} \cdot e^{f \cdot \Delta x_R / k_B T}}{r} \cdot \varphi_B(f,r)$$

(7 C) $$\frac{d\varphi_S(f,r)}{df} = \frac{k_{S0} \cdot e^{f \cdot \Delta x_S / k_B T}}{r} \cdot \varphi_B(f,r)$$

Here the survival probability of the sample Φ_S and the reference bond Φ_R were plotted as a function of normalized force f / f_R with respect to the reference bond, where $f_R = k_BT / \Delta x_R$ is the characteristic force (10).
The experimentally acquired survival probability of the sample duplex Φ_S correspond to the point where the dotted red line converges towards the solid red line in the following diagrams. In Fig. 3 B and the following diagrams this point is highlighted by a black circle.

SIMULATIONS

In Fig. 4 A-D the binding potentials and survival probabilities for different types of molecular balances are depicted in dependence of loading rates and rupture forces. Depending on the grade of asymmetry the external force will bend the binding potential of the reference bond (blue lines) and the sample bond (red lines) to a different degree according to Eqs.7 A-C. In particular the reference bond is characterized by a Gibbs free energy difference of -45.02 k_BT and a potential width of 2.8 nm. With these two values, the binding potential and the potential width in Fig. 4 were normalized. Furthermore the natural dissociation rate was calculated to $k_{R0} = 2.82 \cdot 10^{-14}\ s^{-1}$, using Eq. 3. The potential width of the reference bond Δx_R sets the characteristic force for the reference bond according to $f_R = 4.14$ pN/nm / 2.8 nm = 1.48 pN.
In Fig. 4 A-D, left the binding potential was tilted by $f \cdot \Delta x_R$. Here we applied five different forces of multiples of f_R: $f_0 = 0$ pN, $f_1 = 10 \cdot f_R$, $f_2 = 20 \cdot f_R$, $f_3 = 30 \cdot f_R$, and $f_4 = 40 \cdot f_R$. The simulations for the survival probability Φ_S as a function of the normalized force f / f_R were then performed at five different loading rates of $r_0 = 0$ pN/s, $r_1 = 4 \cdot 10^{-9}$ pN/s, $r_2 = 1.5 \cdot 10^{-4}$ pN/s, $r_3 = 4$ pN/s, and $r_4 = 1 \cdot 10^{5}$ pN/s. (Fig. 4 A-D, right).

A. PERFECTLY SYMMETRIC BALANCES

A balance where the reference and the sample bond are equal in terms of $\Delta x_{R,S}$ and $k_{R0,S0}$ could be considered as perfectly symmetric. In Fig. 4 A two diagrams are shown for a perfectly symmetric molecular balance, where the binding potential for the reference bond and the sample bond is identical along the pulling direction ($k_{R0} = k_{S0} = 2.82 \cdot 10^{-14}\ s^{-1}$ and $\Delta x_R = \Delta x_S = 2.8$ nm). For simplicity a triangular potential was assumed based on the Bell - Evans model. On the left the normalized binding potential $\Delta E / \Delta G_R$ is depicted for different normalized unbinding forces f / f_R. The potentials of the reference bond (hidden blue line) and the sample bond (red line) are deformed to the same degree (left) and no shift in the survival probability Φ_S is observed in the probability diagram (right).

B. ASYMMETRY IN $K_{R0,S0}$

In this case a difference in $k_{R0,S0}$ was introduced into the sample bond by lowering the transition state by 1 k_BT ($k_{S0} = 8.46 \cdot 10^{-14}\ s^{-1}$) while the reference bond was not changed at all ($k_{R0} < k_{S0}$), but leaving the potential width equal ($\Delta x_R = \Delta x_S$). As shown for the potentials in Fig. 4 B (left) the red and the blue lines are shifted to each other indicating the asymmetry between the two bonds (right). As for the symmetric case in Fig. 4 A the system is not affected in terms of the rupture probabilities by a change in loading rate since both binding potentials are tilted by the same energy $f \cdot \Delta x_R = f \cdot \Delta x_S$.

C. ASYMMETRY IN $\Delta X_{R,S}$

Here the potential width of the reference bond was chosen to be wider than the sample bond ($\Delta x_R > \Delta x_S$, $\Delta x_S = 2.66$ nm) while the potential depths were kept equal ($k_{R0} = k_{S0}$). As demonstrated in

Fig. 4 C (right), the asymmetry in $\Delta x_{R,S}$ results in a pronounced dependence of the unbinding process on the force rate. Since the sample bond has a smaller Δx_S, larger rupture probabilities than for the reference bond are observed. As a consequence the survival probability of the sample bond Φ_S (red line, right) converges towards 1 for high loading rates.

D. COMBINED ASYMMETRY

Finally in Fig. 4 D an example for the combination of asymmetries in potential widths (Δx_S = 2.66 nm, $\Delta x_R > \Delta x_S$) and depths ($k_{S0} = 8.46 \cdot 10^{-14}$ s^{-1}, $k_{R0} < k_{S0}$) is presented. As evidenced in the probability diagram, the sample bond is weaker then the reference bond at zero force (f = 0) and for small loading rates. However at higher loading rates the disadvantage due to the larger k_{S0} is successively compensated by the advantage of a shorter Δx_S. After the red line in the right graph has crossed the 0.5 line (between rupture forces f_2 and f_3) again an asymptotic increase towards 1 is observed.

EXPERIMENTS

The theoretical concept presented above was corroborated with experiments on short oligonucleotide duplexes as previously published (22) with the goal to derive Δx_S values for several mutations in the sample duplex. With the data available in the literature (17), the assumption of triangular potentials for the reference and the sample complex are made as shown in Fig. 4 A-D.

For the simulation the following input parameters are required:

- The survival probabilities of the sample bond Φ_S which are calculated from the fluorescence intensities as described in the methods section and listed in Table 2.
- The velocity v by which the molecules are probed is assumed to be identical to the pulling velocity.
- The loading rate and the corresponding rupture force were simulated from k_{R0}, Δx_R and the velocity v as described in the methods section. Based on the pulling velocity of v = 5 nm / s the loading rate equals 37 pN / s at a rupture force of 48 pN.
- Natural dissociation rates $k_{R0,S0}$ at zero force for the reference duplex and the sample duplex were calculated from $\Delta G_{R,S}$ values as described in the methods section.
- The potential width of the reference bond Δx_R was derived from (17) which is 2.8 nm.

For the simulation, the above mentioned variables were kept constant and only Δx_S was varied until the minima of the curves matched the measured Φ_S values (compare to Fig. 4 and 5 A). Then the corresponding potential width Δx_S was extracted.

The probability diagrams for all sample duplexes are plotted in Fig. 5 A, showing experimental data (light grey bars) for the perfect match as well as the 30GG, 30CC, and the 29CC mismatches. In order to get an impression about the correlation between the rupture probability and the dissociation rate k_{S0}, the measured survival probability of the sample bond Φ_S was plotted in Fig. 5 A over the normalized natural dissociation rate k_{S0} / k_{R0}. To calculate survival probabilities of the sample bond (shown as black line), only the potential width of the sample bond was varied. The resulting normalized potential width $\Delta x_S / \Delta x_R$ is plotted in Fig. 5 B as a function of the normalized natural dissociation rate of the sample complex k_{S0} / k_{R0}.

Table 2 summarizes the input parameters for all sample duplexes and the reference duplex. Also the $\Delta x_{R,S}$ values are listed which were calculated by using the differential equation Eqs. 7 A-C

(with exception of $\Delta x_{R,S}$ for the 30 bp perfect match which was taken from the data provided in (17)).
Besides the analysis of force balance measurements our simulations are useful for designing force experiments where the sample is bound to a surface by a receptor ligand immobilization tag. In Fig. 6 two simulations of AFM experiments are depicted, where streptavidin / biotin (A) and anti–digoxigenin / digoxigenin (B) respectively are used to immobilize a 15 bp DNA duplex. Again survival probabilities for the DNA (blue) and for the immobilization tag (red) are plotted as function of the normalized force for different loading rates. Here the reference duplex is a 15 bp DNA duplex with a natural dissociation rate of $k_{R0} = 3.16 \cdot 10^{-5}\ s^{-1}$, a potential width of $\Delta x_R = 1.75$ nm, and a characteristic force $f_R = 2.36$ pN. For a loading rate of 37 pN / s the survival probability of the immobilization tag (red) is highlighted by a black circle. It is evident from Fig. 6 A, which the streptavidin survives over the whole force range with a likelihood of more than 99 %. In contrast, the antibody bond is not sufficiently strong for the experiment and would fail with a probability of about 90 %.

DISCUSSION

We can proceed from the assumption that for a molecular force balance, which is perfectly symmetric in terms of $k_{R0,S0}$ and $\Delta x_{R,S}$, the relative rupture probability is independent of any changes in pulling velocity and loading rate (Fig. 4 A). However, even small variations of the sample duplex binding potential breaks the symmetry and gives rise to significant differences in survival probability as illustrated by Fig. 4 B and 4 C. Compared to the fully symmetric balance in 4 A, where both the reference and the sample bond survival probabilities converge towards 0.5, a huge shift is observed when ΔG_S and Δx_S of the sample bond are changed just between 2 - 5 % compared to the reference bond. Interestingly, for changes in k_{S0}, Φ_S stays constant over the whole loading range, while for changes in Δx_S, Φ_S varies with an increase of the applied loading rate.

As shown by Strunz et. al. (17) deletions of peripheral base pairs from a 30 bp DNA duplex give rise to decreasing k_{S0} and increasing Δx_S. Since the deletion affects both variables in the opposite direction it is evident that a substantial part of the lowering in binding energy is compensated by a decrease in Δx_S when we consider the resulting survival probabilities. This is illustrated by Fig. 4 D where a case with differences in $k_{R0,S0}$ and $\Delta x_{R,S}$ was simulated. It is evident from the red line that the drop in the survival probability of the sample complex Φ_S becomes smaller for increasing loading rates, since the difference in $\Delta x_{R,S}$ causes an asymptotic rise which compensates the differences between k_{R0} and k_{S0}.

In contrast to DNA duplexes, no such correlation was generally expected for an antibody antigen system like that investigated by Schwesinger et. al. (18). There the effect of single amino acid exchanges in the binding pocket of anti-hapten single chain fragment (scFv) antibodies was analyzed by AFM force spectroscopy. Since the mutations should not have altered the geometry of the binding pocket, $\Delta x_{R,S}$ was assumed to be constant despite changes in the binding energy. Surprisingly, the antibody system shows a qualitatively similar behavior as the DNA duplexes studied by Strunz. Again a linear correlation between the logarithm of the natural dissociation rate k_{S0} and the potential width Δx_S was found as shown in Fig. 5 A.

For the experiments presented here we have introduced internal base pair mismatches to the DNA duplex, because such mutations have about the half effect on ΔG_S compared to a 10 bp deletion (17), but without affecting the contour length of the duplex. Therefore we expected the effect of the mutations on Δx_S to be rather small compared to the 10 bp deletions.

To facilitate a quantitative comparison of our data to that of Strunz et. al., we calculated $\Delta G_{R,S}$ values based on the nearest neighbor algorithm as explained above for both experiments. In Fig. 5 B the normalized potential width Δx_S / Δx_R over normalized dissociation rate k_{S0} / k_{R0} is plotted and in accordance to the procedure from Schwesinger et. al. we obtained a slope for the Strunz data of 0.53 (17) close to the value measured by Schwesinger for the scFv-antibodies of 0.3 (18). In contrast to that our point mutations resulted in an even higher slope of 0.8. In other words: A single point mutation like the CC homoduplex accounts for a difference in ΔG_S comparable to a 8 bp deletion (7.8 k_BT) but equals a shift in Δx_S comparable to a 10 bp deletion according to the equation from Strunz. Hence the compensation of ΔG_S (k_{S0}) by Δx_S in terms of the resulting survival probability Φ_S is more pronounced for internal mismatches than for peripheral deletions in DNA. This may be an explanation for the fact that discrimination of mismatches has not been reported for the AFM so far in contrast to energetically comparable peripheral deletions (17).

As seen in Fig. 5, the experimental data are reproduced very well using the approximation of triangular potentials for the reference and the sample complex (17). Furthermore, this framework of comparing two bonds in series is also extendible to other potential shapes. If the reference potential is know in better detail, a wide range of loading rates can be measured, because only the differences between the potentials of the reference and the sample complexes are measured. And even if these differences are small, this method has the potential to resolve them.

There are some potential challenges in applying this technique directly to molecular interactions when the spontaneous dissociation rates become comparable to the timescale of the experiment. If the sample and the reference complex are too weak, they start to dissociate even during assembly of the assay. The consequence will be a change of concentrations of reference and sample complex during the experiment without applying a force. But if one uses the experimental setup above to measure the interactions of molecules that bind to only the sample DNA, it is in principle possible to measure also weaker interactions. These interactions act only on the sample complex in the time frame of the contact of the stamp with the slide and not during the assembly of the assay.

In addition to analyzing force balance experiments the theoretical model also was applied to prove the suitability of immobilization tags for force experiments as illustrated in Fig. 6. The fact that streptavidin / biotin (Fig. 6 A) is very well suited for immobilization of samples under force is again corroborated by the simulation for forces at least up to 100 pN. In contrast to that it is critical to rely on a single digoxigenin / antibody-bond which fail for low loading rates in comparison to a 15mer DNA (Fig. 6 B).

Furthermore it is evident that DNA duplexes may be used as reference bonds in order to determine the k_{S0} and Δx_S values of protein receptors like the anti-digoxigenin antibody. However for the streptavidin / biotin bond it would be hard to find a matching DNA duplex, since the rupture force of 15 bp is much to low and even much longer DNA double strands will not exceed the 65 pN barrier of the BS-transition (39,40).

ACKNOWLEDGEMENTS
We thank Robert Lugmaier, Julia Morfill, Kay Gottschalk, Dominik Ho, Katja Falter and Erich Sackmann for helpful discussions. This work was supported by the Deutsche Forschungsgemeinschaft through the Nano-Initiative Munich.

REFERENCES

1. Rief, M., M. Gautel, F. Oesterhelt, J. M. Fernandez, and H. E. Gaub. 1997. Reversible unfolding of individual titin immunoglobulin domains by AFM. Science 276:1109-1112.

2. Rief, M., F. Oesterhelt, B. Heymann, and H. E. Gaub. 1997. Single molecule force spectroscopy on polysaccharides by atomic force microscopy. Science 275:1295-1297.

3. Grandbois, M., M. Beyer, M. Rief, H. Clausen-Schaumann, and H. E. Gaub. 1999. How strong is a covalent bond? Science 283:1727-1730.

4. Hugel, T. and M. Seitz. 2001. The study of molecular interactions by AFM force spectroscopy. Macromolecular Rapid Communications 22:989-1016.

5. Hugel, T., N. B. Holland, A. Cattani, L. Moroder, M. Seitz, and H. E. Gaub. 2002. Single-molecule optomechanical cycle. Science 296:1103-1106.

6. Bustamante, C. 2005. Unfolding single RNA molecules: bridging the gap between equilibrium and non-equilibrium statistical thermodynamics. Q Rev Biophys 38:291-301.

7. Bockelmann, U. 2004. Single-molecule manipulation of nucleic acids. Current Opinion in Structural Biology 14:368-373.

8. Charvin, G., T. R. Strick, D. Bensimon, and V. Croquette. 2005. Tracking topoisomerase activity at the single-molecule level. Annual Review Of Biophysics And Biomolecular Structure 34:201-219.

9. Gore, J., Z. Bryant, M. Nollmann, M. U. Le, N. R. Cozzarelli, and C. Bustamante. 2006. DNA overwinds when stretched. Nature 442:836-839.

10. Evans, E. 1998. Energy landscapes of biomolecular adhesion and receptor anchoring at interfaces explored with dynamic force spectroscopy. Faraday Discussions:1-16.

11. Merkel, R. 2001. Force spectroscopy on single passive biomolecules and single biomolecular bonds. Physics Reports-Review Section of Physics Letters 346:344-385.

12. Holland, N. B., T. Hugel, G. Neuert, A. Cattani-Scholz, C. Renner, D. Oesterhelt, L. Moroder, M. Seitz, and H. E. Gaub. 2003. Single molecule force spectroscopy of

azobenzene polymers: Switching elasticity of single photochromic macromolecules. Macromolecules 36:2015-2023.

13. Neuert, G., T. Hugel, R. R. Netz, and H. E. Gaub. 2006. Elasticity of poly(azobenzene-peptides). Macromolecules 39:789-797.

14. Bell, G. I. 1978. Models for the specific adhesion of cells to cells. Science 200:618-627.

15. Merkel, R., P. Nassoy, A. Leung, K. Ritchie, and E. Evans. 1999. Energy landscapes of receptor-ligand bonds explored with dynamic force spectroscopy. Nature 397:50-53.

16. Neuert, G., C. Albrecht, E. Pamir, and H. E. Gaub. 2006. Dynamic force spectroscopy of the digoxigenin-antibody complex. Febs Letters 580:505-509.

17. Strunz, T., K. Oroszlan, R. Schafer, and H. J. Guntherodt. 1999. Dynamic force spectroscopy of single DNA molecules. Proc Natl Acad Sci U S A 96:11277-11282.

18. Schwesinger, F., R. Ros, T. Strunz, D. Anselmetti, H. J. Guntherodt, A. Honegger, L. Jermutus, L. Tiefenauer, and A. Pluckthun. 2000. Unbinding forces of single antibody-antigen complexes correlate with their thermal dissociation rates. Proc Natl Acad Sci U S A 97:9972-9977.

19. Nishizaka, T., H. Miyata, H. Yoshikawa, S. Ishiwata, and K. Kinosita. 1995. Unbinding Force of a Single Motor Molecule of Muscle Measured Using Optical Tweezers. Nature 377:251-254.

20. Lang, M. J., P. M. Fordyce, A. M. Engh, K. C. Neuman, and S. M. Block. 2004. Simultaneous, coincident optical trapping and single-molecule fluorescence. Nature Methods 1:133-139.

21. Albrecht, C., K. Blank, M. Lalic-Multhaler, S. Hirler, T. Mai, I. Gilbert, S. Schiffmann, T. Bayer, H. Clausen-Schaumann, and H. E. Gaub. 2003. DNA: a programmable force sensor. Science 301:367-370.

22. Albrecht, C. H., H. Clausen-Schaumann, and H. E. Gaub. 2006. Differential analysis of biomolecular rupture forces. Journal Of Physics-Condensed Matter 18:S581-S599.

23. Blank, K., A. Lankenau, T. Mai, S. Schiffmann, I. Gilbert, S. Hirler, C. Albrecht, M. Benoit, H. E. Gaub, and H. Clausen-Schaumann. 2004. Double-chip protein arrays: force-based multiplex sandwich immunoassays with increased specificity. Analytical and Bioanalytical Chemistry 379:974-981.

24. Blank, K., T. Mai, I. Gilbert, S. Schiffmann, J. Rankl, R. Zivin, C. Tackney, T. Nicolaus, K. Spinnler, F. Oesterhelt, M. Benoit, H. Clausen-Schaumann, and H. E. Gaub. 2003. A force-based protein biochip. Proceedings of the National Academy of Sciences of the United States of America 100:11356-11360.

25. Gilbert, L., S. Schiffmann, S. Rubenwolf, K. Jensen, T. Mail, C. Albrecht, A. Lankenau, G. Beste, K. Blank, H. E. Gaub, and H. Clausen-Schaumann. 2004. Double chip protein arrays using recombinant single-chain Fv antibody fragments. Proteomics 4:1417-1420.

26. Evans, E. and K. Ritchie. 1997. Dynamic strength of molecular adhesion bonds. Biophysical Journal 72:1541-1555.

27. Evans, E. and K. Ritchie. 1999. Strength of a weak bond connecting flexible polymer chains. Biophysical Journal 76:2439-2447.

28. Friedsam, C., A. K. Wehle, F. Kühner, and H. E. Gaub. 2003. Dynamic single-molecule force spectroscopy: bond rupture analysis with variable spacer length. Journal of Physics-Condensed Matter 15:S1709-S1723.

29. Allemand, J. F., D. Bensimon, and V. Croquette. 2003. Stretching DNA and RNA to probe their interactions with proteins. Current Opinion in Structural Biology 13:266-274.

30. Berquand, A., N. Xia, D. G. Castner, B. H. Clare, N. L. Abbott, V. Dupres, Y. Adriaensen, and Y. F. Dufrene. 2005. Antigen binding forces of single antilysozyme Fv fragments explored by atomic force microscopy. Langmuir 21:5517-5523.

31. Evans, E. 2001. Probing the relation between force--lifetime--and chemistry in single molecular bonds. Annu Rev Biophys Biomol Struct 30:105-128.

32. Gore, J., Z. Bryant, M. D. Stone, M. Nollmann, N. R. Cozzarelli, and C. Bustamante. 2006. Mechanochemical analysis of DNA gyrase using rotor bead tracking. Nature 439:100-104.

33. Hinterdorfer, P. and Y. F. Dufrene. 2006. Detection and localization of single molecular recognition events using atomic force microscopy. Nat Methods 3:347-355.

34. Williams, M. C. and I. Rouzina. 2002. Force spectroscopy of single DNA and RNA molecules. Current Opinion in Structural Biology 12:330-336.

35. http://ozone3.chem.wayne.edu/cgi-bin/login/login/showLoginPage.cgi.

36. SantaLucia, J., Jr. 1998. A unified view of polymer, dumbbell, and oligonucleotide DNA nearest-neighbor thermodynamics. Proc Natl Acad Sci U S A 95:1460-1465.

37. Peyret, N., P. A. Seneviratne, H. T. Allawi, and J. SantaLucia, Jr. 1999. Nearest-neighbor thermodynamics and NMR of DNA sequences with internal A.A, C.C, G.G, and T.T mismatches. Biochemistry 38:3468-3477.

38. Northrup, S. H. and H. P. Erickson. 1992. Kinetics of protein-protein association explained by Brownian dynamics computer simulation. Proc Natl Acad Sci U S A 89:3338-3342.

39. Smith, S. B., Y. J. Cui, and C. Bustamante. 1996. Overstretching B-DNA: The elastic response of individual double-stranded and single-stranded DNA molecules. Science 271:795-799.

40. Cluzel, P., A. Lebrun, C. Heller, R. Lavery, J. L. Viovy, D. Chatenay, and F. Caron. 1996. DNA: an extensible molecule. Science 271:792-794.

41. Pincet, F. and J. Husson. 2005. The solution to the streptavidin-biotin paradox: The influence of history on the strength of single molecular bonds. Biophysical Journal 89:4374-4381.

TABLE CAPTIONS

TABLE 1 Four molecular force balances are depicted each comprising an amino-oligo (top), a Cy3-oligo middle and a biotin-oligo (bottom). Amino- and biotin-oligos are identical in all balances. Mutations are only introduced by single nucleotide exchanges (30GG, 30CC, 29CC) and a single nucleotide deletion (29CC) in the Cy3-oligonucleotides (underlined bases).

dir.	duplex	no.	sequence
3'-5'	30PM	#66	NH2-20t-CTGCAGGAATTCGATATCAAGCTTATCGAT
5'-3'		#74	GACGTCCTTAAGCTATAGTTCGAATAGCTAc-17t-cATCGATAAGCTTGATATCGAATTCCTGCAGttttt-Cy3
3'-5'	30PM	#62	TAGCTATTCGAACTATAGCTTAAGGACGTC-20*t-Biotin
3'-5'	30GG	#66	NH2-20t-CTGCAGGAATTCGATATCAAGCTTATCGAT
5'-3'		#75	GACGTCCTTAAGGTATAGTTCGAATAGCTAc-17t-cATCGATAAGCTTGATATCGAATTCCTGCAGttttt-Cy3
3'-5'	30PM	#62	TAGCTATTCGAACTATAGCTTAAGGACGTC-20*t-Biotin
3'-5'	30CC	#66	NH2-20t-CTGCAGGAATTCGATATCAAGCTTATCGAT
5'-3'		#80	GACGTCCTTAACCTATAGTTCGAATAGCTAc-17t-cATCGATAAGCTTGATATCGAATTCCTGCAGttttt-Cy3
3'-5'	30PM	#62	TAGCTATTCGAACTATAGCTTAAGGACGTC-20*t-Biotin
3'-5'	29CC	#66	NH2-20t-CTGCAGGAATTCGATATCAAGCTTATCGAT
5'-3'		#86	_ACGTCCTTAACCTATAGTTCGAATAGCTAc-17t-cATCGATAAGCTTGATATCGAATTCCTGCAGttttt-Cy3
3'-5'	30PM	#62	TAGCTATTCGAACTATAGCTTAAGGACGTC-20*t-Biotin

TABLE 2 Summary of the input parameters for the simulations and the resulting potential width $\Delta x_{R,S}$ values. $\Delta G_{R,S}$ is the Gibbs free energy difference, $k_{R0,S0}$ is the natural dissociation rate, Φ_S measured survival probability.

duplex	Φ_S	$\Delta G_{R,S}$ [k_BT]	$k_{R0,S0}$ [s^{-1}]	$\Delta x_{R,S}$ [nm]
reference	-	-45.02	$2.82 \cdot 10^{-14}$	2.800
30PM	0.406 ± 0.016	-45.02	$2.82 \cdot 10^{-14}$	2.834 ± 0.006
30GG	0.271 ± 0.010	-41.88	$6.49 \cdot 10^{-13}$	2.612 ± 0.005
30CC	0.199 ± 0.010	-37.24	$6.76 \cdot 10^{-11}$	2.228 ± 0.005
29CC	0.179 ± 0.009	-35.39	$4.26 \cdot 10^{-10}$	2.072 ± 0.005

FIGURE CAPTION

FIGURE 1 Experimental setup of the molecular force balance.
A molecular force balance consisting of a reference bond (blue) and a sample bond (red) is immobilized between to chip surfaces in contact (left). Upon separation of the surfaces force builds up in the balance until one of the bonds fails (right). The location of the fluorescent label after the separation indicates whether the reference or the sample bond was ruptured. The bond survival probability $\Phi_{R,S}$ depends on the rates of the reference bond k_R and the sample bond k_S.

FIGURE 2 Fluorescent images are shown for the slide after separation of the stamp. (A) Image of the Cy3 fluorescent signal of a spot after separation. (B) The same spot after binding of fluorescent-streptavidin to the free biotin. Dark squares correspond to the contact area where the balances have ruptured. $Cy3_{START}$ intensity and $AF647_{START}$ intensity have been derived from ROI-1 and ROI-3 respectively. $Cy3_{REM}$ intensity and $AF647_{REM}$ intensity have been derived from ROI-3 and ROI-4 and correspond to the grid around one contact area.

FIGURE 3 Solutions of the Eqs. 6 A-C are plotted for a symmetric balance with $t_{R0}=1/k_{R0} = 3.55 \cdot 10^{13}$ s, $k_{R0,S0} = 2.82 \cdot 10^{-14}$ s^{-1} and $\Delta x_{R,S} = 2.8$ nm. (A) Survival probabilities of the reference bonds (blue) and sample bonds (red) as function of the logarithm of the normalized dissociation time for rupture forces of $f_0 = 0$ pN, $f_1 = 10 \cdot f_R$, $f_2 = 20 \cdot f_R$, $f_3 = 30 \cdot f_R$, and $f_4 = 40 \cdot f_R$ with $f_R = k_BT / \Delta x_R = 1.48$ pN are plotted. (B) The same survival probabilities are plotted as shown in (A) as a function of normalized force f / f_R for loading rates $r_0 = 0$ pN/s, $r_1 = 4 \cdot 10^{-9}$ pN/s, $r_2 = 1.5 \cdot 10^{-4}$ pN/s, $r_3 = 4$ pN/s, and $r_4 = 1 \cdot 10^5$ pN/s. Black circles indicate the point where all balances are ruptured for different rupture forces $f_{0,\,1,\,2,\,3,\,4}$.

FIGURE 4 Influence of the shape of triangular binding potentials for two bonds in series.
The two binding potentials of the reference (blue) and the sample (red) bond are plotted on left. The differences in potential width and depth are magnified in the inserts. The resulting survival probabilities of the two bonds are plotted on the right side. The loading rates are $r_0 = 0$ pN/s, $r_1 = 4 \cdot 10^{-9}$ pN/s, $r_2 = 1.5 \cdot 10^{-4}$ pN/s, $r_3 = 4$ pN/s, and $r_4 = 1 \cdot 10^5$ pN/s. The applied forces are $f_0 = 0$ pN, $f_1 = 10 \cdot f_R$, $f_2 = 20 \cdot f_R$, $f_3 = 30 \cdot f_R$, and $f_4 = 40 \cdot f_R$ with $f_R = k_BT / \Delta x_R = 1.48$ pN.
A) Perfectly symmetric molecular balance with identical potential width $\Delta x_{R,S} = 2.8$ nm and natural dissociation rates $k_{R0,S0} = 2.82 \cdot 10^{-14}$ s^{-1} . Black circles indicate the survival probability for the sample bond (red curves) for a given loading rate $r_{0,1,2,3,4}$ and rupture force $f_{0,1,2,3,4}$.
(B) Asymmetry in potential depth which corresponds to an asymmetry in $k_{R0,S0}$ for a molecular balance with identical $\Delta x_{R,S}$ but different $k_{S0} = 8.46 \cdot 10^{-14}$ s^{-1}. The survival probability of the sample bonds which is indicated by the black circles is the same for different loading rates $r_{0,1,2,3,4}$ and rupture forces $f_{0,1,2,3,4}$.
(C) Asymmetry in $\Delta x_{R,S}$ with identical $k_{R0,S0}$ but different $\Delta x_S = 2.66$ nm. The survival probability of the sample bonds which is indicated by the black circles rises with higher loading rates and rupture forces.
(D) Mixed asymmetry with differences in $k_{R0,S0}$ ($k_{R0} = 2.82 \cdot 10^{-14}$ s^{-1}, $k_{S0} = 8.46 \cdot 10^{-14}$ s^{-1}) and $\Delta x_{R,S}$ ($\Delta x_R = 2.8$ nm ,$\Delta x_S = 2.66$ nm). The sample bonds (red curve) have a lower survival probability than the reference bonds (blue curve) for low loading rates but rises with higher loading rates and rupture forces. The crossover occurs at a rate of $r_c = 9 \cdot 10^{-4}$ pN/s.

FIGURE 5 Combined data from different experiments (light grey bars) and simulations (black line) on a 30mer PM, 30mer GG MM, 30mer CC MM and a 29mer CC MM. (A) Survival property of the sample duplex Φ_S plotted as a function of normalized dissociation rate k_{S0} / k_{R0} on a log scale. (B) Calculated normalized potential width of the sample duplex $\Delta x_S / \Delta x_R$ is plotted as a function of the corresponding normalized dissociation rate of the sample duplex k_{S0} / k_{R0} that match the survival probabilities in (A). The pulling velocity was v = 5 nm / s, resulting in a loading rate of 37 pN / s at a rupture force of 48 pN.

FIGURE 6 Simulation of possible AFM experiments using two bonds in series. The reference bond is a 15 bp DNA duplex (blue) which was immobilized by (A) streptavidin / biotin (red) and (B) anti–digoxigenin / digoxigenin (red). Black circles indicate survival probability of the immobilization tag at $f_1 = 23$ pN and $r_1 = 37$ pN / s (dotted curves). The black circle on the solid line indicates survival probabilities at zero force (f_0) and loading rate (r_0). Reference: $k_{R0} = 3.16 \cdot 10^{-5}$ s^{-1} and $\Delta x_R = 1.75$ nm for 15 bp DNA (17); Sample (A): $k_{S0} = 3.71 \cdot 10^{-6}$ s^{-1} and $\Delta x_S = 1.31$ nm for streptavidin / biotin (41).(B) $k_{S0} = 0.015$ s^{-1} and $\Delta x_S = 1.15$ nm for anti-digoxigenin / digoxigenin (16).

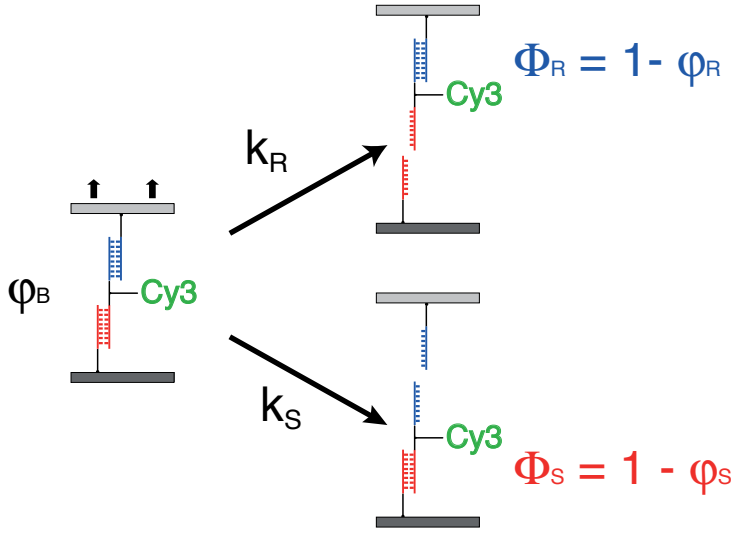

Neuert_figure1

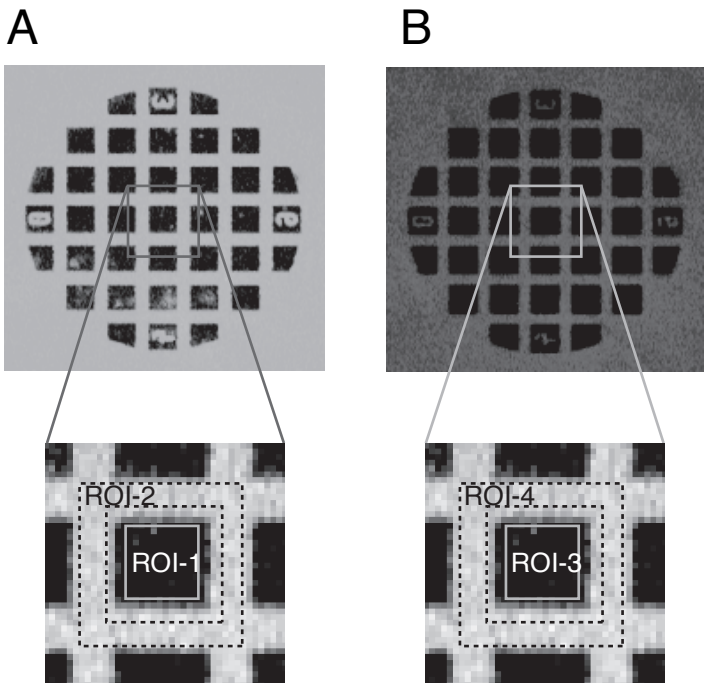

Neuert_figure2

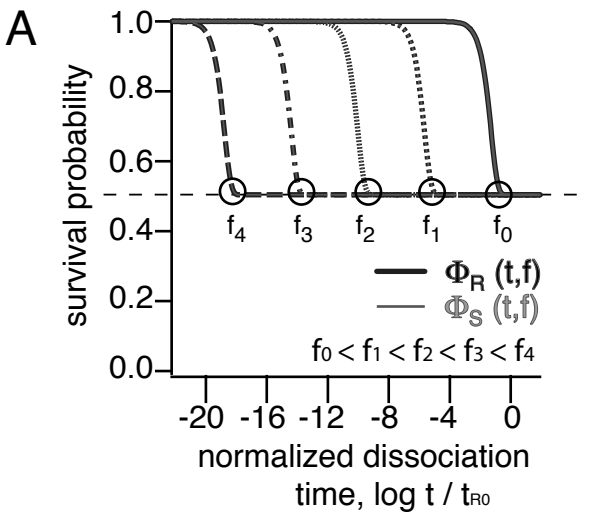

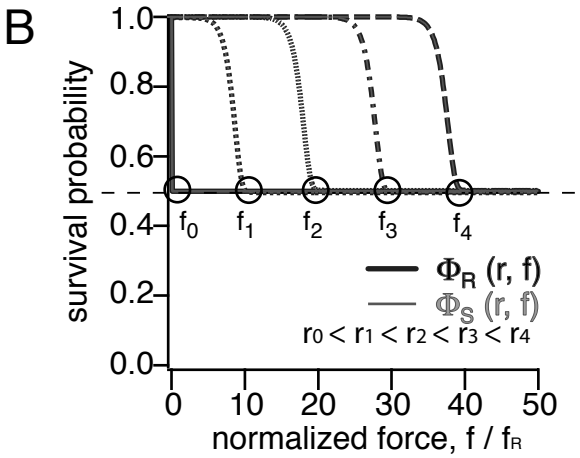

Neuert_figure3

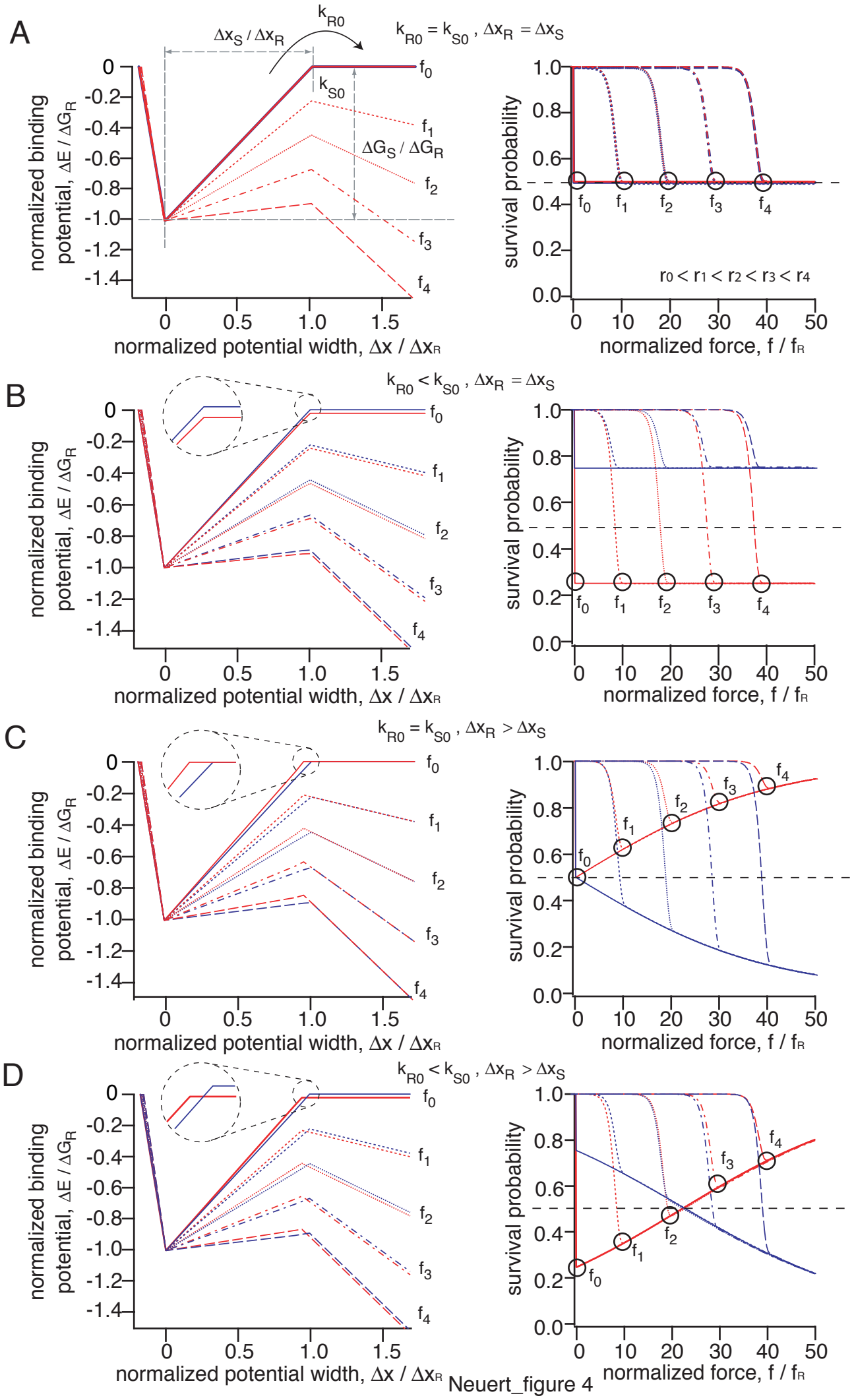

Neuert_figure 4

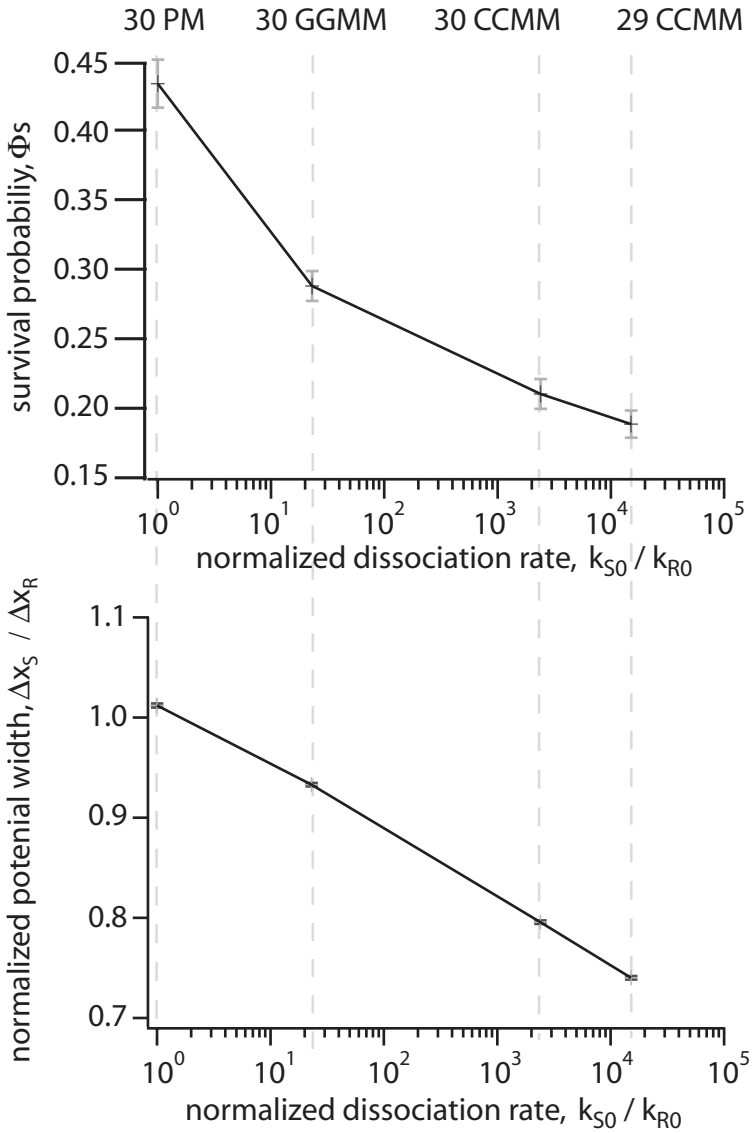

Neuert_figure5

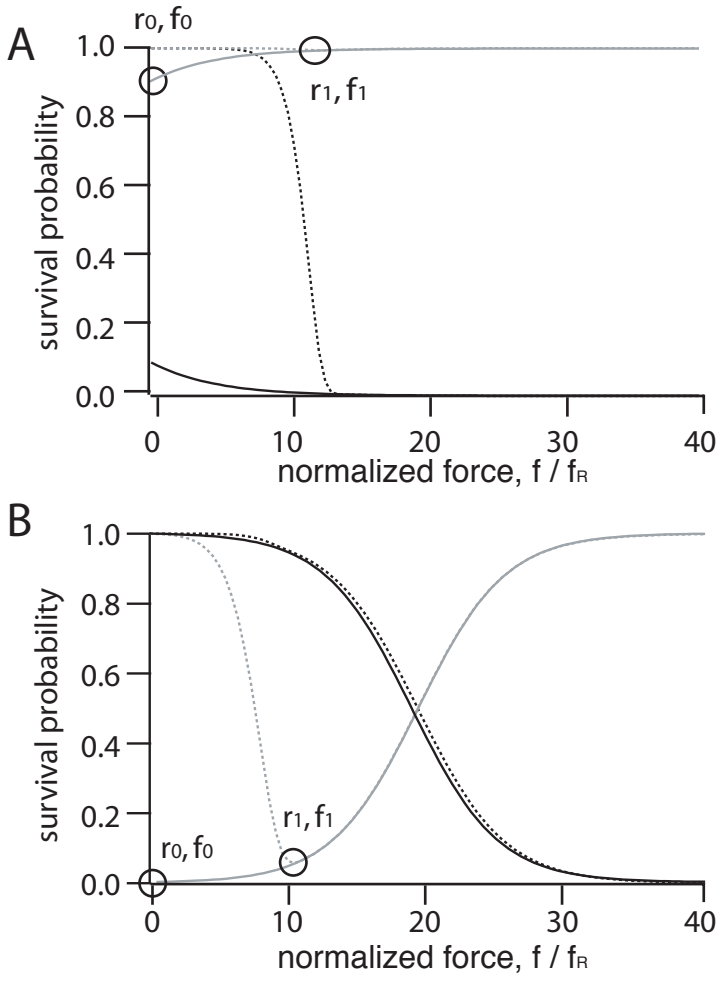

Neuert_figure6

P4) Dynamic force spectroscopy with a molecular balance

Christian Albrecht, Gregor Neuert, Robert A. Lugmaier, Hermann E. Gaub

European Biophysics Journal, 2007, **Submitted**

Dynamic force spectroscopy with a molecular balance

Christian H. Albrecht[#*], Gregor Neuert[+], Robert A. Lugmaier [#], Hermann E. Gaub [#]

Chair of applied physics, LMU-München, Amalienstrasse 54, D-80799 Munich

+ Massachusetts Institute of Technology, Department of Physics, 77 Massachusetts Ave., Cambridge, MA, 02139, USA

* to whom correspondence should be addressed: e-mail: christian.albrecht@physik.uni-muenchen.de

Abstract

Differential measurements, where two DNA duplexes are compared directly to each other in a balance like manner, have been demonstrated to be very sensitive in resolving small differences in rupture force. Here we extend this technique to *dynamic* differential force measurements, where the force balances are probed over a wide range of pulling speed in a single measurement by applying gradient fields. We quantify the gradients of the pulling velocities by reflection interference contrast microscopy and convert them into local force loading rates based on an elastic model. In parallel we measured the difference in bond rupture probability by fluorescence imaging which we correlate with the force loading rates. We discovered that at force loading rates above $9 \cdot 10^5$ pN/s, which were not accessible before, the unbinding of the two strands of DNA-Oligomers becomes orientation dependent.

Introduction

Due to their dominant role in immunity, signal transduction and drug binding, to mention a few, "receptor-ligand" associations are of general interest in the life sciences. Being studied for a long time in terms of their "energetic" properties only, those non-covalent interactions have meanwhile become an important subject of mechanical single molecule investigations with instruments like atomic force microscopes, biomolecular force probes and optical or magnetic traps. The first single molecule force experiments on receptor-ligand systems, which were carried out at constant pulling speed, revealed that even very stable receptor-ligand complexes could be overcome by pulling forces in the piconewton range in a reasonable time [1]. Later *dynamic* force spectroscopy was introduced when series of measurements on the same interaction were carried out at different pulling velocities. Compared to *"static"* measurements at constant velocity, those *dynamic* studies are suited to map the energy landscape at many points, thereby revealing kinetic unbinding barriers [2], [3], [4], [5].

We have recently introduced an alternative approach to measure molecular rupture forces, where two receptor ligand complexes are compared to each other differentially: the molecular force balance [6, 7]. In figure 1, a force balance consisting of two DNA oligonucleotide duplexes is depicted, having a reference bond (blue) and a sample bond (red) which are connected to each other and which are immobilized between two surfaces in close contact. When the surfaces are pulled apart from each other, strain builds up in the balance until one of the two bonds ruptures. A fluorescent label (green) that is attached to the middle part of the balance either ends up on the upper or the lower surface, depending on whether the rupture force of the reference bond F_R is higher than the rupture force of the sample bond F_S, or vice versa. By reading out the distribution of

the label between the surfaces it is possible to determine the strength of the bonds relative to each other.

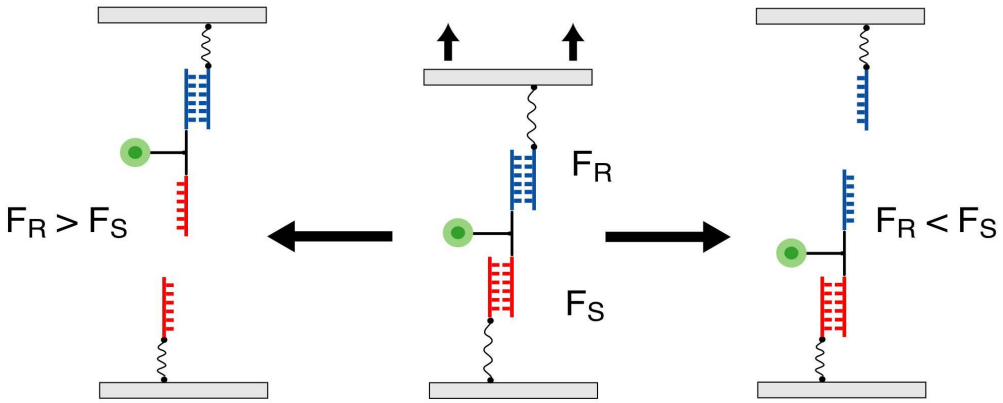

Figure 1: Differential force measurement with a molecular balance. A force balance consisting of a reference duplex (blue) linked to a sample duplex (red) is immobilized and probed between to surfaces. The fluorescent label attached to the middle part of the balance either ends up on the upper surface, when the unbinding force of the reference duplex is stronger, or on the bottom, when the unbinding force of the reference duplex is lower than that of the sample duplex.

According to this concept we have achieved to discriminate between different kinds of single base pair mismatches in 30 bp DNA duplexes [7], [8], thereby demonstrating the outstanding sensitivity of the differential approach. However those results have been derived from *"static"* measurements were the pulling velocity was relatively low and constant, leaving the interesting regime of high loading rates unexplored. Here we report for the first time on *dynamic* differential force measurements, where the separation velocity at the stamp slide interface has a marked gradient, giving rise to a large gradient of loading rates in a single measurement. Moreover with the dynamic force balance method very high loading rates of 10^6 pN/s are realized, a regime that is hardly accessible by conventional techniques.

Surprisingly an asymmetry of the force balance became evident in this high range of loading rates that was completely unexpected. We show that the asymmetric effect

arises when a critical loading rate of ~$9 \cdot 10^5$ pN/s is reached at ~65 pN of rupture force. Moreover we show that the asymmetry is caused by a mechanism which formally results in an abrupt change of the potential widths of the reference duplex (x_R) and the sample duplex (x_S) relatively to each other at a critical loading rate. The results are discussed by taking reference to the B-S transition of DNA [9], [10] and to kinetic effects that have been measured for the biotin-streptavidin complex [5].

The differential force assay

In contrast to force probe techniques, where individual molecules are loaded by means of a microscopic transducer, the differential measurement is carried out on a macroscopic number of balances (~10^9) simultaneously by probing the molecular bridges that have formed over a large area of ~1mm^2 between a silicone stamp and a glass slide. Assembly of the balances starts with immobilization of amino-modified oligonucleotides on an aldehyde activated glass slide. Oligonucleotides labelled with Cy3™-fluorophore then are hybridized to the amino-oligonucleotides thereby forming a sample duplex. Subsequently oligonucleotides labelled with biotin at the 5'-terminus are hybridized to the Cy3-oligonucleotide thereby forming a reference duplex. The structure of the balance used for this study is depicted in Table 1.

oligo dir.	sequence
3'-5'	←NH2-10t-CTGCAGGAATTCGATATCAAGCTTATCGAT
5'-3'	GACGTCCTTAAGCTATAGTTCGAATAGCTAc-8t-Cy3-8t-cATCGATAAGCTTGATATCGAATTCCTGCAG
3'-5'	TAGCTATTCGAACTATAGCTTAAGGACGTC-10t-Bio->

Table 1: Molecular balance drawn in horizontal orientation. Left = slide, right = stamp. Sample duplex (red) and reference duplex (blue). Labels: NH2 = amino; Cy3 = Cyanin-3 fluor; Bio = biotin; 8t = poly-t-spacer. The force is applied along the arrows (Oligonucleotides were purchased from IBA GmbH,Goettingen, Germany)

Coupling of the balances to the silicone stamp is facilitated by streptavidin biotin interaction as depicted in figure 2. The silicone stamp comprises sixteen protruding pads, each having a diameter of 1.1 mm. Each pad is brought into contact with a spot of balances, on the slide (figure 2 a). On top each pad is structured by a micropattern of rectangular contact areas, which are elevated by 5µm (figure 2b). When the stamp is approached to the slide, only those elevated rectangular areas make contact to the slide and will couple to the balances (figure 2c). The trenches in between serve as drainage channels. After coupling, the stamp is pulled apart from the slide, by means of a piezo actuator, thereby probing and rupturing the balances. This results in a distribution of the Cy3-label between stamp and slide that is read out by a laser scanner (figure 2d) (see [7] for details).

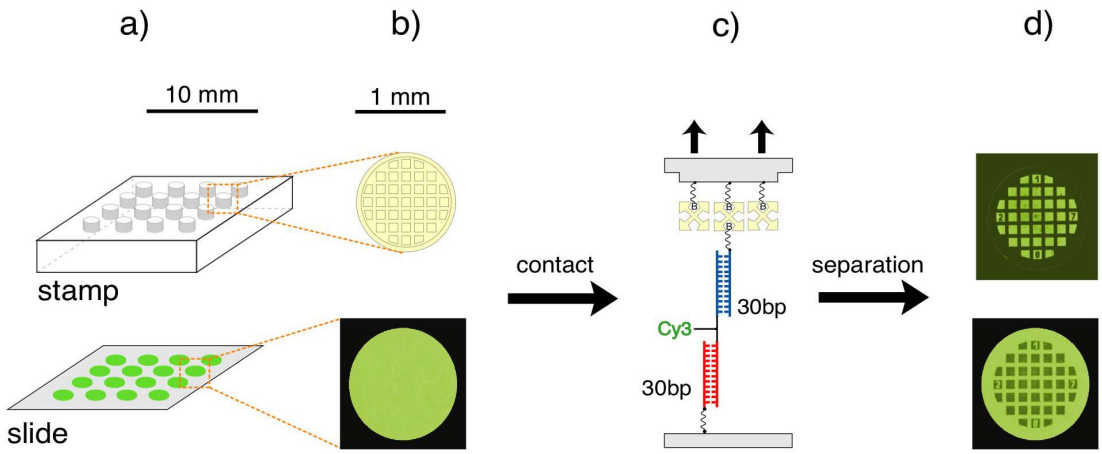

Figure 2: Contact and separation stamp and slide: a) Scheme of a silicone stamp having 16 contact pads and a glass slide having 16 spots of force balances. b) A single pad with a microstructure of elevated rectangular contact areas covered with streptavidin (yellow) and fluorescence image of a single spot (green). c) Coupling of a single biotinylated force balance to streptavidin on the stamp. d) Fluorescence image of stamp and spot after separation: The dark rectangular prints in the spot indicate where contact has been established and balances have coupled to the stamp.

In order to correct for those balances that have not coupled to the stamp, soluble streptavidin-AlexaFluor647-conjugate is bound to the free biotin residues on the slide

and the signal is read out again by the scanner. The output of a differential force experiment, the survival probability of the sample duplex Φ_S, is calculated from four input parameters, that are extracted from the two fluorescence scans as depicted in figure 3. The remained Cy3-intensity ($Cy3_{REM}$) is extracted from the rectangular prints in the green scan, where contact has been established between stamp and slide. $Cy3_{REM}$ corresponds to balances that have been probed and ruptured at the reference duplex as well as to balances which have not been coupled to the stamp, thereby causing an offset. The start Cy3-intensity ($Cy3_{START}$) that corresponds to the initial density of balances immobilized on the slide is extracted from the grid pattern in the green scan. If the coupling efficiency of the balances would be 100 %, then the survival probability of the sample bond simply would be $\Phi_S = Cy3_{REM} / Cy3_{START}$. However both Cy3-variables first have to be corrected for the offset of balances that have not been coupled. Therefore the red scans is analyzed in terms of the remained biotin density ($AF647_{REM}$) and the start biotin density ($AF647_{START}$) (figure 3). The degree of coupling then corresponds to $AF647_{REM} / AF647_{START}$ and the offset can be calculated according to:

$$Cy3_{offset} = Cy3_{START} \cdot \frac{AF647_{REM}}{AF647_{START}}$$

The survival probability of the sample duplex Φ_S is determined from the offset corrected $Cy3_{REM}$ normalized to the offset corrected $Cy3_{START}$ according to:

$$\Phi s = \frac{Cy3_{REM} - Cy3_{offset}}{Cy3_{START} - Cy3_{offset}}$$

Correction for coupling efficiency and normalization to $Cy3_{START}$ was performed for all experimental data. For images in figure 5 an average $Cy3_{offset}$ was determined from all

contact areas. For the plots in figure 6, 7 and 8 the correction was calculated separately for the referring contact area.

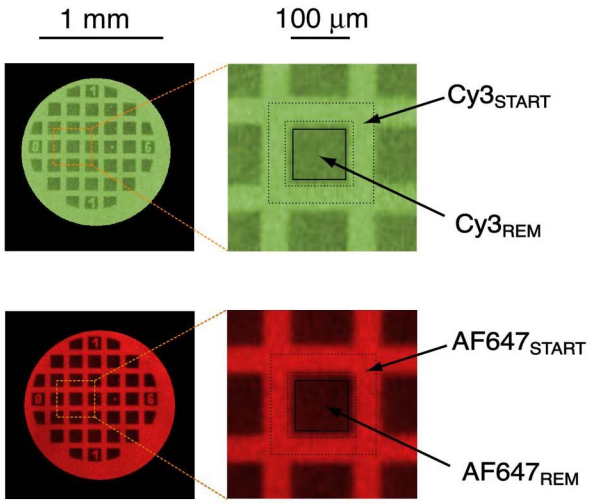

Figure 3: Two images of the same spot after separation. Dark squares correspond to the contact area where the balances have ruptured. Scans for Cy3 (green) and for AF647-streptavidin (red) which was bound to free biotins after scanning for Cy3. $Cy3_{START}$ intensity and $AF647_{START}$ intensity are derived from the area surrounded by the dashed lines. $Cy3_{REM}$ intensity and $AF647_{REM}$ intensity are derived from the area surrounded by the solid lines.

Dynamic differential force spectroscopy

Due to the accumulative binding force of ~10^9 molecular balances at one contact area, a quite strong interaction is built up between stamp and slide. The stamp therefore, is not separated at once over the whole contact area, but deforms elastically and detaches in a propagating cleft from the rigid slide when pulled apart by the piezo actuator. This separation process commences at the edges of the rectangular contact areas, and moves forward until complete separation (figure 4a).

As long as the stamp is pulled apart by low velocities up to ~50 nm/s, the lateral speed of the cleft propagation is almost constant over all contact areas of the stamp. However at elevated piezo speeds, detachment is not keeping pace with the movement in z-

direction and strain is build up in the stamp. This tension gives rise to a non-linear separation behaviour, where detachment occurs relatively slow at the edges of the contact areas but accelerates markedly towards the points, where contact remains longest. As a consequence a steep velocity gradient and a broad range of loading rates is accomplished over a single contact area. In fact originally it was not our intention to separate the surfaces with a non-linear characteristic, but then we decided to make use of it for *dynamic* measurements and analyzed the velocity gradient by means of reflection interference contrast microscopy (RICM) comparable to the approach in [11]. For this purpose we mounted the contact device on an inverted microscope (Axiomat, Zeiss, Goettingen) as depicted in figure 4a. The contact interface of stamp and slide was illuminated by means of a xenon arc lamp, a neutral 50/50 beamsplitter and a HC bandpass 628/40 nm excitation filter (AHF Analysentechnik, Tuebingen) through a 10x Fluar (0.5 NA) objective (Zeiss, Goettingen). Separation was filmed at 500 frames/s with a pco1200hs high-speed camera (PCO, Kehlheim, Germany). A single RICM frame of the whole stamp pad is depicted in figure 4a, individual contact areas are shown in figure 4b.

The effective separation velocities were derived by converting the lateral movement of the first and second interference maximum into separation distances in z-direction according to the method described in [12] and [13], under the assumption that the geometry of the separation cleft (figure 4a) is wedge-shaped (which was corroborated by finite element simulations not shown here). In figure 4b four frames from a high speed RICM movie are shown. The first two of them, which are separated by an interval of 4 ms, were analyzed along a region of interest with a width of three pixels (white line), by plotting an averaged intensity profile over the position on the slide.

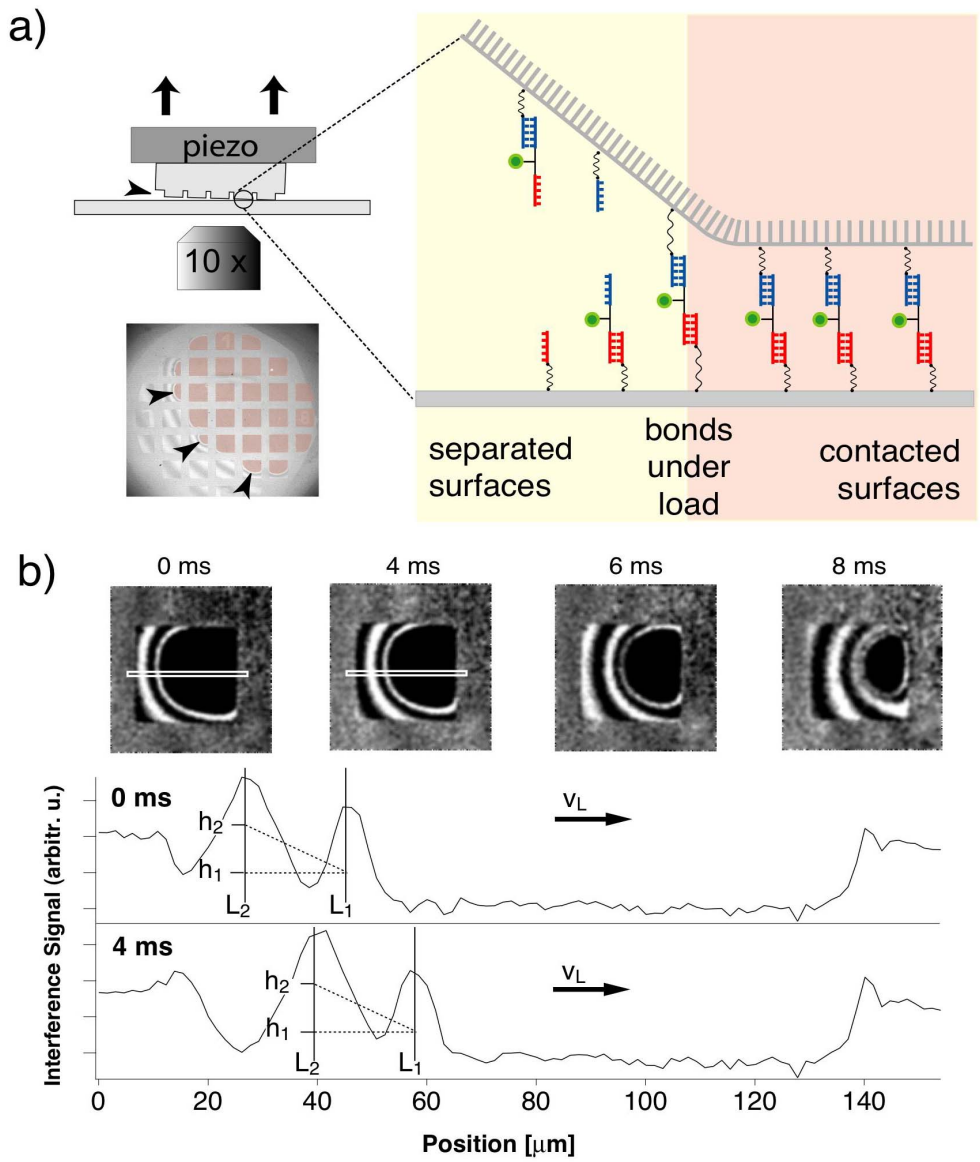

Figure 4: a) Schematics and interference micrograph of slide-stamp separation driven by piezo movement. Slide-stamp contact areas (light red) are separated at the edge of the propagating cleft at which the balances are loaded and ruptured. The separation direction is indicated by black arrowheads. b) RICM profile at the time t1 = 0 ms (upper section) and at the time t2 = 4 ms (lower section) showing the first and second interference maximum at the positions L1 and L2. Each profile is measured along the white marking, which is perpendicular to the direction of movement of the bright interference rings (images on the left side). The two maxima move with a lateral velocity $v_L = 3.1 \cdot 10^3$ μm/s to the left. This corresponds to a stamp – slide separation velocity $v_Z = 40$ μm/s (calculation see text). The heights of the stamp over the slide are referred as h_1 and h_2 for the first and second maximum.

The first and second maximum next to the contact area were fitted with a Gaussian curve in order to determine their lateral position. The lateral velocity v_L of the peeling

process was determined from a diagram where the first maxima were plotted as a function of position and time. From the lateral distances (L_1 and L_2) and the heights of the interference maxima (which are $h_1 = 124 \pm 3$ nm and $h_2 = 362 \pm 5$ nm at a wavelength of 628 nm) a conversion factor k was derived which links the lateral peeling speed into a z-directional separation velocity via $v_z = k \cdot v_L$ with $k = (h_2-h_1)/(L_2-L_1)$.

Results and Discussion

A force balance of perfect symmetry is not easy to accomplish, since different sequences have to be used for the reference and the sample duplex in order to avoid cross hybridization when the balance is assembled. Unequal sequences however will always result in some difference in Gibb's free energy ($\Delta G_R \neq \Delta G_S$). Nevertheless, a satisfactory symmetry could be achieved when the sequences of the two duplexes are reverse to each other like those depicted in Table 1, which correspond to Gibb's free energy differences of $\Delta G_R = -46.2$ and $\Delta G_S = -45.0\ k_BT$ for the reference- and the sample duplex respectively, as calculated with the nearest neighbour algorithm [14], [15]. The same balance was previously used to determine the influence of various mismatches in the sample duplex [8]. However, with a difference, which we initially assumed to have little influence: the Cy3-label was attached at the 3'-terminus of the middle oligonucleotide for the latter study, unlike here, where the label was introduced centrally between the duplexes. This "minor" alteration however resulted in a noteworthy shift of the survival probability Φ_S. Indeed it was reproduced many times that the survival probability Φ_S equals ~0.4 for the 3'-Cy3 balance whereas the new balance shows a Φ_S of ~0.6. Obviously the reference duplex was stabilized by the label nearby, a notion that is supported by studies on the stacking interaction of Cy3 at the end of a helix [16].

Another kind of asymmetry was discovered when the force balance in table 1 was probed at different piezo pulling velocities. While for low velocities between 0.02 µm/s and ~1 µm/s constant survival probabilities Φ_S ~0.63 were observed, the situation was very different for higher velocities: In figure 5a the stamp was pulled apart by a very low velocity of 0.02 µm/s. The corresponding graph (measured along the white area in the micrograph) shows normalized intensities between ~0.63 and 1. High values approaching 1 correlate with the grid structure in the micrograph, while the lower values originate from the rectangular contact area and correspond to the survival probability of the sample duplex Φ_S. Apart from some noise the Φ_S-profile is relatively flat. For the spot in figure 5b where the stamp was removed thousand times faster at 20 µm/s, the situation is different. Although the graph again shows values of ~1 for the grid, large irregularities are present throughout the contact area where Φ_S increases abruptly and culminates in peaks of about 0.9, as highlighted by grey shadows in the plot of figure 5b.

As described in the methods section, contacting and separation of stamp and slide was monitored by reflection interference contrast microscopy (RICM). Inspection of the interference image by eye soon led to the presumption, that the pulling velocity is not uniform over the whole contact area, when the stamp is moved faster than 50 nm/s. Rather a non-linear disjoining was observed, starting with slow separation at the edges of the squares and then accelerating significantly towards the points where the contact maintained longest. This led to the speculation, that Φ_S maxima and minima in image figure 5b might be caused by locally enhanced separation velocities. Therefore high-speed RICM movies were taken from the separation process in order to quantify the local separation velocities. Along a section (white arrow) that crosses the non-linear

effect, the velocity gradient was determined and plotted together with the normalized fluorescence (green line) as a function of the position on the slide (see Fig 6).

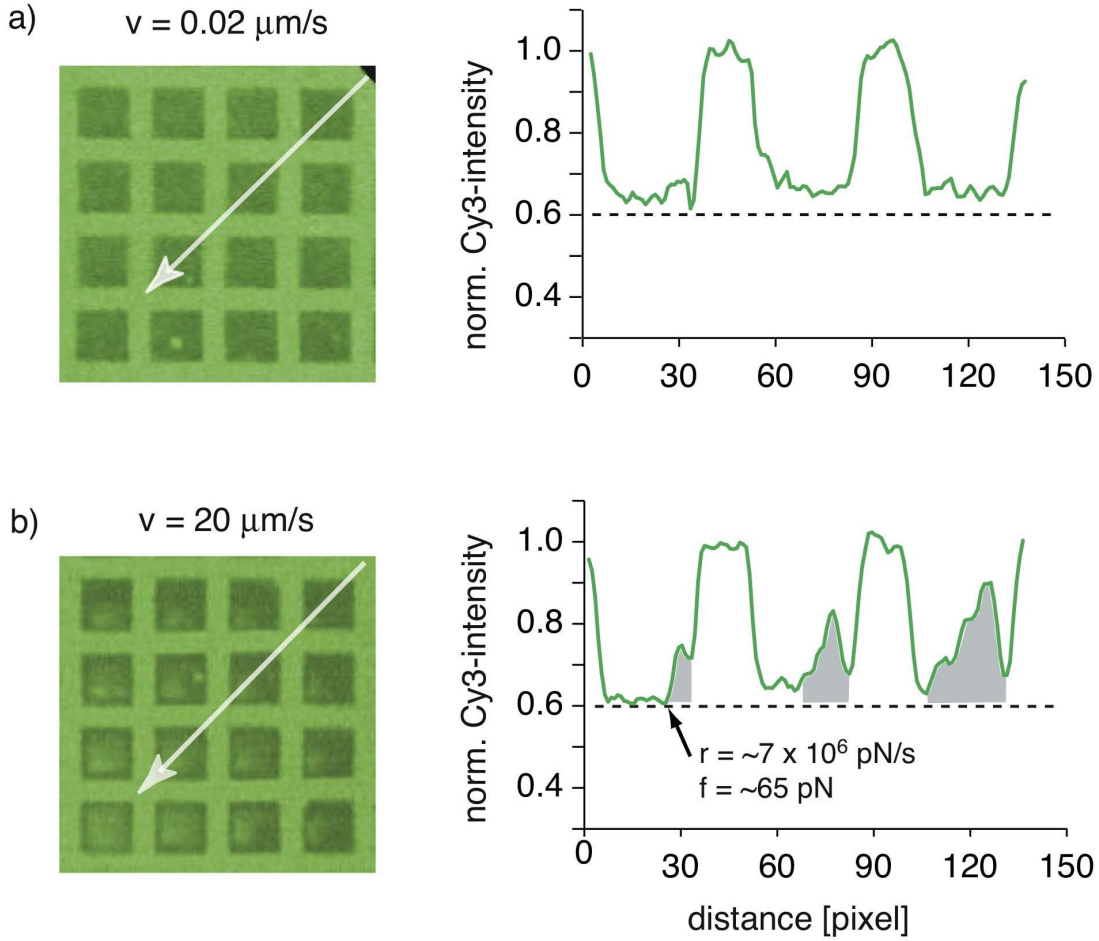

Figure 5: Normalized Cy3-intensity images where the rectangular contact areas correspond to Φ_S (survival probability of the sample duplex). White selections in the images are plotted as normalized intensity over distance. Grey areas in the diagram are specifying the non-linear effect. (a) Molecular force balance probed at 0.02 μm/s: The curve sections between the peaks (Φ_S) are relatively flat. (b) Molecular force balance probed at 20 μm/s: Φ_S is increasing steeply in some contact areas. For the onset of the peaks loading rate and rupture force was calculated (black arrow). Data was smoothed by a median filter.

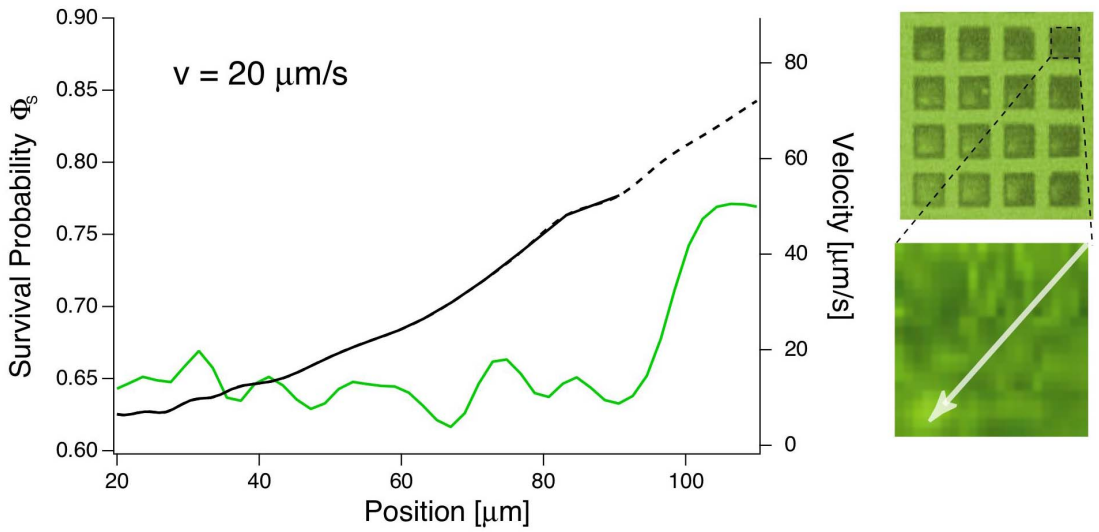

Figure 6: Upper right contact area of experiment in 5b. Survival probability of the sample duplex Φ_S was plotted over position on the slide (green line). Velocity was determined as described above (black solid line; dotted line: extrapolated).

However, after the point in the curve where the fluorescence intensity increases sharply, the first and second interference maximum around the contacted area started to merge and became indistinguishable. This effect indicates, that the slope of the stamp reaches the limit of the vertical resolution at this point, which can be estimated from the difference in height between the first and the second maximum (238 nm) divided by the limit of the lateral resolution (2380 nm), which corresponds to two pixel of the camera. The resolution limit of the slope therefore is tan 0,1 = 5,7°. Since velocity and loading rate could not be determined after the non-linear effect, they were extrapolated after that point (dotted black line).

In general receptor-ligand-systems are characterized by a rupture force that occurs at a certain force loading rate. Those parameters are accessible with AFM- or other force probe techniques, when force is plotted over time. In our differential assay however we can not derive rupture force and the loading rate directly, since the fluorescence distribution and the separation velocity are the only measured parameters. Nevertheless, since in this case the receptor-ligand-system was well characterized in terms of potential

width and off-rate with AFM before [3], it is possible to convert the velocity curve in figure 6 into loading rates and rupture forces. This was done by Monte Carlo simulations as described in [17], where the Bell-Evans-theory [18] and a freely jointed chain model was employed. The force loading rate and the rupture force were calculated under the assumption, that the polymeric PEG-linker of 68 monomers, which connects the balances to the stamp, accounts fully for the overall spring constant of the system and that the spring constant of the silicone is negligible (we used a spring constant of 1000 pN/s for the transducer). To describe the properties of the balance, we assumed a single DNA duplex of 30 bp which corresponds to a binding width of 2.8 nm according to [3] and to a k_{off} = 2.8e-14 s^{-1} . The off-rate was calculated according to $K_D = \frac{k_{off}}{k_{on}} = e^{\frac{\Delta G}{k_B T}} = e^{\frac{\Delta G_{off} - \Delta G_{on}}{k_B T}}$ from the free Gibb's energy differences of the DNA duplex and under the assumption that the association rate is diffusion limited and equals $k_{on} = 10^6 M^{-1} s^{-1}$ [19]. Loading rate and rupture force then were plotted together with the survival probability over the distance on the slide in figure 7 and 8:

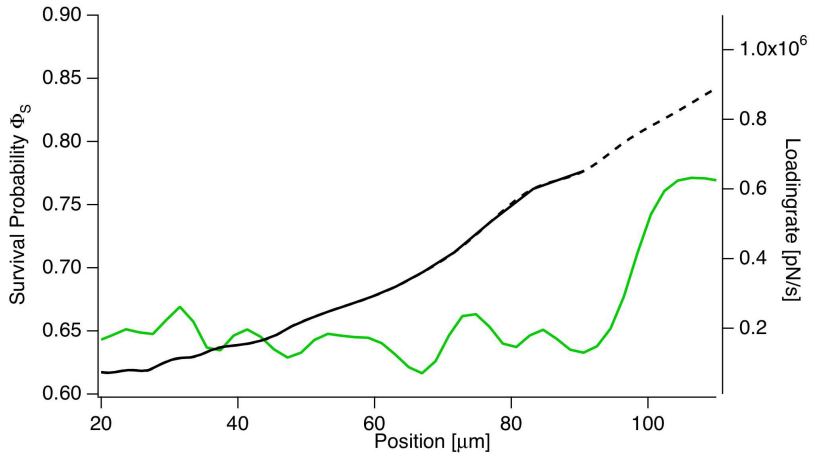

Figure 7: Survival probability Φ_S curve of figure 6 plotted together with loading rates which were calculated from the velocities in figure 6 (black solid line; dotted line: extrapolated).

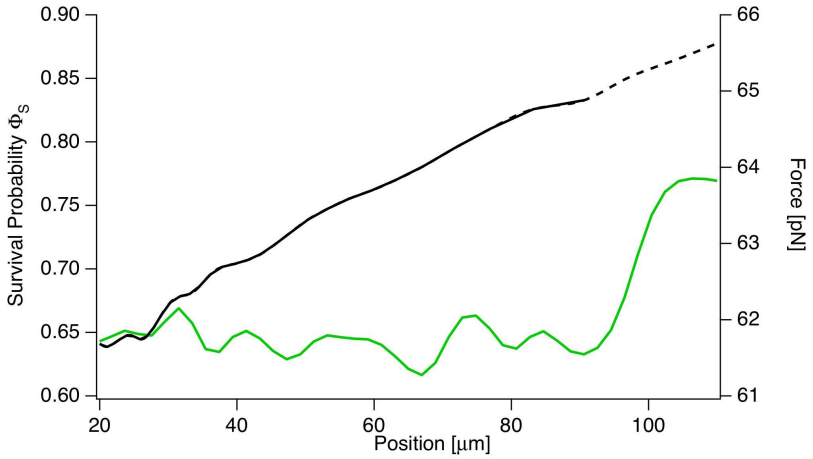

Figure 8: Measured survival probability Φ_S of the sample duplex (green solid line) against the rupture force F (black line) that was calculated from the velocity curve in figure 6 (black solid line; dotted line: extrapolated).

While for the curve shown in figure 5 and figure 6 a loading rate of $7 \cdot 10^5$ pN/s and a rupture force of ~65 pN was determined at the onset of the non-linear effect the average value was slightly higher. The average values derived from six curves each from a different contact area of the same spot are: $9.46 \cdot 10^5 \pm 1.6 \cdot 10^5$ pN/s of loading rate and 65.4 ± 0.3 pN of rupture force at 0.64 ± 0.01 of survival probability.

In order to explain the non-linear effect in figure 5b, one has to bear in mind, that it occurs due to a difference between the upper and the lower duplex of the balance and therefore is a relative property of both bonds, not a property of a single bond alone. The ramifications of asymmetries between sample- and reference-duplex balance have been modelled recently by means of coupled differential rate equations [8]. It was pointed out, that asymmetry arising from differences in ΔG_{off} will change the survival property of the sample bond Φ_S by a value that is independent of the applied loading rate. A difference in potential width between the two duplexes Δx_{RS} however will affect Φ_S increasingly when rising loading rates are applied to the balance.

Consequently the non-linear effect observed in figure 5 and could be formally ascribed to a difference in potential width, where the width of the reference duplex is broader than that of sample duplex ($x_R > x_S$), a notion that is supported by the fact, that $\Delta G_R < \Delta G_S$ and by the finding that ΔG and Δx of a short DNA duplex are directly proportional [8]. Therefore we have estimated the range of loading rate, that would be necessary to give rise to an increase of Φ_S from 0.64 to 0.9 for the variables that were used to fit the Φ_S curve in figure 6, where $x_R = 2.8$ nm, $x_S = 2.665$ nm, $\Delta G_R = -46.2\ k_BT$ and $\Delta G_S = -45.0\ k_BT$. It however turned out that it would require a rise in the force loading rate of about 20 orders of magnitude for the non-linear effect to be observed. Such an extreme gradient in force load is far beyond any realistic scenario and can therefore be exclude as possible cause.

As mentioned above, we were not able to determine velocities from the RICM movies for those positions on the slide, where the non linear effect in Φ_S has been observed, since no concentric RICM maxima or minima could be resolved around the area of contact. This effect very likely is due to a deformation of the stamp which results in a profile too steep to be resolved by RICM. A deformation like this however would also be associated with a much steeper increase in velocity compared to that we have indicated by the dashed line in figure 6. Nevertheless even at a ten or twenty times higher velocity no significant effect on Φ_S is to be expected as evidenced by the estimation given above.

Furthermore some other observation from experiments, where the same force balances have been stabilized by intercalating molecules may explain, why the stamp becomes deformed exactly at the point where Φ_S becomes non-linear as well: Only when the intercalator is present, such stamp deformations are already observed when pulled at a

rather low velocity of 200 nm/s, indicating that much higher forces have to be overcome to rupture the balances (publication in preparation). We therefore can assume that for the experiments presented here the overall rupture forces of the balances are increasing at the non-linear Φ_S effect, which then gives rise to a deformation of the stamp.

Interestingly all this happens at a rupture force of 65 pN (figure 6), a value that is well known from the overstretching of long polymeric DNA [9], [10], [20]. However we can not think of a plausible scenario where the sample duplex is getting more stable relative to the reference duplex due to a mechanism just based on B-S-overstretching at 65 pN. We therefore assume that the non-linear effect is due to a relative change in binding width between both duplexes, where x_S suddenly becomes smaller than x_R due to a unknown mechanism that is triggered at a critical loading rate of $\sim 9 \cdot 10^5$ pN/s and accompanied by a significant jump in rupture force of the whole balance.

Loading rate dependent effects like this have been reported before, especially for the complex of biotin and avidin but also for antibody interactions [5, 21]. For avidin it was proposed that inner kinetic barriers become dominant for the unbinding process when the outer barrier is lowered due to the applied force. Moreover a correlation of those barriers to structural features of the binding pocket have been proposed based on molecular dynamics simulations [22]. For DNA however we currently do not see a relation between structure and the observed kinetic barrier.

The fact that this kinetic barrier has not been discovered so far may have two reasons. First, the loading rates achieved in the differential test are at least two orders of magnitude higher than those employed in single molecule studies like AFM, which are in the range between 30 and 6000 pN/s [3], [23] and second, the change of binding

width difference between the two duplexes might be very small and therefore not easy to detect.

Conclusion

Our observation and the fact of an ongoing debate about the structural nature of the B-S-transition [24, 25] shows that the mechanics of forced rupture of DNA obviously is not entirely understood, despite having been investigated thoroughly. Experiments with different alterations of the force balance, which are suited to shed more light on both issues are currently carried out at our lab.

Acknowledgement

We thank Dieter Braun for hardware support. Hauke Clausen-Schaumann for helpful discussions. Ferdinand Kuehner and Steffen Mihatsch for providing the software to analyze the measured velocity values. Dominik Ho for simulations and reviewing the manuscript.

References

1. Florin, E.L., V.T. Moy, and H.E. Gaub, *Adhesion forces between individual ligand-receptor pairs.* Science, 1994. **264**(5157): p. 415-7.
2. Schwesinger, F., et al., *Unbinding forces of single antibody-antigen complexes correlate with their thermal dissociation rates.* Proc Natl Acad Sci U S A, 2000. **97**(18): p. 9972-7.
3. Strunz, T., et al., *Dynamic force spectroscopy of single DNA molecules.* Proc Natl Acad Sci U S A, 1999. **96**(20): p. 11277-82.
4. Berquand, A., et al., *Antigen binding forces of single antilysozyme Fv fragments explored by atomic force microscopy.* Langmuir, 2005. **21**(12): p. 5517-23.
5. Merkel, R., et al., *Energy landscapes of receptor-ligand bonds explored with dynamic force spectroscopy.* Nature, 1999. **397**(6714): p. 50-3.
6. Albrecht, C., et al., *DNA: a programmable force sensor.* Science, 2003. **301**(5631): p. 367-70.
7. Albrecht, C., H. Clausen-Schaumann, and H. Gaub, *Differential analysis of biomolecular rupture forces.* Journal of Physics: Condensed Matter, 2006. **18**: p. 1-19.
8. Neuert, G., C. Albrecht, and H.E. Gaub, *Predicting the rupture probabilities of molecular bonds in series.* Biophysical Journal, 2006. **submitted**.

9. Cluzel, P., et al., *DNA: an extensible molecule.* Science, 1996. **271**(5250): p. 792-4.
10. Smith, S.B., Y. Cui, and C. Bustamante, *Overstretching B-DNA: the elastic response of individual double-stranded and single-stranded DNA molecules.* Science, 1996. **271**(5250): p. 795-9.
11. Leckband, D.I., J, *Intermolecular forces in biology.* Quarterly Reviews of Biophysics, 2001. **34**(2): p. 105-267.
12. Wiegand, G., K. Neumaier, and E. Sackmann, *Microinterferometry: three-dimensional reconstruction of surface microtopography for thin-film and wetting studies by refelection interference contrast microscopy (RICM).* Applied Optics, 1998. **37**(29): p. 6892-6905.
13. Rädler, J. and E. Sackmann, *Imaging optical thickness and separation distances of phospholipid vesicles at solid surfaces.* Journal de Physique II, 1993. **3**: p. 727-748.
14. SantaLucia, J., Jr., *A unified view of polymer, dumbbell, and oligonucleotide DNA nearest-neighbor thermodynamics.* Proc Natl Acad Sci U S A, 1998. **95**(4): p. 1460.
15. *http://jsl1.chem.wayne.edu/Hyther/hythermenu.html*.
16. Norman, D.G., et al., *Location of cyanine-3 on double-stranded DNA: importance for fluorescence resonance energy transfer studies.* Biochemistry, 2000. **39**(21): p. 6317-24.
17. Friedsam, C., et al., *Dynamic single-molecule force spectroscopy: bond rupture analysis with variable spacer length.* Journal of Physics-Condensed Matter, 2003. **15**(18): p. S1709-S1723.
18. Evans, E. and K. Ritchie, *Dynamic strength of molecular adhesion bonds.* Biophys J, 1997. **72**(4): p. 1541-55.
19. Northrup, S.H. and H.P. Erickson, *Kinetics of protei-protein association explained by Brownian dynamics computer simulation.* Proc Natl Acad Sci U S A, 1992. **89**: p. 3338-3342.
20. Clausen-Schaumann, H., et al., *Mechanical stability of single DNA molecules.* Biophys J, 2000. **78**(4): p. 1997-2007.
21. Neuert, G., et al., *Dynamic force spectroscopy of the digoxigenin-antibody complex.* FEBS Lett, 2006. **580**(2): p. 505-9.
22. Grubmuller, H., B. Heymann, and P. Tavan, *Ligand binding: molecular mechanics calculation of the streptavidin-biotin rupture force.* Science, 1996. **271**(5251): p. 997-9.
23. Lang, M.J., et al., *Simultaneous, coincident optical trapping and single-molecule fluorescence.* Nat Methods, 2004. **1**(2): p. 133-9.
24. Lebrun, A. and R. Lavery, *Modelling extreme stretching of DNA.* Nucleic Acids Res, 1996. **24**(12): p. 2260-7.
25. Rouzina, I. and V.A. Bloomfield, *Force-induced melting of the DNA double helix 1. Thermodynamic analysis.* Biophys J, 2001. **80**(2): p. 882-93.

P5) dsDNA unbinds under force dependent pathways

Christian Albrecht, Gregor Neuert, Robert A. Lugmaier, Hermann E. Gaub

Nucleic Acids Research, 2007, **Submitted**

dsDNA unbinds under force in rate dependent pathways

Christian H. Albrecht[*#], Gregor Neuert[+], Robert A. Lugmaier[#], Hermann E. Gaub[#]

Center for Nanoscience and chair for applied physics, LMU-München, Amalienstrasse 54, D- 80799 Munich

+ Massachusetts Institute of Technology, Department of Physics, 77 Massachusetts Ave., Cambridge, MA, 02139, USA

* to whom correspondence should be addressed: e-mail: calidris@gmx.com

Abstract

Strand separation of double stranded DNA (dsDNA) is a crucial step for essential cellular processes like recombination and transcription. The forces necessary to open the DNA helix will depend heavily on geometry and speed by which molecular machines are acting on the double strand and thus on the degree by which thermal fluctuations are assisting the process. By means of a molecular force balance we have analyzed the impact of different pulling directions and different force loading rates on the unbinding process of short dsDNA. We discovered that the unbinding reaction of DNA proceeds over different transition states, which depend on the loading rate. We show that at low loading rates, which are comparable to those applied in conventional single molecule experiments, unbinding is dominated by thermal fluctuations, creating bubbles which lower the force required to separate the two strands. Predominantly the height of the barriers and to a lower extend the orientational details determine the forces that are involved here. At higher loading rates however, the asymmetry of the phosphoribose backbone becomes important. We find a marked difference in rupture force for pulling the duplex in 3'-3'-direction compared to 5'-5'-direction indicating different unbinding pathways. The transition states in this range resemble conformations with intact base pairing ("S-forms"), which earlier have been proposed for the B-S-transition. A mechanism is proposed, where the unbinding switches from a quasi-equilibrium to a kinetic process, when the loading rate exceeds the relaxation time of DNA melting bubbles. This model is discussed in conjunction with dynamic force measurements on protein receptor ligand systems. Moreover we give evidence for a loading range where the rupture force of both 5'-5'- and 3'-3'-pulling direction exceeds that of the biotin-streptavidin complex.

Introduction

Conversion of double stranded DNA (dsDNA) into single strands is crucial for essential cellular processes like recombination, replication and transcription. According to their physiological function, molecular machines have evolved different mechanisms to apply the forces necessary to denature the double strand. In RecA assisted recombination for example, the helix is enclosed in a narrow tunnel, where it is stretched, unwound and subsequently denatured [1]. In contrast to that, RNA polymerase forms a transcription bubble that moves along the DNA template while RNA is polymerized. As for any other molecular machine, two basic mechanisms have been discussed in terms of the opening of DNA during transcription: the "powerstroke", where the hydrolysis of the triphosphates is efficiently converted into mechanical work and the "brownian ratchet" where the process mainly is powered by thermal noise, while chemical energy predominantly is used to rectify those fluctuations [2]. Interestingly DNA separation by means of force probe instruments has been discussed in a quite similar way. Again one discrete "mechanical" and one fuzzy "brownian" model has been put forward to describe the unbinding reaction however without definitive answers. Here we present a study, where we have probed short dsDNA at different ends, at different speed by means of a molecular force balance. Thereby unknown mechanical properties of the DNA-helix have been revealed which provide new insights into the unbinding mechanism of DNA.

A molecular force balance measures differences in binding forces by direct comparison of a sample-bond (red) to a reference-bond (blue) (Fig. 1a). A large number of such balances are attached at their opposing ends between a glass slide and a silicone stamp and probed in parallel. Upon separation of the stamp and the slide (Fig. 1b) the polymeric spacers are gradually stretched and the force builds up in the balances until

either the reference- or the sample-bond fails, depending on which one has the lower rupture force. As a consequence, the fluorescent label attached to the middle part of the balances will afterwards be found either on the stamp or on the glass surface. The difference in rupture force can thus be quantified by measuring the fluorescence on both sides and provides the survival probability Φ_S of the sample bond [3, 4]. Due to the high sensitivity of this differential measurement principle it was possible to detect minute differences in binding force as demonstrated for the discrimination between different kinds of single mismatches in 30 bp DNA [4], [5].

Single molecule force spectroscopy studies have revealed that only moderate forces in the piconewton range are required to disrupt receptor-ligand complexes like biotin-streptavidin or to separate the strands in dsDNA, as long as only moderate loading rates are applied to the bond because thermal fluctuations contribute to the unbinding reaction [6]. Accordingly a linear correlation between the logarithm of the loading-rate and the rupture-force has been measured for the unbinding of different short DNA duplexes [7]. However, recently we have demonstrated by means of a molecular force balance that short dsDNA shows a non-linear force response when a critical loading rate of $\sim 8 \cdot 10^5$ is exceeded indicating a kinetic barrier of unbinding [8].

Here we show that the non-linear effect reported previously is caused by an asymmetry between 5'-5' and 3'-3' pulling direction, that becomes significant when DNA is probed at rates higher than the relaxation kinetics of internal fluctuations. Obviously a kinetic regime is reached at high loading rates where mechanics becomes dominant over thermal fluctuations and the 5'-3' asymmetry of the helix becomes mechanically tangible.

This notion interestingly also could reconcile two opposing models which have been put forward for the transition state of DNA unbinding and overstretching: According to the "force induced melting" hypothesis, the B-S-transition is characterized by an opening of base pairs with the effect of partial unwinding and extension of the helix in order to compensate for the strain [9-11]. In contrast to this so-called "S-form", conformations with intact base pairing but steeply inclined nucleotides were suggested to represent the transition state. Thereby a ribbon-like unwound and a fiber-like "inwound" conformation have been proposed for pulling at the 3'-3'- and 5'-5'- ends respectively [12, 13], which could account for the asymmetry revealed by our measurements.

Consequently we argue that both hypothesis, "force induced melting" and "S-forms", are relevant for unbinding of short dsDNA depending on the actual loading rate. We propose that the unbinding mechanism switches from a quasi equilibrium reaction based on melting bubbles to a kinetic regime, where mechanics are dominant and stretched conformation with essentially intact base pairing account for the transition state, once a critical loading rate is exceeded.

The results are discussed by taking reference to kinetic barriers observed for other receptor ligand systems and to the opening of DNA by molecular machines.The technique of the molecular force balance has been described in detail elsewhere [4]. Briefly, oligonucleotides labeled at the 3'- or 5' terminus by amino groups are immobilized on an activated slide. Cy3-labeled oligonucleotides then are hybridized to the receptors thereby forming a sample duplex. Subsequently biotin labeled oligonucleotides are hybridized to the sample thereby forming a reference duplex. This results in a molecular balance as it is depicted in Fig. 1a.

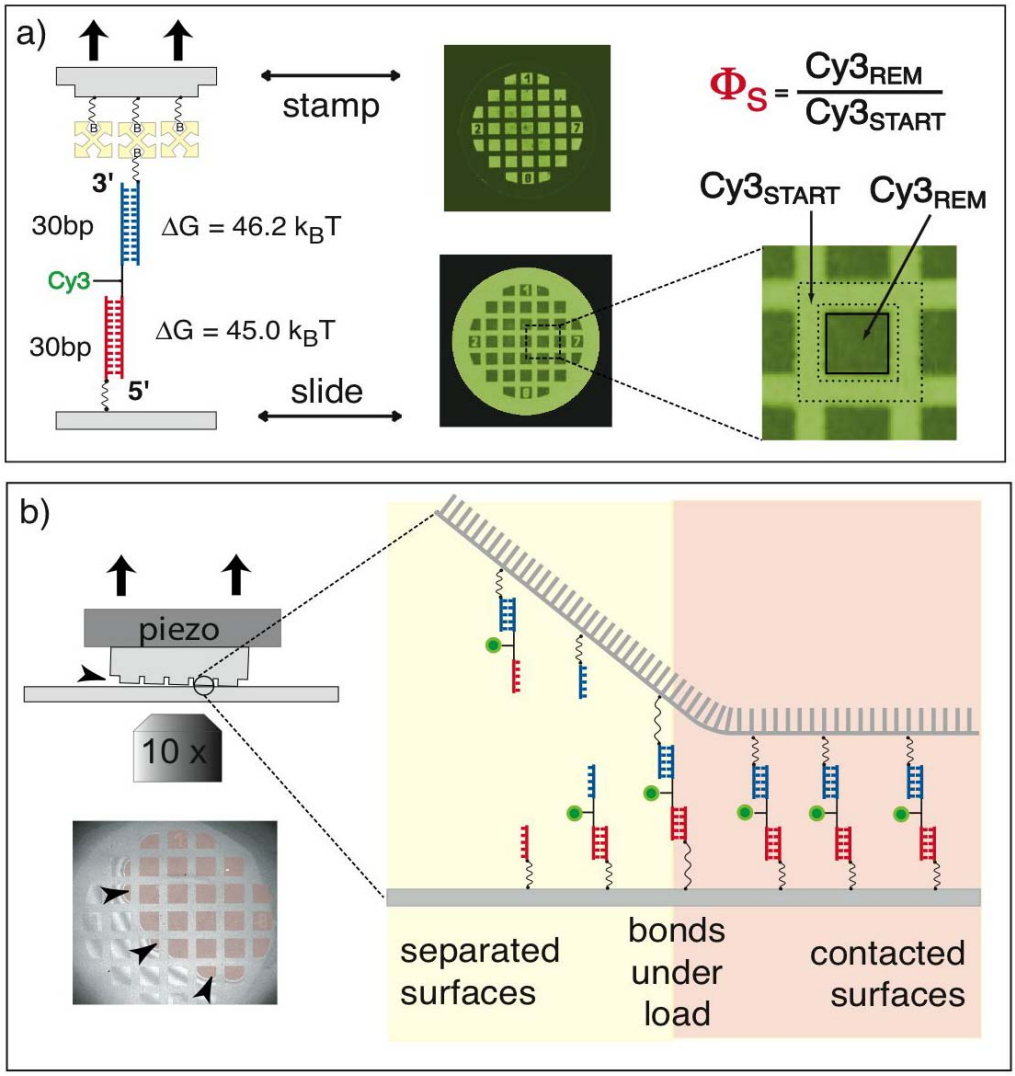

Figure 1: (a) A DNA force balance immobilized on a slide at the sample duplex (red) and to a streptavidin coated stamp at the reference duplex (blue). Micrographs showing the distribution of Cy3-fluor (green) between stamp (top) and slide (bottom) after separation. Survival property of the sample duplex Φ_S is calculated from the remaining intensity on the contact areas $Cy3_{REM}$ (squares) normalized to the starting intensity $Cy3_{START}$ (grid). (b) Schematics and interference micrograph of slide-stamp separation driven by piezo movement. Slide-stamp contact areas (light red) are separated along a moving edge at which the balances are loaded and ruptured. The separation direction is indicated by black arrowheads.

A stamp covered with streptavidin having an elevated microstructure is pressed onto the slide at this time. When the elevated area of the stamp makes contact with the slide, the biotinylated oligonucleotides bind to the streptavidin. Following the formation of biotin-streptavidin bond the stamp is pulled away from the slide. The applied force

gradually increases until the reference duplex or the sample duplex ruptures depending on which one was the weaker link. The Cy3-label of the middle oligonucleotide therefore ends up on the stamp when the sample duplex fails or on the slide when the reference duplex fails. Reading out the slide using a fluorescent scanner determines how much of the Cy3-oligonucleotide remains on the slide ($Cy3_{REM}$) in relation to the starting intensity $Cy3_{START}$. Thus the normalized $Cy3_{REM}$ intensity reflects the survival probability of the sample duplex Φ_S when probed against a certain reference duplex [8]. Structure and sequences of the molecular balances used here are described in the supplement.

Results

In Fig. 2 three experiments are depicted where the same kind of force balance was investigated at different velocities and orientations. Sections of DNA spots on the slides are depicted where fluorescence intensity was corrected for coupling efficiency [8] and normalized to the start-values (intensity of the grid). The area of contact between slide and stamp corresponds to the darker squares, where Cy3-labelled oligonucleotides were probed and removed from the slide. The normalized intensity of the squares corresponds to the survival probability Φ_S of the sample duplex.

In Fig. 2a the stamp was pulled apart by a very low velocity of 0.02 µm/s. The profile (measured along the white arrow in the micrograph) shows normalized intensities between ~0.6 and 1. High values around 1 correlate with the grid structure in the micrograph, while the lower values originate from the rectangular contact areas and correspond to the survival probability of the sample duplex Φ_S. Apart from some noise the Φ_S-profile is relatively flat. For the experiment in Fig. 2b the stamp was removed thousand times faster at 20 µm/s. Under these conditions, the stamp distorts upon

retraction, which results in even higher peak values for the separation velocities in the centers of the square. Although the graph again shows values of ~1 for the grid, the centers of the squares exhibit large irregularities throughout the contact area where Φ_S increases abruptly and culminates in peaks of about 0.9.

In order to address the question if the correlation of high survival probabilities Φ_S and high velocity in Fig. 2b is a property intrinsic to the molecular balance, it was simply probed in a molecular upside-down orientation, again at 20 μm/s. In fact a similar effect but with inverted sign, as shown in Fig. 2c, was the consequence. Expectedly Φ_S dropped down to minima of about ~0.35 instead of giving rise to high values as in the previous experiment. This finding unambiguously corroborates the assumption, that the Φ_S maxima and minima in image 2b and 2c reflect an increased stability of the sample complex compared to the reference complex at higher pulling velocities.

Therefore it was desirable to determine the locally effective pulling velocities, which apparently were different from the external velocity of piezo movement. As described in detail in [8], contacting and separating stamp and slide was monitored by interference contrast microscopy. Inspection of the interference pattern supported the notion of a dynamic separation process, starting with slow separation at the edges of the contact area and accelerating substantially towards the points were contact was maintained longest.

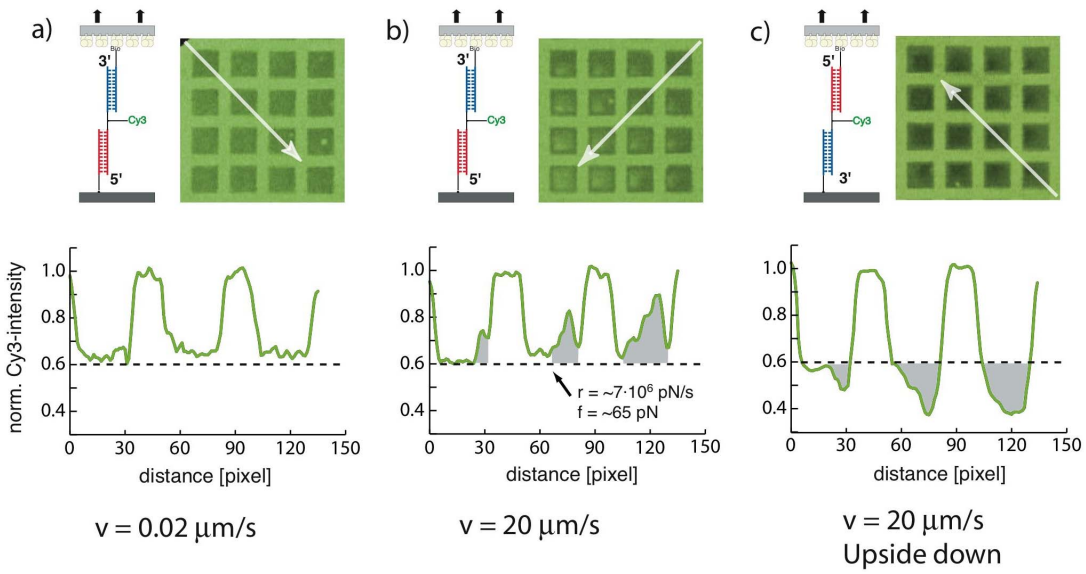

Figure 2: Normalized Cy3-intensity images where the contact areas correspond to Φ_S (survival probability of the sample duplex (red)). White selections in the images are plotted as normalized intensity over distance. Grey areas in the diagrams are specifying the non-linear effect. (a) Molecular force balance probed at 0.02 μm/s: The curve sections between the peaks (Φ_S) are relatively flat. (b) Molecular force balance probed at 20 μm/s: Φ_S is increasing steeply in some contact areas. For the onset of the peaks loading rate and rupture force was calculated (black arrow). (c) Molecular force balance turned upside down and probed at 20 μm/s. Φ_S is steeply decreasing in some contact areas. Images were smoothed by a median filter.

We concluded that the system obviously exhibits an asymmetry at high pulling velocities, despite both duplexes differ by only ~1k_BT in free Gibb's energy (Fig. 1a). This was surprising since the balance should be insensitive to velocity changes due to its putative symmetry. In search for the break in the symmetry we dissected the structure of the force balance as depicted in Fig. 3. Now it was obvious that the assembly of the three oligonucleotides results in a lower duplex with 3'-3'- and an upper duplex with 5'-5'-pulling direction. Hence we concluded, that asymmetry in pulling geometry between the upper and lower duplex gives rise to the non-linear effect. In order to proof this hypothesis we designed a new "rectified" balance were both duplexes were probed in the same direction (Fig. 3a) (see supplements for design). As expected, the rectified balance exhibited no kinetic peculiarities as demonstrated in

Fig. 3. In fact the Φ_S-profile stayed flat for pulling velocities between 0.02 and 20 µm/s and loading rates as high as those accomplished in Fig. 2b (Fig. S1 supplement).

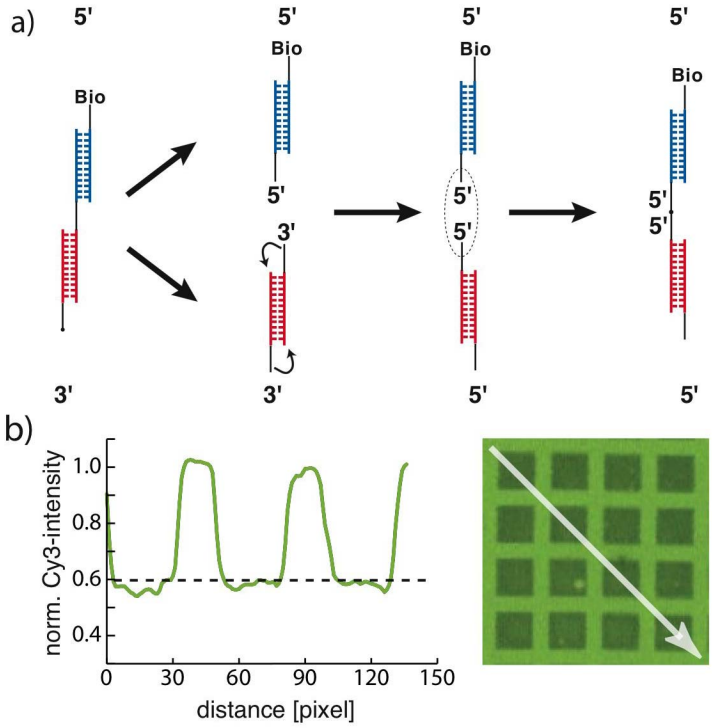

Figure 3: a) Design of a rectified balance: After dissecting the standard balance (left) it is evident that the sample duplex (red) is probed in 3'-3'- and the reference duplex (blue) in 5'-5'-direction. Conjugation of the duplexes at their 5'-termini results in a rectified balance where both duplexes are probed in 5'-5'-direction. The plot refers to the white arrow in the micrograph. b) The rate dependence that was observed for the standard balance (Fig. 2b) was canceled out by the rectified design. Curve was smoothed by a median filter.

Another interesting discovery was made for many images of balances that were probed at 20 µm/s or higher. In Fig. 4 an experiment is depicted, where the standard balance was immobilized in upside down orientation comparable to Fig. 2c. For the green images, the Cy3-signal was normalized to the start intensity. In Fig. 4b free biotins were labeled with soluble strepatvidin-Alexa-Fluor-647-conjugate after separation of stamp and slide, again the image was normalized to the start intensity [8]. In general the Cy3-signal is decreasing to the center of the contact areas comparable to the spots depicted in 2c. However an additional effect is evident in the middle of the central contact areas

where spikes of increased Cy3-intesity are visible in the blow up image. Moreover these spikes are also present in the AF647-image at exactly the same location as evidenced by the line plots. Obviously at these locations both DNA duplexes are still intact but biotinylated oligonucleotides were ruptured from the streptavidin on the stamp.

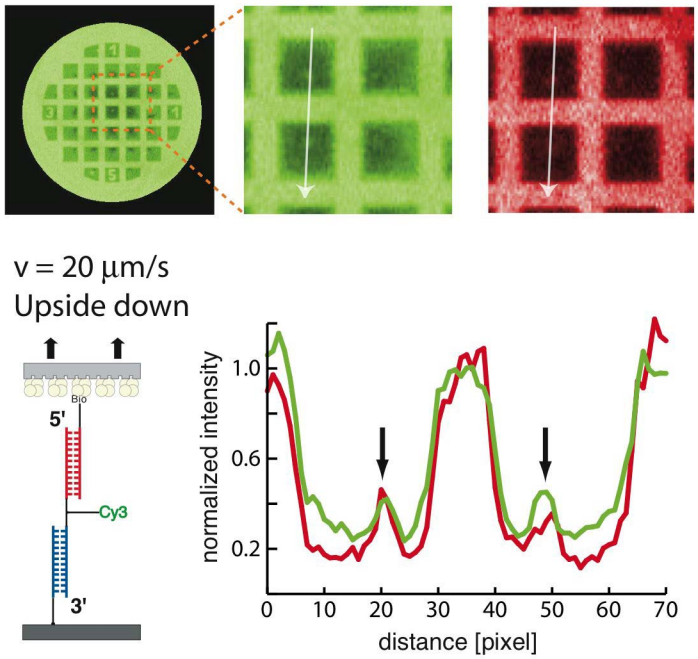

Figure 4: Experiment of an asymmetric standard balance in upside-down orientation pulled at 20 μm/s. Blow up images of the contact area were the putative final contact points show intensity peaks for Cy3 (green) and streptavidin-AF647 which was bound to free biotins (red). The line plots which represent the white arrows in the blow up images show a section through two contact areas and the putative last contact points where velocity and force loading rate is assumed to be maximal (black arrows in the plot). Spikes in the Cy3- and AF647-signal indicate that bonds between biotin-oligonucleotide and streptavidin were ruptured at these points.

Discussion

That different unbinding geometries of the same molecule could give rise to significant differences in rupture force most convincingly has been demonstrated by comparison of DNA unzipping and shearing. While unzipping of a 16mer by pulling apart the 5' and 3' termini at one duplex end a force of only ~10 pN is required, for shearing in 5'-5' direction ~37 pN have been determined at a loading rate of 24 pN/s [14]. Comparable results have been obtained by force balance experiments, when those different unbinding geometries have been measured directly [3, 4]. While diverging forces for unzipping and shearing DNA are very intuitive this is not the case for the two possible shear directions 5'-5' and 3'-3' which are generally assumed to exhibit similar unbinding characteristics. At least no disparity has been measured so far and even sophisticated considerations about DNA melting under force do not reason about it [10]. The only hint comes from simulations where different transition states have been proposed for polymeric DNA namely a narrow fiber for 5'-5' and a unwound ribbon for 3'-3' pulling direction (Fig. 5d) [12, 13, 15].

In Fig. 2b we have shown that the balance turns out to be asymmetric, once a critical loading rate is exceeded. The effect was found to appear at a loading rate of $\sim 9 \cdot 10^5$ pN/s and a rupture force of ~65 pN [8] and is due to a kinetic unbinding barrier comparable to those which have been reported for the biotin-streptavidin and hapten-antibody complexes [16, 17]. Here we now demonstrate that the asymmetry arises because of the difference in geometry of the 5'-5' and 3'-3' pulling direction and vanishes again when a rectified balance with two 5'-5' duplexes, is used (Fig. 3).

We think that the so called "S-form" transition states [12, 13] which are structurally different for the two pulling directions (Fig. 5d) are the origin of the asymmetry.

However, since this asymmetry only becomes visible above a critical loading rate, another unbinding mechanism, which is insensitive to the pulling direction, must exist at lower loading rates. We assume that DNA "bubbles" are responsible for unbinding at low loading rates according to the "force induced melting" hypothesis [10]. Because those thermal fluctuations are non-directed, they are suited to obscure the most part of the geometrical difference of unbinding in 5'-5' and 3'-3' direction. According to this, a distinction could be drawn between two regimes of unbinding: One in quasi-equilibrium at low loading rates where the reaction takes place assisted by thermal fluctuations and a kinetic regime at elevated loading rates, where deformation is dominant over fluctuations and geometric properties of the helix are more meaningful.

In order to proof this assumption we wanted to compare our results to studies where fluctuation in DNA have been measured directly. In [18], Altan-Bonnet has demonstrated, that AT-rich sequences in a short duplex give rise to bubble-like fluctuations which are characterized by a rate of 10^4-10^5 /s. If one assumes now that a breathing rate of ~10^5 /s could be identified as the attempt frequency ν_{off} used in the Bell-Evans model

$$F \cdot \Delta x = k_B T \cdot \ln \frac{r \cdot \Delta x}{k_B T \cdot \nu_{off} \cdot e^{(-\Delta G_{off} / k_B T)}} \qquad \text{(equation 1)}$$

and furthermore the loading rate of ~$9 \cdot 10^5$ pN/s measured at the kinetic effect is inserted in equation 1, then the relation ends up with $F \cdot \Delta x \approx \Delta G_{off}$. With other words by assuming an attempt frequency typical for the breathing mode of DNA, the mechanical power $r \cdot \Delta x$ applied to the bond approaches the power achieved by thermal fluctuations $\nu_{off} \cdot k_B T$. This means, that the duplex would have no more time to escape from the potential well by fluctuations, since the loading rate applied approaches the attempt

frequence very closely. For situations where the mechanical work eventually equals the whole depth of the well $F \cdot \Delta x = \Delta G_{off}$, the potential model is not valid any more, since it requires the possibility of the duplex to escape from the well by fluctuations. At this point very likely a description based on continuums mechanics like that in [12] would describe the experiment adequately.

We therefore argue that the kinetic barrier observed in Fig. 2a and 2b probably occurs when the mechanically forced separation of the strands is faster than the opening kinetics of the fluctuation bubbles, and hence thermal contributions are becoming less important for unbinding. With other words: Once force has build up in a DNA helix which partially was opened by thermal fluctuations, then the closing reaction of the bubble will be stalled by the applied strain and further extension of the bubble proceeds until the strands are separated. When the force-loading rate however is faster than the inherent opening rate, than the remaining base pairs will be disrupted predominantly by mechanics. Accordingly, stretched conformations with intact base pairing ("S-forms") (Fig. 5d) are becoming more important for the transition state than bubbles when a critical loading rate of $\sim 9 \cdot 10^5$ pN/s is exceeded. The fact that even biotin streptavidin complexes are disrupted close to the position on the slide where the kinetic effect occurred, corroborates, that much higher forces are accomplished, in the loading rate regime after the kinetic effect (Fig. 4).

The hypothesis is summarized in figure 5: a) At zero force DNA is in B-conformation except of the ends, where the duplex is constantly opened and closed (curved arrows) by thermal fluctuations. b) At moderate loading rates the bubbles are rapidly extended by fluctuations because the closing reaction is hindered due to the applied strain that keeps one strand at every duplex end in single stranded conformation. c) At a critical

loading rate the strain is applied faster than the fluctuations and significant deformation work is carried out, that drives both duplexes into different stretched conformations.

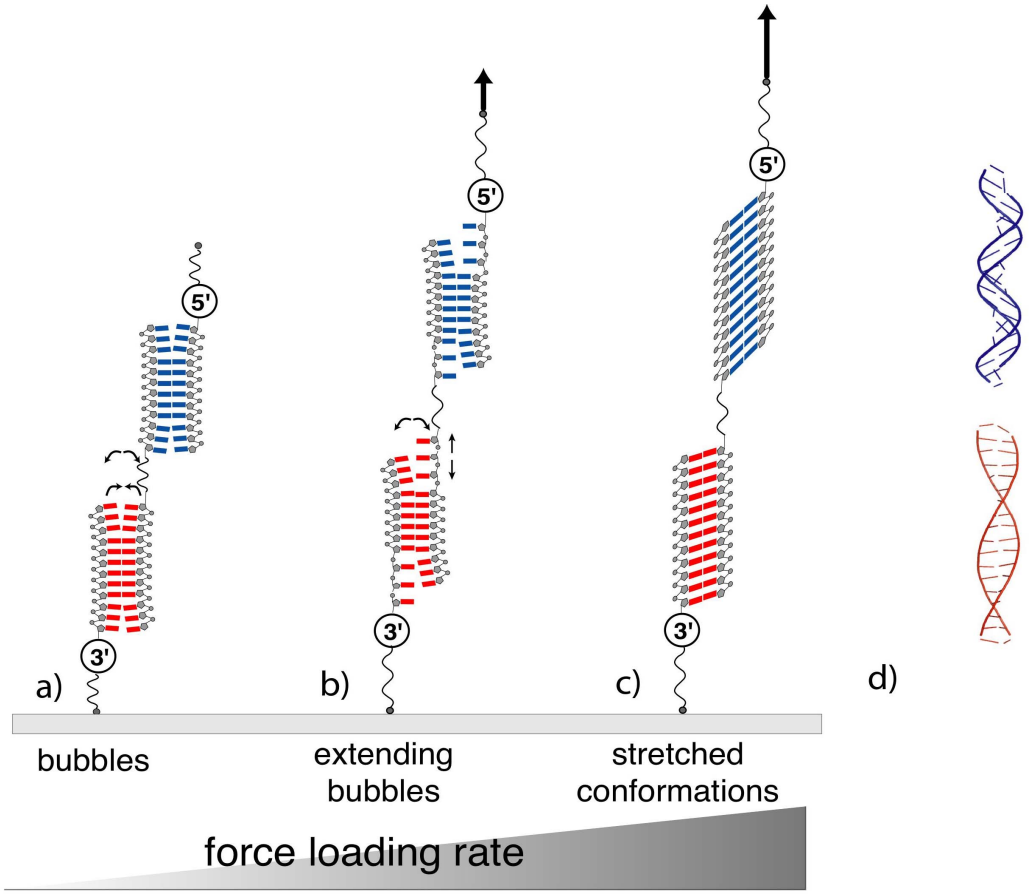

Figure 5: Model for the dominant transition state of DNA rupture dependent on pulling geometry and force loading rate. a) Unstretched B-DNA at zero force. Fluctuations are opening and closing the duplex at the ends (curved arrows) b) At moderate loading rates bubbles are growing because the applied strain hinders the closing reaction (small vertical arrows). c) At loading rates higher than $9 \cdot 10^5$ pN/s the duplexes are forced into stretched conformations with intact base pairing. d) 5'-5' and 3'-3' pulling directions lead to different duplex structures (polyGC duplexes stretched 1.6 times from [12, 15]).

Explaining kinetic unbinding barriers by explicit relaxation times or the frequency of fluctuations might be relevant for receptor-ligand interactions in general. Kinetic unbinding barriers have first been reported for biotin-avidin [16, 17] and later for antigen-antibody complexes [19], [17]. A relation between temporal fluctuations characteristics and the external pulling rate might be suitable to explain those barriers as

well. However one had to assume even much slower fluctuation kinetics than for DNA bubbles, since the barriers for avidin are found at 10^2 and 10^4 pN/s.

Our results give evidence that opening of short DNA-duplexes is assisted by thermal fluctuations up to a loading rate of ~$9 \cdot 10^5$ pN/s when force is applied in parallel to the helix. Above that limit molecular machines would have to apply much higher forces in the separation of the double strand due to higher energy dissipation. Of course $9 \cdot 10^5$ pN/s is a very high value that hardly ever could be accomplished even by the strongest molecular machines. However when proteins are bound to the helix, presumably lower loading rates are required to convert DNA into a stretched and completely closed conformation, comparable to those in RecA recombination.

Moreover it is likely that application of force in 5'-5' direction indeed causes "inwinding", leading to a double strand of smaller diameter as suggested in [12, 13]. Even so this mechanism will not result in opening of long DNA, the smaller diameter maybe useful in situations where DNA has to be pulled through a narrow hole. The question if different pulling directions and loading rates will give rise to different effects when proteins are bound to the helix will be one of the next subjects to be addressed by molecular balance experiments.

References

1. Prevost, C. and M. Takahashi, *Geometry of the DNA strands within the RecA nucleofilament: role in homologous recombination.* Q Rev Biophys, 2003. **36**(4): p. 429-53.
2. Gelles, J. and R. Landick, *RNA Poymerase as a molecular motor.* Cell, 1999. **93**: p. 13-16.
3. Albrecht, C., et al., *DNA: a programmable force sensor.* Science, 2003. **301**(5631): p. 367-70.
4. Albrecht, C., H. Clausen-Schaumann, and H. Gaub, *Differential analysis of biomolecular rupture forces.* Journal of Physics: Condensed Matter, 2006. **18**: p. 1-19.
5. Neuert, G., C. Albrecht, and H. Gaub, *Predicting the rupture probabilities of two bonds in series.* Biophys J, 2007. **accepted**.
6. Florin, E.L., V.T. Moy, and H.E. Gaub, *Adhesion forces between individual ligand-receptor pairs.* Science, 1994. **264**(5157): p. 415-7.
7. Strunz, T., et al., *Dynamic force spectroscopy of single DNA molecules.* Proc Natl Acad Sci U S A, 1999. **96**(20): p. 11277-82.
8. Albrecht, C., et al., *Dynamic force spectroscopy with a molecular balance.* Biophys J, 2007. **submitted**.
9. Smith, S.B., Y. Cui, and C. Bustamante, *Overstretching B-DNA: the elastic response of individual double-stranded and single-stranded DNA molecules.* Science, 1996. **271**(5250): p. 795-9.
10. Rouzina, I. and V.A. Bloomfield, *Force-induced melting of the DNA double helix 1. Thermodynamic analysis.* Biophys J, 2001. **80**(2): p. 882-93.
11. Harris, S.A., Z.A. Sands, and C.A. Laughton, *Molecular dynamics simulations of duplex stretching reveal the importance of entropy in determining the biomechanical properties of DNA.* Biophys J, 2005. **88**(3): p. 1684-91.
12. Lebrun, A. and R. Lavery, *Modelling extreme stretching of DNA.* Nucleic Acids Res, 1996. **24**(12): p. 2260-7.
13. Konrad and Bolonick, *Molecular dynamics simulation of DNA streching is consistent with the tension observed for extension and strand separation and predicts a novel ladder structure.* JACS, 1996. **118**: p. 10989.
14. Lang, M.J., et al., *Simultaneous, coincident optical trapping and single-molecule fluorescence.* Nat Methods, 2004. **1**(2): p. 133-9.
15. Lavery, R. and A. Lebrun, *Modelling DNA stretching for physics and biology.* Genetica, 1999. **106**(1-2): p. 75-84.
16. Merkel, R., et al., *Energy landscapes of receptor-ligand bonds explored with dynamic force spectroscopy.* Nature, 1999. **397**(6714): p. 50-3.
17. Neuert, G., et al., *Dynamic force spectroscopy of the digoxigenin-antibody complex.* FEBS Lett, 2006. **580**(2): p. 505-9.
18. Altan-Bonnet, G., A. Libchaber, and O. Krichevsky, *Bubble dynamics in double-stranded DNA.* Phys Rev Lett, 2003. **90**(13): p. 138101.
19. Berquand, A., et al., *Antigen binding forces of single antilysozyme Fv fragments explored by atomic force microscopy.* Langmuir, 2005. **21**(12): p. 5517-23.

Acknowledgements

We thank Richard Lavery for the pdb files of stretched DNA.

Supplement

Structure and synthesis of the molecular balances:

oligo dir.	pulling dir.	oligo no.	sequence
3'-5'	**3'-3'**	#134	NH2-10t-CTGCAGGAATTCGATATCAAGCTTATCGAT
5'-3'		#118	GACGTCCTTAAGCTATAGTTCGAATAGCTAc-8t-Cy3-8t-cATCGATAAGCTTGATATCGAATTCCTGCAG
3'-5'	**5'-5'**	#62	TAGCTATTCGAACTATAGCTTAAGGACGTC-10t-Bio

5'-3'	**5'-5'**	#124	NH2-10t-CTGCAGGAATTCGATATCAAGCTTATCGAT
3'-5'		#118	GACGTCCTTAAGCTATAGTTCGAATAGCTAc-8t-Cy3-8t-cATCGATAAGCTTGATATCGAATTCCTGCAG
5'-3'	**3'-3'**	#125	TAGCTATTCGAACTATAGCTTAAGGACGTC-10t-Bio

5'-3'	**5'-5'**	#113	NH2-10t-TAGCTATTCGAACTATAGCTTAAGGACGTC
3'-3'		#117	ATCGATAAGCTTGATATCGAATTCCTGCAGc-6t-Cy3t-sfb-sanh-8t-cATCGATAAGCTTGATATCGAATTCCTGCAG
3'-5'	**5'-5'**	#123	TAGCTATTCGAACTATAGCTTAAGGACGTC-10t-Bio

Table S1: Molecular balances drawn in horizontal orientation. Left = slide, right = stamp. Oligonucleotide direction and pulling direction of duplexes in bold charachters. Top: Standard balance in normal orientation: 3'-3' pulling direction of sample duplex (red) and 5'-5' pulling direction of reference duplex (blue). Sample duplex is oriented to the slide. Middle: Standard balance in inverted orientation. 3'-3' sample duplex is oriented to the stamp. Bottom: Rectified balance with oligonucleotide-conjugate having two 3'-termini. Both duplexes are in probed in 5'-5' direction. Labels: NH2 = amino; Cy3 = Cyanin-3 fluor; Bio = biotin; 8t = poly-t-spacer. Conjugation: SFB-aldehyde and SANH-hydrazin reagents.

All DNA oligonucleotides were purchased from IBA GmbH Goettingen, Germany. The "rectified" oligonucleotide-conjugate with two 3'-termini was assembled from two separate oligonucleotides that were amino-modified at their 5'-termini. One oligonucleotide was remodified by SFB- (aldehyde) and the other by SANH- (hydrazin) reagent. Subsequently both were conjugated to each other (all done by IBA GmbH according to: Kozlov et al., Biopolymers, 2005. 73 (5): 621-630). All experiments were carried out in 1xSSC buffer (150 mM NaCl, pH 7.2).

12. Anhang (Material und Methoden)

Bei der Plattform für die differenziellen Messungen handelt es sich technisch betrachtet um eine Kombination aus einem DNA-Array mit der Methode des Mikrokontaktstempelns [1]. DNA-Arrays zum hochparallelen Nachweis von Nukleinsäuremolekülen sind heute unter dem Namen „DNA-Chips" bekannt, eine Technik, bei der tausende von DNA-Sonden als „Spots" von etwa 100 µm Durchmesser auf einem Objektträger angebunden werden. Dem Prinzip nach geht die Methode auf Edwin Southern zurück, der sie als „reversen Southernblot" eingeführt hatte, ohne jedoch über die Technologie zur Miniaturisierung zu verfügen, welche später für die als „Genomics" bekannte Forschung ausschlaggebend wurde [2]. Da es auch für die differenziellen Kraftmessungen von Vorteil ist, mehrere Kraftwaagen gleichzeitig vermessen zu können, wurde ein Muster von 4 x 4 Messflecken auf einem Feld von einem Quadratzentimeter als „Array" definiert, ein Grad an Parallelisierung, der mit sehr einfachen Methoden zu verwirklichen ist, ohne dass dabei viel Aufwand in „Array-Technologie" investiert werden muss.

12.1 Die Herstellung des Stempels

Der Stempelrohling

Im Gegensatz zu den Objektträgern, die fertig für den Gebrauch zu kaufen sind, musste für die Herstellung des Stempel ein erheblich größerer Aufwand betrieben werden. Wie bei der Methode des Mikrokontaktstempelns hat der Silikonstempel die Aufgabe, sich bei geringem Anpressdruck an die harte Glasoberfläche anzuschmiegen und somit einen molekularen Kontakt zu den Kraftwaagen herzustellen. Dies wird durch den Umstand erschwert, dass der sich zwischen den Oberflächen befindliche Puffer weitgehend verdrängt werden muss, was sich bei einer Kontaktfläche von etlichen Quadratmillimetern nur dadurch realisieren ließ, indem die Silikonfläche durch Mikrokanäle strukturiert wurde, um das Ablaufen des Puffers zu erleichtern.

Trotzdem erwies es sich als sehr schwierig, den zuerst verwendeten Stempel von 1 mm Stärke und einer Fläche von 1 cm^2 über die gesamte Fläche unter gleichmäßigem Druck mit dem Objektträger in Kontakt zu bringen. Weit bessere Resultate wurden schließlich mit einem Stempel erzielt, bei dem der Kontakt zum Objektträger auf die Stirnfläche

von weit hervorstehenden Noppen reduziert wurde (Abb. 21). Die damit verbundene Änderung des Aspektverhältnisses von 1:10 (alter Stempel) auf 1:1,1 (Noppe) erwies sich dabei als sehr günstig, da der Stempel dadurch siebenmal weicher wurde und sehr viel gleichmäßiger in Kontakt gebracht werden konnte (P2).

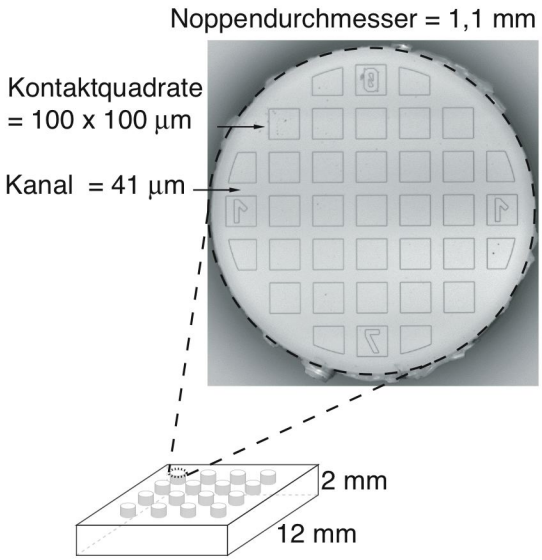

Abbildung 21: Silikonstempel mit sechzehn Noppen von 1 mm Höhe und 1,1 mm Durchmesser. Der vergrößerte Ausschnitt zeigt eine Aufnahme der Stirnfläche einer Noppe, auf der man die Mikrostruktur erkennen kann. Dabei handelt es sich um 5 µm erhabene Quadrate mit einer Kantenlänge von 100 µm, welche die eigentliche Kontaktfläche zum Objektträger darstellen.

Für die Herstellung des Stempels musste aufgrund der besonderen Anforderung, Millimeter große Noppen mit einer Mikrostruktur zu verbinden, eine Gussform aus zwei Komponenten entwickelt werden. Zuerst wurden die Mikrostrukturen in einen SOI-Wafer mit einer 5 µm starken Siliziumschicht geätzt. Daraufhin wurde eine 1 mm starke Pyrexglasplatte durch Ultraschallbohren mit Durchbrüchen von 1,1 mm Durchmesser versehen (Abb. 22c). Wafer und Pyrexglas wurden schließlich durch anodisches Bonden miteinander verbunden und als Komposit durch eine sehr dünne und gleichmäßige Klebeschicht auf einer Bodenplatte befestigt (Abb. 22a). Die Herstellung der gesamten Kompositform wurde bei HSG-Imit, Institut für Mikrotechnik, in Villingen-Schwenningen in Auftrag gegeben. Um die Gussform zu vervollständigen, wurde ein hufeisenförmiger Aluminium-Spacer angefertigt, der als Halterung für vier Kugellagerkugeln dient und an dessen Innenseite ein aufgeschlitzter Silikonschlauch (4,5 mm Durchmesser) als Dichtung aufgezogen wird. Zuletzt wird eine Glasdeckelplatte auf den Spacer gelegt und mit Klammern befestigt (Abb. 22b). Als sehr wichtig erwies es sich, den Wafer-Pyrex-Komposit mit einer Lösung aus 0,2 %

Fluorsilan in Hexan zu behandeln, da der auspolymerisierte Silikonrohling andernfalls nicht entformt werden kann (im schlimmsten Fall lässt sich Silikon mit Trifluoressigsäure aus der Form lösen).

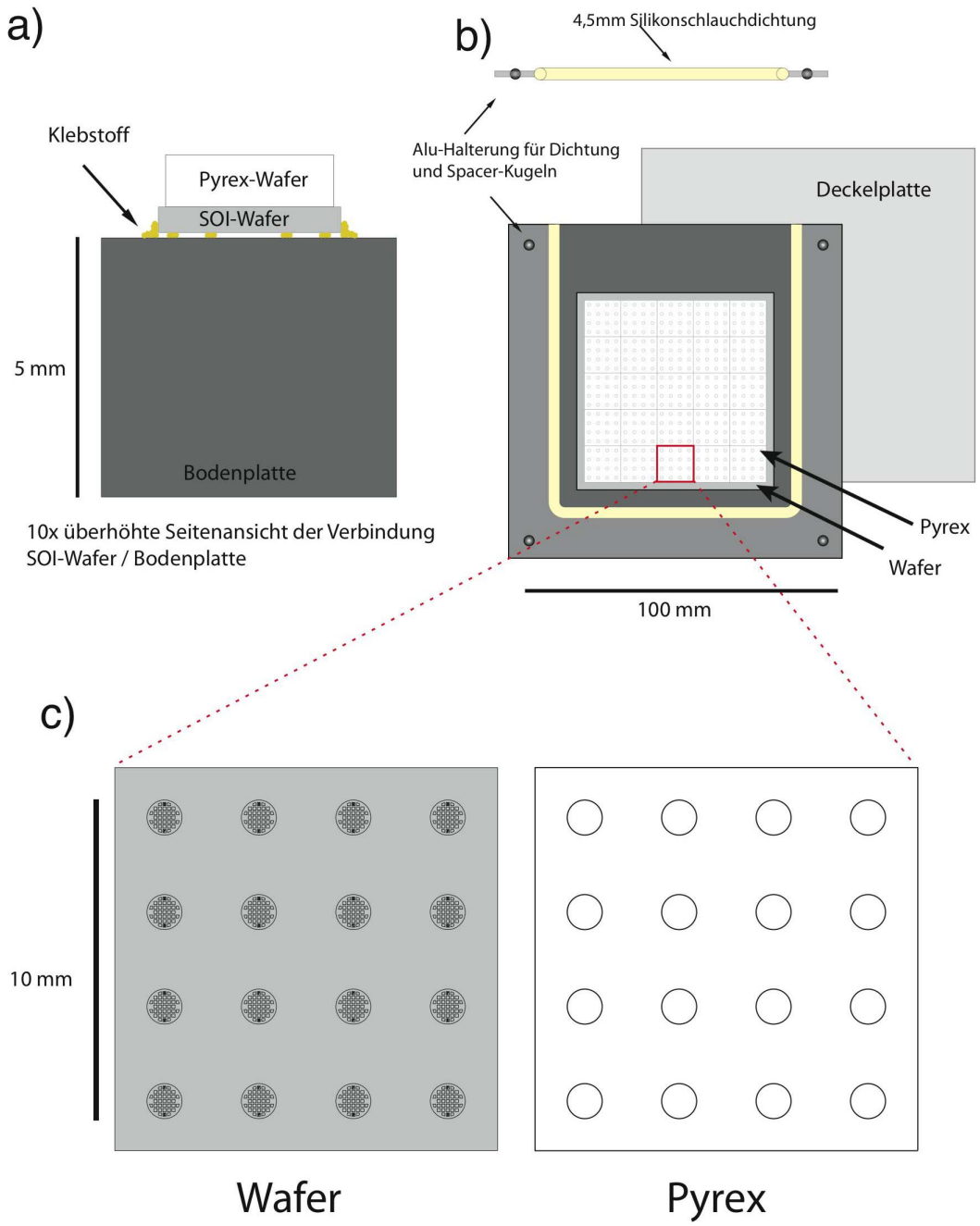

Abbildung 22: a) 5x überhöhte Seitenansicht der Gussform mit dem Verbund aus SOI- und Pyrexwafer, der durch Klebstoff auf der Bodenplatte befestigt wird. b) Aufsicht auf die gesamte Gussform, in der 25 Noppenstempel gegossen werden können. Auf die hufeisenförmige Aluminium-Halterung ist als Dichtung ein Silikonschlauch aufgezogen. Kugellagerkugeln dienen als Abstandshalter zwischen der Bodenplatte und der Deckelplatte. c) Ausschnitt, der die Bohrungen des Pyrexwafers und die Mikrostruktur des SOI-Wafers für einen einzelnen Stempel zeigt.

Der Guss der Stempel erfolgt mit einem handelsüblichen Zweikomponenten-Polydimethylsiloxan (PDMS), wobei das Siloxanpolymer und der Vernetzer 1:10

gemischt werden. Nach intensivem Entgasen wird das Gemisch in die Form gefüllt. Um das blasenfreie Eindringen des Gemischs in die Bohrungen der Pyrexplatte zu ermöglichen, wird die befüllte Form in einen Exikator gestellt und wiederholt evakuiert, bis alle Kavitäten befüllt sind. Die Polymerisation erfolgt über Nacht bei Raumtemperatur und anschließend für 24 h bei 50 °C. Nach der Entformung wird der Silikonrohling schließlich mit einem rotierenden Tapetenmesser in die einzelnen Stempelrohlinge mit jeweils 4 x 4 Noppen zerteilt. Um nicht auspolymerisierte Siloxanmonomere aus den Stempelrohlingen zu entfernen, werden diese in einer Soxhlet-Apparatur für 24 h in Toluol extrahiert. Nach drei Tagen Trocknen sind die Stempelrohlinge schließlich bereit für die Oberflächenbeschichtung.

Die Beschichtung des Stempels

Die für das differenzielle Messverfahren notwendigen Oberflächeneigenschaften sind im Prinzip dieselben wie die für eine kraftspektroskopische Messung mit dem AFM (atomic force microscope). Dabei ist es besonders wichtig, dass die spezifischen Rezeptor-Ligand-Interaktionen nicht durch unspezifische Molekül-Oberflächen-interaktionen überdeckt werden und dass die Beschichtung eine hohe Stabilität gegenüber den angelegten Zugkräften aufweist. Darüber hinaus ist es notwendig, die Kraftwaagen zumindest auf einer Seite an lange, elastische Polymerspacer anzubinden, um die Kraftladungsrate bei den Experimenten in einem moderaten Bereich zu halten.

Für die Beschichtung des Stempels wurden zwei Alternativen entwickelt, die beide auf einer Silanisierung und der anschließenden Anbindung von Biotin-Polyethylenglycol (Bio-PEG) beruhen. Die wichtigste Voraussetzung bei diesem Vorgehen besteht darin, dass die Oberfläche des Silikonpolymers nicht mit unvernetzten Siloxanmolekülen verunreinigt ist. Eine nur oberflächliche Reinigung ist hier nicht ausreichend, da sich auch im Silikonkörper eine erhebliche Menge nicht vernetzter Siloxane befindet, die auf die bereits beschichtete Oberfläche „kriechen" können und somit erneut zu einem hydrophoben Schmierfilm führen. Um dieses Phänomen zu vermeiden, das auch als „hydrophobic recovery" bekannt ist [3], ist die oben beschriebene Extraktion der nicht vernetzten Siloxane mit Toluol eine unbedingte Voraussetzung. Der erste Schritt der Beschichtung besteht darin, die Stempelrohlinge über Nacht in 12%iger Salzsäure zu aktivieren, wodurch es zur teilweisen Hydrolyse von PDMS-Siloxanen und somit zur Bildung von Hydroxygruppen auf der Oberfläche kommt. Die Salzsäure wird nun sehr gründlich mit H_2O abgewaschen und die Stempel werden sofort weiterverarbeitet.

Bei der ersten Beschichtungsvariante handelt es sich um eine Aminosilanisierung mit anschließender Anbindung von Biotin-PEG-NHS. Dafür werden die Stempel für 20 min in einer Lösung aus 10 % H_2O, 2 % Aminosilan in reinem Ethanol inkubiert, anschließend mit Ethanol gewaschen und trocken geblasen. Um eine bessere Reaktivität der Aminogruppen zu gewährleisten, werden NH_3^{+-}Gruppen durch eine kurze Behandlung mit 100 mM NaOH in die NH_2-Form überführt. Daraufhin wird kurz mit H_2O gewaschen und trocken geblasen. Nun wird jede Noppe mit 2 µl einer 6-mM-Lösung aus Biotin-PEG-NHS in H_2O überschichtet und für 1 h in einer mit Wasserdampf gesättigten Kammer inkubiert. Nach gründlichem Waschen in H_2O und Trockenblasen sind die Stempel nun fertig für die Anbindung von Streptavidin. Die Hauptproblematik der Aminosilan-Methode besteht in der geringen Wasserlöslichkeit des Biotin-PEG-NHS, die keine höhere Konzentration als 6 mM zulässt. Da PDMS von anderen Lösungsmitteln wie DMSO zersetzt wird, ist eine Verbesserung der Löslichkeit auch auf diesem Weg nicht möglich. Folglich kommt es zu einer relativ unvollständigen und hydrophoben Beschichtung, bei der vermutlich ein erheblicher Anteil der Aminogruppen nicht umgesetzt wird. Dies kann man aus Experimenten schließen, bei denen die gleiche Kraftwaage in verschiedenen NaCl-Konzentrationen vermessen wurde. Dabei stellte es sich heraus, dass es bei Konzentrationen < 100 mM NaCl zu einer unspezifischen Adsorption der Kraftwaagen an den Stempel kam, die sehr wahrscheinlich auf eine Wechselwirkung der positiv geladenen NH_3^+-Gruppen mit der negativ geladenen DNA zurückzuführen ist. Da alle hier präsentierten Messungen, die auf dieser Beschichtung basierten, bei 150 mM NaCl durchgeführt wurden, ist ein störender Einfluss durch unspezifische Wechselwirkung auszuschließen [4].

Um eine elektrostatische Interaktion der DNA mit der Stempeloberfläche auszuschließen, wurde eine zweite Beschichtungsvariante mit einer Grundfunktionalisierung aus ungeladenem Epoxysilan entwickelt. Ein weiterer Vorteil der Epoxyde besteht darin, dass sie mit geschmolzenem NH_2-PEG abreagieren [5], was zu einer deutlich hydrophileren und wahrscheinlich sehr viel dichteren Schicht führt, als dies mit die Aminosilanmethode möglich ist. Für die Epoxy-Silanisierung wird zuerst eine Verdünnung von 38,3 µl konzentrierte H_2SO_4 mit 250 ml H_2O hergestellt. Daraufhin wird 919 µl Epoxysilan mit 394 µl der verdünnten Schwefelsäure für 1 h gerührt und mit 25 ml Isopropanol verdünnt. In dieser Lösung werden die Stempel für 20 min inkubiert, sodann mit Isopropanol und H_2O gewaschen und trocken geblasen.

Für die PEG-Schmelze werden für vier Stempel 18 mg Methoxy-PEG-NH_2 mit 6 mg Biotin-PEG-NH_2 gemischt und auf einer Heizplatte bei 80 °C zum Schmelzen gebracht. Von dieser Mischung werden mithilfe einer erwärmten Nadel ca. 2 µl auf jede Noppe eines auf 80 °C erwärmten Stempels aufgetragen. Der Stempel wird nun in einem mit Argon gefüllten Exikator über Nacht bei 80 °C inkubiert. Abschließend wird der Stempel mit 80 °C heißem H_2O gewaschen und für 30 min in kochendes H_2O gestellt, um nicht-kovalent gebundenes PEG zu entfernen. Die somit biotinylierten Stempel können mindestens für eine Woche gelagert werden.

Die Anbindung des Streptavidins erfolgt stets kurz vor der Messung. Dazu wird der Stempel in einer Lösung von 1 µg/ml Streptavidin mit 0,4 % BSA in 1 x PBS unter Schütteln für 30 min inkubiert. Es wird gründlich mit 0,2 x PBS gewaschen und trocken geblasen.

12.2 Die Herstellung des Objektträgers

Zur Anbindung der DNA-Messflecken wird eine einfache Vorrichtung verwendet, wie in Abb. 23 dargestellt. Dafür wird einer der oben beschriebenen Stempelrohlinge auf jeder Noppe mit 1,5µl DNA-Lösung beladen und kopfunter an einen Schlitten gehängt, der geführt von zwei Stangen in vertikaler Richtung über dem Objektträger auf und ab gefahren werden kann. Wird der Schlitten in eine Position von etwa einem Millimeter über den Objektträger gebracht, so wird dieser von den Tropfen benetzt, worauf der Schlitten zurückgezogen wird. Auf diese Art können auf jedem Objektträger zwei Felder mit einem gut definierten 4x4-Muster hergestellt werden.

Die wichtigste Anforderung an den Objektträger besteht darin, das unterste Oligonukleotid der Kraftwaage in hoher Dichte, kovalent und sehr orientierungsspezifisch anzubinden. Aus diesem Grund werden Aldehydobjektträger verwendet, die sehr spezifisch mit einer künstlich in die Oligonukleotide eingeführten Aminogruppe abreagieren. Die an sich nur schwach exotherme Reaktion von Aldehyd und Aminogruppe zu einer Schiff'schen Base muss dabei durch Entzug des entstehenden Wassers begünstigt werden, was man durch sehr hohe Salzkonzentrationen erreichen kann. Die Reaktion erfolgt deshalb in 5 x SSC (750 mM NaCl) bei 70 % relativer Luftfeuchtigkeit (über einer gesättigten NaCl-Lösung) und

über Nacht. Dadurch kommt es zu einer starken Reduktion des Volumens des DNA-Lösungstropfens, ohne dass dieser jedoch eintrocknet.

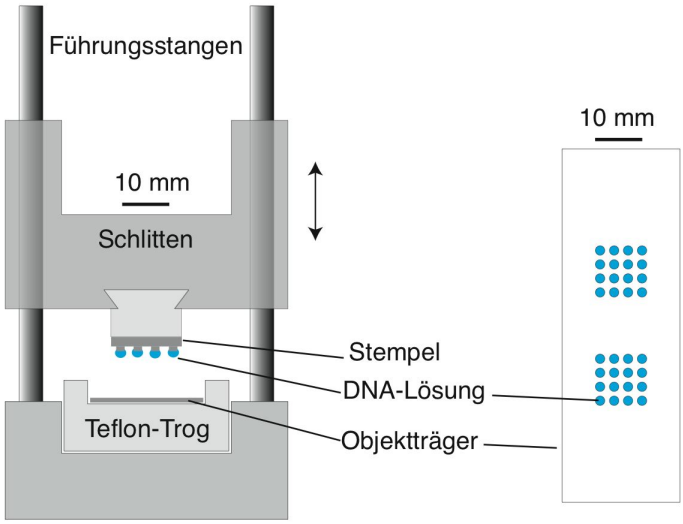

Abbildung 23: Vorrichtung zum Aufbringen der DNA-Messflecken auf den Objektträger. Die Noppen eines Silikonstempels werden mit Oligonukleotidlösung beladen. Der Stempel wird darauf kopfunter an den Schlitten der Vorrichtung befestigt und so weit abgesenkt, bis die Tropfen den Objektträger benetzen.

Der Objektträger wird nun mit H_2O gewaschen und für zwei Stunden in einer Lösung von 4 mg/ml Natriumborhydridlösung inkubiert, was zur Reduktion der Schiff'schen Basen führt. Nach 30 min Blocken in einer 0,4 % BSA-Lösung wird abschließend mit H_2O gewaschen und sehr vorsichtig mit einem Stickstoffstrahl trocken geblasen.

Falls es erwünscht ist, verschiedene Kraftwaagen auf demselben Feld zu verwenden, ist es notwendig, die Hybridisierung auf jedem Messflecken in einem separaten Reservoir durchzuführen. Dies gelingt mithilfe einer Hybridisierungsmaske aus Silikon, die entsprechend dem Muster der Messflecken sechzehn runde Durchbrüche aufweist und die mit dem in Abb. 23 beschriebenen Gerät ortsgenau auf den Objektträger aufgebracht wird (Abb. 24 Mitte). Um für jedes der beiden Felder ein Pufferreservoir zu schaffen, wird nun ein Plexiglasrahmen mit zwei Durchbrüchen auf den Objektträger aufgesetzt, wie in Abb. 24 gezeigt. Die Dichtigkeit zwischen dem Objektträger und der Plexiglasplatte ist dabei durch eine Silikondichtlippe gewährleistet, die fest mit der Platte verklebt wird.

Bei der nun folgenden Hybridisierung werden in jedes Reservoir der Maske 3 µm einer Mischung von 100 nM des Cy3-Oligonukleotids und 200 nM des Biotin-

Oligonukleotids in 5 x SSC-Puffer gegeben. Nach 30 Minuten Inkubation bei Raumtemperatur wird der Objektträger gründlich mit 1 x SSC gewaschen und abschließend mit 1 x SSC überschichtet, ohne dass es dabei zur Entnetzung der Oberfläche kommt. Der Objektträger ist somit fertig zum Kontaktieren mit dem Stempel.

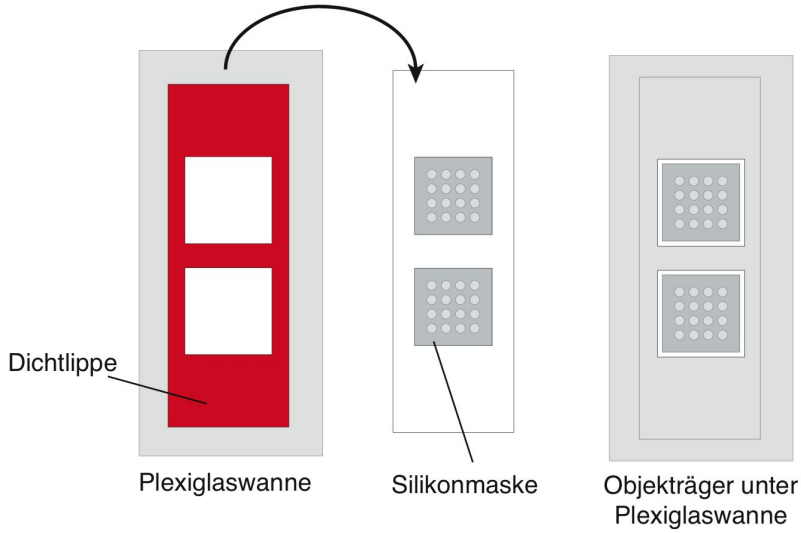

Abbildung 24: Auf den mit Messflecken versehenen Objektträger werden zuerst Hybridisierungsmasken aus Silikon aufgelegt. Durch Aufsetzen des Plexiglasrahmens mit der roten Silikondichtlippe auf den Objektträger werden die für das Kontaktieren mit dem Stempel notwendigen Pufferreservoirs geschaffen.

12.3 Das Kontaktgerät

Prinzipiell gibt es zwei mögliche Vorgehensweisen, einen ebenmäßigen Kontakt zwischen dem Stempel und dem Objektträger herzustellen. Entweder fertigt man die beiden Teile in äußerster Präzision, um sie dann in einer fest justieren Vorrichtung in Kontakt zu bringen, oder man nimmt individuelle Abweichungen des Stempels in Kauf, die durch eine nachjustierbare Kontaktvorrichtung ausgeglichen werden. Tatsächlich stellte es sich heraus, dass ein elastisches Gebilde aus Silikon kaum mit ausreichend guten Toleranzen herzustellen ist. Aus diesem Grund wurde ein Apparat konstruiert, mit dem die Neigung des Stempels eingestellt werden kann und bei dem das Kontaktieren unter optischer Kontrolle stattfindet (Abb. 25).

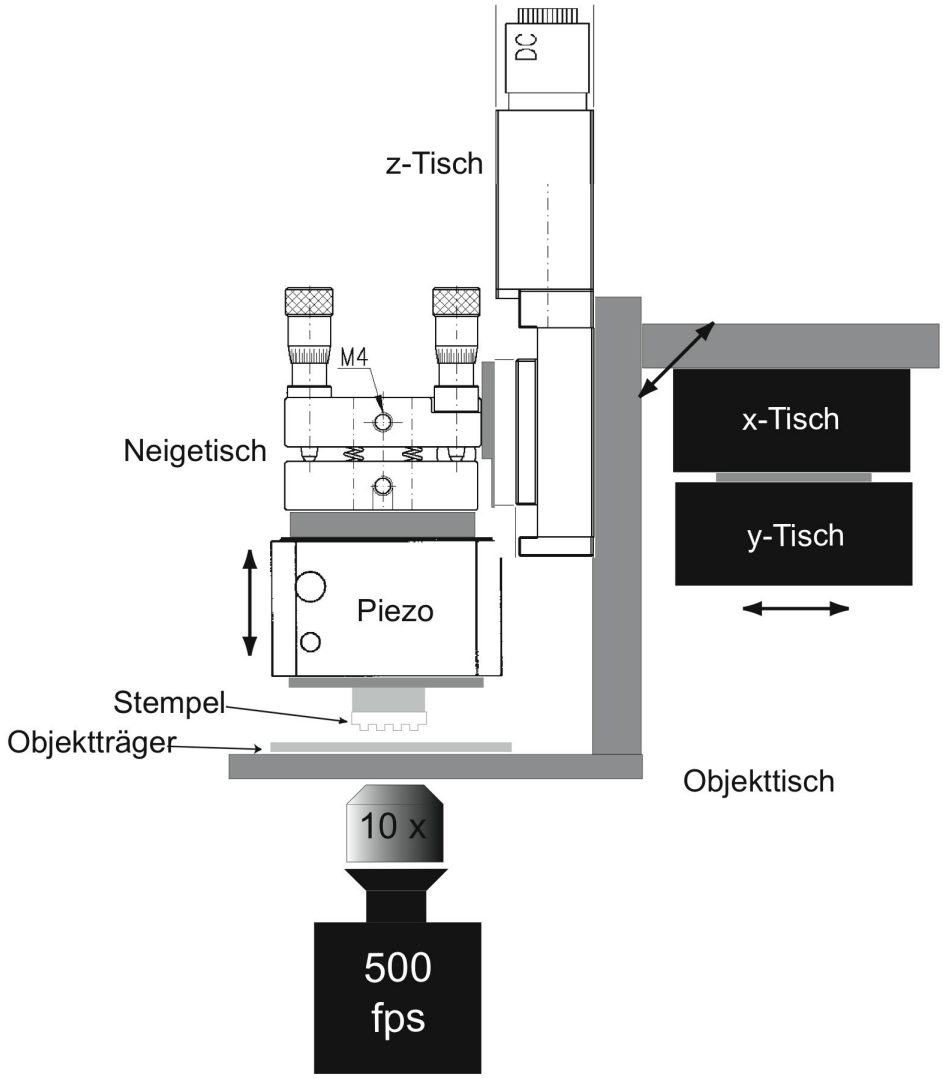

Abbildung 25: Das Kontaktgerät montiert auf einem inversen Mikroskop. Der Stempel wird durch den Piezoaktuator auf den Objektträger mit den Kraftwaagen aufgedrückt und wieder getrennt. Ein Neigetisch dient zur planparallelen Ausrichtung von Stempel und Objektträger. Vertikale Distanzen von mehr als 300 µm werden mit dem z-Tisch verfahren. Der x-y-Tisch dient dazu, einzelne Noppen in das Gesichtsfeld des Objektivs zu fahren.

Das vertikale Fahren des Stempels bis zum Kontakt bzw. das Trennen erfolgt bei diesem Gerät durch einen Piezoaktuator auf dessen Gehäuse der Stempel kopfunter angebracht wird. Die planparallele Ausrichtung des Stempels zum Objektträger wird mit einem Neigetisch eingestellt, mit dem sich das Piezogehäuse in zwei Richtungen verkippen lässt. Größere vertikale Distanzen, werden mit einem DC-Motortisch verfahren, der über den Neigetisch mit dem Piezo verbunden ist. Um einzelne Noppen in guter Auflösung beobachten zu können, kann der gesamte Apparat außerdem mithilfe eines x-y-Tisches über dem Objektiv verfahren werden.

Die Annäherung des Stempels an den Objektträger kann mit dem Mikroskop genau beobachtet werden, wobei bei sehr kurzen Distanzen von den Interferenzerscheinungen Gebrauch gemacht wird, die allgemein als Newton'sche Ringe bekannt sind. Diese treten auf, wenn zwei semitransparente Körper, die durch ein Medium niedrigerer optischer Dichte getrennt sind, einander bis auf wenige Mikrometer angenähert werden. Bei der Reflektions-Interferenz-Kontrast-Mikroskopie (RICM) kann diese Erscheinung dazu genutzt werden, um den Abstand einer Probe über dem Objektträger zu bestimmen, womit es beispielsweise möglich ist, das Adhäsionsverhalten von Vesikeln oder Zellen an Oberflächen zu studieren [6], [7].

Das Prinzip der RICM ist in Abb. 26 am Beispiel des hier untersuchten Systems Glas/Wasser/Silikon dargestellt: Von einem einfallenden Lichtstrahl der Intensität I_0 wird an der Glas-Wassergrenzfläche ein Strahl der Intensität I_1 und an der Wasser/Silikon-Grenzfläche eine Strahl der Intensität I_2 reflektiert. Aufgrund der verschiedenen Brechungsindizes von Wasser und Glas entsteht ein Gangunterschied zwischen I_1 und I_2 . Beim Zusammentreffen von Strahlen, die an verschiedenen Oberflächen reflektiert wurden, kommt es deshalb zu einer konstruktiven oder destruktiven Interferenz, je nach Abstand der beiden Oberflächen. Bei exakt parallel ausgerichteten Oberflächen erscheint deshalb das ganze Bild entweder als hell oder dunkel. Bei einem keilförmigen Spalt erhält man dagegen ein Bild mit alternierenden Helligkeitsmaxima oder -minima. Da der Kontrast im wässrigen Medium aufgrund des geringen Brechungsindexunterschieds von Wasser und Glas ($\Delta n_{Glas\text{-}Wasser} = 0{,}18$) bzw. von Wasser und der Probe sehr schwach ausfällt, verwendet man bevorzugt Objektive einer hohen numerischen Apertur, um eine möglichst große Ausbeute an reflektiertem Licht zu erhalten. Dies ist im vorliegenden Fall jedoch nicht möglich, da der Arbeitsabstand solcher Objektive viel kleiner ist als die Stärke der hier verwendeten Objektträger. Da es außerdem notwendig ist, ganze Noppen (1,1 mm Durchmesser) abzubilden, kommt maximal eine Vergrößerung von 10 x in Betracht. Als Kompromiss wird deshalb ein 10x-Fluar-Objektiv mit einer numerischen Apertur von 0,5 verwendet. Da dieses Objektiv jedoch ohne Immersionsöl betrieben wird, lassen Reflektionen an der Luft-Glas-Grenzfläche (zwischen Objektiv und Objektträger) das Hintergrundlicht erheblich ansteigen. Bei der Verwendung einer sensitiven Kamera (pco1200) und eines relativ breitbandigen Filters (HC Bandpass 628/40 nm) ist es dennoch möglich, einen ausreichend guten Kontrast zu erzielen.

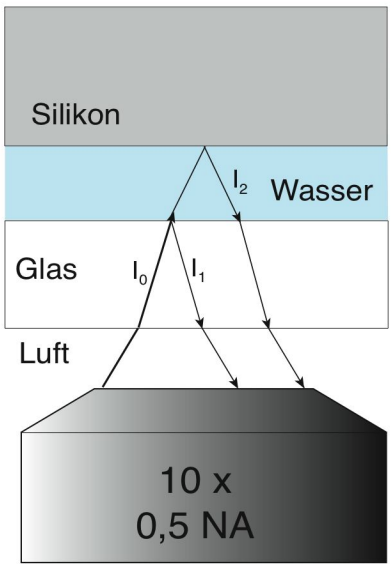

Abbildung 26: Das RICM-Prinzip: Ein Strahl der Intensität I_0 wird zu einem Teil an der Glas-Wassergrenzschicht und zu einem zweiten Teil an der Wasser-Silikongrenzschicht reflektiert. Die reflektierten Strahlen I_1 und I_2 weisen einen Gangunterschied auf, da I_2 eine Strecke in einem Medium mit einem geringeren Brechungsindex zurückgelegt hat, was bei einem Aufeinandertreffen solcher Strahlen zu Interferenzen führt.

Das RICM-Bild wird dazu verwendet, um Stempel und Objektträger exakt planparallel auszurichten und vor allem, um den exakten Kontaktpunkt zu finden, das heißt die Position in vertikaler Richtung, bei der alle Noppen in Kontakt sind, ohne dass es dabei zu einer Deformation der Mikrostruktur kommt, wie in Abb. 27 dargestellt.

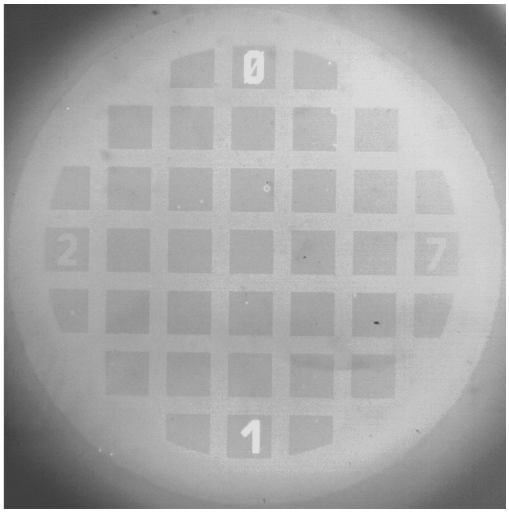

Abbildung 27: RICM-Aufnahme einer Noppe des Silikonstempels in Kontakt mit dem Objektträger. Am Kontrast ist deutlich zu erkennen, dass nur die erhabene, quadratische Silikonstruktur sich im Kontakt mit dem Objektträger befindet. Zwei der Ziffern leuchten hell auf, da sie mit Luft gefüllt sind.

Bei einem dynamischen Experiment, das heißt für den Fall, dass die Trenngeschwindigkeit genau bestimmt werden soll, wird von dem Trennvorgang ein

Film mit 500 Bildern/s aufgenommen und das Interferenzmuster analysiert, wie in P4 detailliert beschrieben.

12.4 Die Fluoreszenzmessung

Nach dem Trennen der beiden Oberflächen wird der Objektträger mit 0,2 x SSC-Puffer (kein H_2O!) gewaschen und sehr sorgfältig und langsam mit einem schwachen Stickstoffstrahl trocken geblasen. Daraufhin wird das Fluoreszenzsignal der Cy3™-Markierungen mit einem Laser-Scanner bei Anregungswellenlänge 532 nm bei 4 oder 6 µm Auflösung gemessen.

Um die Korrektur hinsichtlich der Kopplungseffizienz vornehmen zu können, wie in P2, P3 und P4 beschrieben, wird der Objektträger nach der ersten Fluoreszenz-Messung unter Schütteln für 30 min in einer Lösung von 1 µg /ml Streptavidn-Alexa-Fluor-647 in 1 x PBS und 0,4 % BSA inkubiert. Anschließend wird erneut in 0,2 x SSC gewaschen und trocken geblasen, wie oben beschrieben. Der Objektträger wird nun ein zweites Mal bei einer Anregungswellenlänge von 633 nm bei 4 oder 6 µm Auflösung gemessen.

Die Auswertung des Experiments erfolgt, wie in P2, P3 und P4 beschrieben.

12.5 Die Struktur der molekularen Kraftwaagen

Die Oligonukleotide der Kraftwaagen wurden mit Standard-Phosphor-Amidit-Chemie durch die Firma IBA GmbH in Göttingen hergestellt. Biotin- und Aminogruppen wurden als Phosphoramidite eingebaut. Die Cy3™-Fluoreszenzmarkierung wurde entweder als NHS-Ester oder als Phosphoramidit eingeführt. Die Oligonukleotide wurden in Stammlösungen von 100 µm in Aliquots zu 10 µl bei -20 °C aufbewahrt.

Bei der Auswahl der Sequenzen der Kraftwaagen wurde darauf geachtet, dass die Stränge keine selbstkomplementären Bereiche größer fünf Basenpaare aufweisen, um unerwünschte Sekundärstrukturen auszuschließen. Als Abstandshalter zwischen den beiden Duplexen sowie zwischen den Oberflächen und den Duplexen wurden stets 10-20 Thymidin-Nukleotide eingebaut.

12.6 Verbrauchsmaterial

Aldehydobjektträger	nexterion Slide AL, Peqlab, Erlangen
Aminosilan	3-Aminopropyldimethyl-ethoxysilan, ABCR, Karlsruhe
Bio-PEG-NHS	Biotin-Polyethylenglycol-N-Hydroxy-Succinimid, MW 3.400, Nektar, Huntsville
Biotin-PEG-NH2	MW 3000, Rapp Polymere, Tübingen
BSA	Albumin Fraktion V, Protease-frei, Roth GmbH, Karlsruhe
Epoxysilan	3-Glycidoxy-propyl-trimethoxy-silan, ABCR, Karlsruhe
Ethanol	reinst, Roth GmbH, Karlsruhe
Fluorsilan	1H,1H,2H,2H-Perfluorodecyltrichlorosilan, ABCR; Karlsruhe
H_2O	bidestilliert
Hexan	wasserfrei über Molekularsieb, Sigma, Taufkirchen
Hybridisierungsmaske	Sonderanfertigung, Grace Biolabs, Bend, OR, USA
Isopropanol	Roth GmbH, Karlsruhe
Methoxy-PEG-NH2	MW 2000, Rapp Polymere, Tübingen
NaOH	Natriumhydroxid-Plätzchen, Merck, Darmstadt
Natriumborhydrid	Sigma, Taufkirchen
Oligonukleotide	IBA GmbH, Göttingen
PBS	Phosphate buffered Saline 10 x, Roche, Penzberg
PDMS	Polydimethysiloxan, Sylgard 184, Dow Corning
Silikondichtlippe	Adhesive Silicone Isolator, Grace Biolabs, Bend, OR, USA
SSC	20 x SSC, Sodium-Sodium-Citrat (pH7,2), Sigma, Taufkirchen
Streptavidin	Invirtogen, Karlsruhe
Toluol	Roth GmbH, Karlsruhe

12.7 Geräte

1,25 x	Epiplan Neofluar
10 x Objektiv	10 x Fluar, 0,5 NA, Zeiss
DC-Tisch-Steuerung	DC500, OWIS GmbH, Staufen
Laser-Scanner	Tecan-LS Reloaded, Tecan Trading AG, Schweiz
Mikroskop	Zeiss Axiomat
Piezoaktuator	pz400, Piezosysteme Jena, Jena
y-z-DC-Motor-Tisch	Linearmesstisch LM60, OWIS GmbH, Staufen
z-DC-Motor-Tisch	Linearmesstisch LM45, OWIS GmbH, Staufen

12.8 Literatur (Material und Methoden)

1. Wilbur, J.L., et al., *Microfabrication by microcontact printing of self-assembled monolayers.* Advanced Materials, 1994. **6**(7/8): p. 600-4.

2. Southern, E., K. Mir, and M. Shchepinov, *Molecular interactions on microarrays.* Nat Genet, 1999. **21**(1 Suppl): p. 5-9.

3. Morra, M.J., D, *On the aging of Oxygen Plasma-Treated Polydimethylsiloxane Surfaces.* Journal of colloid and Interface Science, 1990. **137**(1): p. 11-24.

4. Faltlhauser, M., *Zugratenabhängige Messungen an Nukleinsäureduplexen mit dem differenziellen Krafttest*, in *Fachbereich 06, Bioingenieurswesen*. 2006, University of applied sciences: Munich. p. 78.

5. Piehler, J., et al., *A high-density poly(ethylene glycol) polymer brush for immobilization on glass-type surfaces.* Biosens Bioelectron, 2000. **15**(9-10): p. 473-81.

6. Rädler, J. and E. Sackmann, *Imaging optical thickness and separation distances of phospholipid vesicles at solid surfaces.* Journal de Physique II, 1993. **3**: p. 727-748.

7. Weber, I., *Reflection Interference Contrast Microscopy.* Methods in Enzymology, 2003. **361**: p. 34-47.

13. Anhang (Abkürzungen)

AFM	Atomic Force Microscope
bp	Basenpaar(e)
DMSO	Dimethylsulfoxid
DR	Daunorubicin
FRET	Förster-Resonanz-Energie-Transfer
MM	Mismatch
NMR	Nuclear Magnetic Resonance
PDMS	Polydimethylsiloxan
PM	Perfect Match
RICM	Reflection Interference Contrast Microscopy

Danke

An dieser Stelle vielen Dank an alle, die mich bei dieser Arbeit unterstützt haben:

- Hermann Gaub für die Betreuung der Arbeit, bei der er insbesondere Außergewöhnliches als Übersetzer Physik => Bio, Bio => Physik zu leisten hatte.

- Hauke Clausen-Schaumann, Gregor Neuert und Robert Lugmaier, für die gute Zusammenarbeit.

- Dieter Braun für die Unterstützung beim Aufbau der Hardware und viele hilfreiche Diskussionen.

- Angelika Kardinal für ein gut funktionierendes und gut gestimmtes Labor.

- Martin Benoit für viele Hilfestellungen und die moralische Unterstützung.

- Dominik Ho, meinem Nachfolger dafür, dass ich das Projekt Kraftwaage in guten Händen weis.

- Philip Severin, Christoph Wienken und Marcus Otten für Ihr großes Engagement als Praktikanten und Werkstudenten.

- Merit Faltlhauser, von der FH-München, für Ihre Bereitschaft ihr Diplomarbeit an der Universität durchzuführen.

- Philip Baaske für viele Tips zum Thema DNA.

- Stefan Kufer und Lars Sonnenberg, für die entspannte Stimmung im Büro.

- Wolfgang Parak für die Bereitstellung des Mikroskops.

- Und allen, die zu einer guten Atmosphäre am Lehrstuhl beigetragen haben.

Erklärung

Hiermit versichere ich, die vorliegende Arbeit selbstständig ausgeführt und keine weiteren Hilfsmittel als die im Text und im Literaturverzeichnis aufgeführten verwendet zu haben.

München, den

_____

Christian Albrecht